# IN-SITU CAMERAS FOR RADIOMETRIC CORRECTION OF REMOTELY SENSED DATA

by

Jess S Kautz

A Dissertation Submitted to the Faculty of the

COLLEGE OF OPTICAL SCIENCES

In Partial Fulfillment of the Requirements

For the Degree of

DOCTOR OF PHILOSOPHY

In the Graduate College

THE UNIVERSITY OF ARIZONA

2017

THE UNIVERSITY OF ARIZONA

GRADUATE COLLEGE

As members of the Dissertation Committee, we certify that we have read the dissertation prepared by Jess S Kautz entitled In-Situ Cameras for Radiometric Correction of Remotely Sensed Data and recommend that it be accepted as fulfilling the dissertation requirement for the Degree of Doctor of Philosophy.

____________________________________________ Date: July 21 2016

Stephen R. Yool

____________________________________________ Date: July 21 2016

J. Scott Tyo

____________________________________________ Date: July 21 2016

Jeffery Czapla-Myers

Final approval and acceptance of this dissertation is contingent upon the candidate's submission of the final copies of the dissertation to the Graduate College.

I hereby certify that I have read this dissertation prepared under my direction and recommend that it be accepted as fulfilling the dissertation requirement.

____________________________________________ Date: July 21 2016

Dissertation Director: Stephen R. Yool

# STATEMENT BY AUTHOR

SIGNED: Jess S Kautz

# ACKNOWLEDGEMENTS

I would like to thank Jeff Czapla-Myers, Nik Anderson, Stuart Biggar, and Oscar Hernandez of the Remote Sensing Group at the University of Arizona, for all their help with both their technical expertise and lending me necessary equipment for this work.

I also extend my thanks to Dave Kopec and the people of the Karsten Turfgrass center provided and maintained the site for this research. Without them, the process of gathering this data would have been much more difficult.

I thank Steve Yool, Jeff Czapla-Myers, Scott Tyo and for being my committee members for all the hours he has put in talking me through aspects of project. Their suggestions have been invaluable for improving this dissertation.

Thank you to Kyle Hartfield and Patrick Broxton for their assistance with solving programming issues in the later simulations in this dissertation.

My sincerest thanks to my mother, brother and wife for all their proof reading help for a long document which is not at all in any of their fields.

Finally, I owe thanks to my family for all their support and understanding during the long hours put into this project.

# DEDICATION

Dedicated to the atmosphere,
which has almost always been there
when I needed it.

# Table of Contents

# List of Figures

# List of Tables

# List of Acronyms

| | |
|---|---|
| 6S | Second Simulation of a Satellite Signal in the Solar Spectrum, |
| ACORN | Atmosperic CORrection Now |
| AMBRALS | Algorithm for Modeling Bidirectional Reflectance Anisotropies of the Land Surface |
| AMOS | Archive of Many Outdoor Scenes |
| ASD | Analytical Spectral Device |
| ASTER | Advanced Spaceborne Thermal Emission and Reflection radiometer |
| ATCOR | ATmosperic CORrection (an algorithm) |
| BRDF | Bidirectional Reflectance Distribution Function |
| BRF | Bidirectional Reflectance Factor |
| CCD | Charge Coupled Device |
| CMOS | Complementary Metal–Oxide–Semiconductor |
| COST | Not an acronym. Name of Chavez's (citation) atmospheric correction method |
| DMC | Dry Matter Content |
| DN | Digital Number |
| DOS | Dark Object Subtraction |
| EGO | European GOniometric facility |
| ELM | Empirical Line Method |
| ETM+ | Enhanced Thematic Mapper Plus |
| EWT | Equivalent Water Thickness |
| FIGOS | FIeld GOniometer System |
| FLAASH | Fast Line-of-sight Atmospheric Analysis of Hypercubes |
| HATCH | High-accuracy Atmospheric Correction for Hyperspectral data |
| HCRF | Hemispherical Conical Reflectance Factor |
| HyMap | Hyperspectral Mapper |
| IKONOS | Not an acronym |
| LAI | Leaf Area Index |
| LIDAR | Light Detection And Ranging |
| LISS-IV | Linear Imaging Self-scanning System |
| LOWTRAN | LOW resolution atmospheric TRANsmission |
| LTER | Long Term Environmental Research |
| LUT | Look-Up Table |
| MISR | Multiangle Imaging SpectroRadiometer |
| MODIS | Moderate Resolution Imaging Spectroradiometer |
| MODTRAN | MODerate resolution atmospheric TRANsmission |
| MTF | Modulation Transfer Function |
| NDVI | Normalized Difference Vegetation Index |
| NIR | Near Infra-Red |
| NIST | National Institute of Science and Technology |
| NuRADS | New Upwelling Radiance Distribution |
| OLI | Operational Land Imager |

| | |
|---|---|
| pBRDF | polarization Bidirectional Reflectance Distribution Function |
| PIF | Pseudo-Invariant Feature |
| POLDER | POLarization and Directionality of the Earth's Reflectances |
| PROSAIL | A portmanteau of PROSPECT and SAIL |
| PROSPECT | Not an acronym |
| RAMI | Radiation transfer Model Intercomparison |
| RMS | Root Mean Square |
| RSG | Remote Sensing Group (of the University of Arizona) |
| SAIL | Scattering by Arbitrarily Inclined Leaves |
| SAVI | Soil Adjusted Vegetation Index |
| SFG | Sandmeier Field Goniometer |
| SMARTS | Simple Model of the Atmospheric Radiative Transfer of Sunshine |
| SPOT | Satellite Pour l'Observation de la Terre |
| TOA | Top of Atmosphere |
| TSP01 | A Thorlabs item number |
| USB | Universal Serial Bus |
| WiSARD | Wireless Sensing And Relay Device |

# Abstract

The atmosphere distorts the spectrum of remotely sensed data, negatively affecting all forms of investigating Earth's surface. To gather reliable data, it is vital that atmospheric corrections are accurate. The current state of the field of atmospheric correction does not account well for the benefits and costs of different correction algorithms. Ground spectral data are required to evaluate these algorithms better. This dissertation explores using cameras as radiometers as a means of gathering ground spectral data.

I introduce techniques to implement a camera systems for atmospheric correction using off the shelf parts. To aid the design of future camera systems for radiometric correction, methods for estimating the system error prior to construction, calibration and testing of the resulting camera system are explored. Simulations are used to investigate the relationship between the reflectance accuracy of the camera system and the quality of atmospheric correction. In the design phase, read noise and filter choice are found to be the strongest sources of system error. I explain the calibration methods for the camera system, showing the problems of pixel to angle calibration, and adapting the web camera for scientific work. The camera system is tested in the field to estimate its ability to recover directional reflectance from BRF data. I estimate the error in the system due to the experimental set up, then explore how the system error changes with different cameras, environmental set-ups and inversions. With these experiments, I learn about the importance of the dynamic range of the camera, and the input ranges used for the PROSAIL inversion. Evidence that the camera can perform within the specification set for ELM correction in this dissertation is evaluated. The analysis is concluded by simulating an ELM correction of a scene using various numbers of calibration targets, and levels of system error, to find the number of cameras needed for a full-scale implementation.

# 1 Introduction

## 1.1 Motivation

In the field of remote sensing, research focuses frequently on the measurement of electromagnetic radiation reflected or emitted from the Earth's surface (Jensen, 2007). The atmosphere degrades the quality of this remotely sensed data by adding random noise, scattering light we desire to measure out of the field of view of a sensor, and scattering undesired light in from adjacent areas and the sky. While there are many methods of correcting for atmospheric effects, their results are inconsistent with one another. Not only does the magnitude of correction vary between methods (Figure 1) but in some cases even the direction of correction is different, moving the estimated reflectance even further from the ground reference data (Moran et al. 1992). In-situ measurements of near-nadir reflectance provide a way of comparing the relative quality of atmospheric correction, and a means of improving corrections. Taking these measurements presently can be a large and expensive undertaking (Sellers et al., 1988 ; Moran et al., 1992).

I developed software and tested off-the-shelf and custom-built cameras as a cost-effective means of gathering ground spectral data and estimating near-nadir reflectance. Unlike a spectroradiometer, cameras provide a means of sampling the reflected radiance over a large area quickly, while being able to account for variations in reflectance across a scene. By measuring the bidirectional reflectance factor (BRF) and near-nadir reflectance, cameras can use grass areas as calibration targets to provide a reflectance estimate to be used in an empirical atmospheric correction, such as the empirical line method (ELM). This ELM correction could then be used to evaluate other corrections, providing data for choosing an appropriate atmospheric correction when in-situ data are more limited.

## 1.2 Background

Remote sensing users are often interested in collecting and interpreting measurements of electromagnetic radiation (Jensen, 2007). The sun provides known illumination throughout the electromagnetic spectrum that reflects off objects on Earth's surface. Sensors on satellite or airborne platforms can then passively detect this reflected radiation. Finding the ratio between downwelling light and the light reflected provides the reflectance of the surface. Measuring the reflectance of surfaces, and finding correlations enables researchers to quantify and classify objects on Earth’s surface (Vincent, 1972 ; Ahern et al., 1977). However, light reaching these

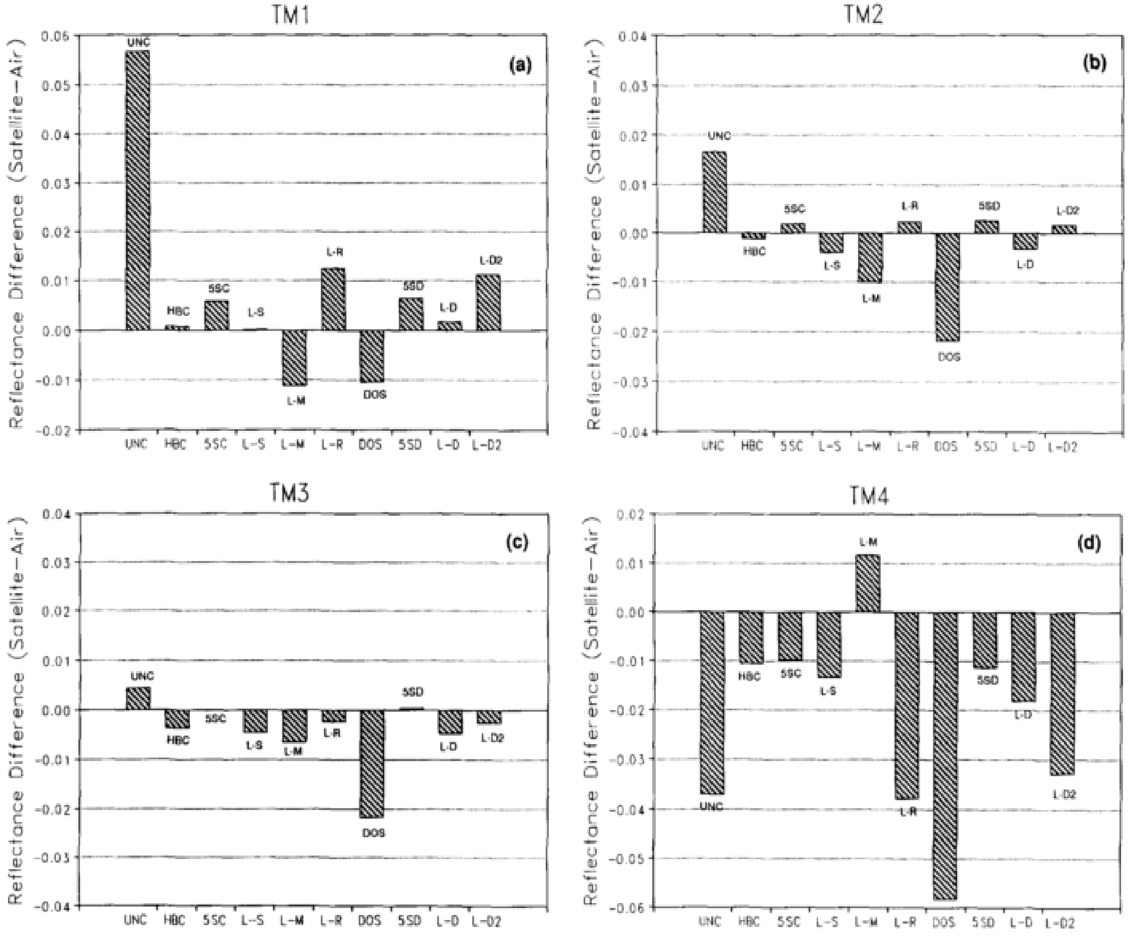

*Figure 1: Plot from a paper by Moran et al. (1992), showing the difference between estimated reflectance taken from Landsat images after correction, and an airborne sensor. The data taken by the airborne sensor are treated as ground reference data for the reflectance in this example. From left to right, the corrections used are: no correction, Herman-Browning code, 5S code with on-site optical depth measurement, three Lowtran7 models with different estimated inputs, Dark Object Subtraction, and three more models (5S and Two Lowtran7) based on estimating dark object reflectance.*

sensors interacts with both surface objects and the atmosphere. (Otterman & Robinove, 1981). The atmosphere reduces the transmission of the reflected light and scatters radiance from other sources into the sensor (Ahern et al., 1977). This effect can be written:

$$L_{Sensor} = L_R T + P \qquad \text{Eq (1)}$$

$L_{sensor}$ is the radiance observed by the sensor, $L_R$ is the reflected radiance in the direction of the sensor by an area of interest, T is the transmission of the atmosphere, and P is the path radiance scattered into the sensor by the atmosphere. As the atmosphere scatters more light, P will go up and T will go down, reducing the variation in $L_{sensor}$ across a scene due to $L_R$. This reduces contrast, making $L_R$ less distinct against other factors, such as digitalization or random system noise. The atmosphere and its effect vary with time and location (Goetz, 2009). Reduced transmission decreases classification accuracy by narrowing the range of digital number (DN) values recorded by the sensor over a scene while increased path radiance widens the range of values associated with any class. Different classes will have increasingly similar ranges of DN values, making it harder to differentiate them (Figure 2). This applies particularly to cases on the edges of the probability densities of two otherwise spectrally distinctive classes of objects. The way the atmosphere changes the spectrum of remotely sensed data can compromise efforts to compare classifications from different dates or places. Without the intervening atmosphere, if measurable factors such as sensor response and sun angle were accounted for, it would be possible to map a particular set of DN values from a sensor to a previously established classification. With an intervening atmosphere, each classification set up must be done independently, since the data from each image will be distorted in different ways. This will make the data space for each image different, and makes it less likely that algorithmically selected classes will be consistent from image to image. In this way, the atmosphere negatively affects land-use classification (Miller, 2002), comparison of data from different times and places (Congalton, 2010), and the measurement of quantitative properties (Liang et al., 2001).

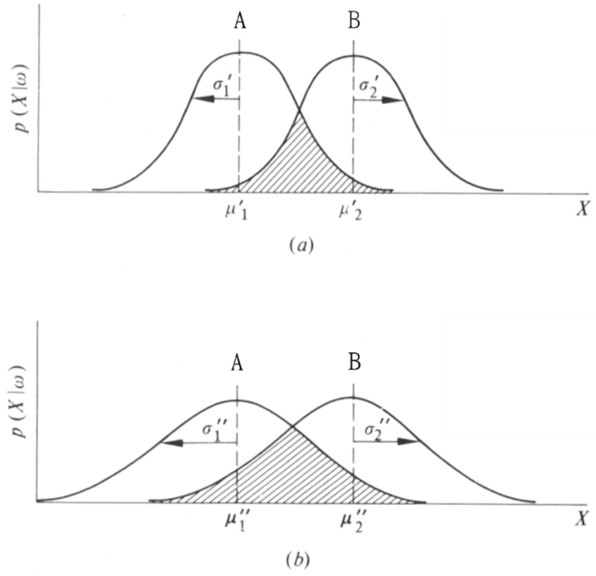

*Figure 2: For two land classification classes A and B, given readings X, we have a probability function of P(X|w) of being in A or B respectively. The hatched area represents areas where the probabilities cross over. As the range of spectral readings X where the probability of being in a class expands, as due to atmospheric effects, the area where the probability of being in either class will increase. Figure modified from one found in* (Davis et al., 1978).

Researchers have developed a large number of methods of estimating atmospheric effects. To avoid the complication and expense of measuring the atmosphere's composition at the time of fly over, corrections are often dependent on mathematical approximations and value estimations. When deciding on a method of atmospheric correction to use, the relative quality of correction should be an important consideration. This is something not well addressed by the present literature.

## 1.3 Scope of Work

### 1.3.1 Intention of Research

Without certainty in the quality of atmospheric correction, empirical ground reflectance data provide a means of evaluating corrections, increasing or verifying accuracy (Gao et al., 2009). More large-scale general studies of atmospheric correction would be desirable but tend to be costly, as they require knowledge of the ground, either gathered by aircraft-borne sensors, or a number of researchers on the ground (Sellers et al., 1988). Ground-based camera systems would reduce the cost of these general studies.

Automated systems enable continuously gathering spectral data, unlike current implementations of the Empirical Line Method (ELM), which use technicians in the field to take readings (Smith & Milton, 1999 ; Karpouzli & Malthus, 2003 ; Baugh & Groeneveld, 2008). A camera system splits the target into discrete elements taken over a range of angles. These data can approximate BRF (Nandy, 2000 ; Dymond & Trotter, 1997 ; Shell, 2005) and account for spatial variations such as shadows and instrumentation found within the field of view (Demircan et al., 2000). This is an improvement on current automated spectral monitoring systems, which record the entire target using a single spectroradiometer reading, reducing the area to a single pixel of data (Leuning et al., 2006 ; Schiller & Luvall, 1994 ; Czapla-Myers, 2006). Some researchers have tried to account for spatial variation by moving spectrometers across the area of interest (Gamon et al., 2006 ; Berry et al., 1978 ; Bell et al., 2002). A camera system removes the need for the tramway used by Gamon et al. and Berry et al., or the tractor and driver used by Bell et al., reducing the infrastructure required for monitoring spectral reflectance over a large area.

By sampling over a wide range of angles, a camera has a significant advantage over a conventional spectroradiometer: To take near-nadir readings of radiance with a radiometer, the radiometer must necessarily be pointed near-nadir. To view a large area, the radiometer must by necessity be either moved or aimed around the target, be very high off the ground, or have a very wide field view and thus mostly taking data from off-nadir angles. A camera can view its target at off-nadir angles, while gathering data to account for BRF effects, enabling it to see a larger area from a lower height, without automation, lowering the cost of implementation. Setting the camera at a non-nadir position places the platform the camera or sensor is attached to outside of its field of view, and can help avoid self-shadowing. In order for the camera to take some near-nadir readings, near-nadir must only be at some point within its field of view. For a wide field of view camera, it would be possible for it to simultaneously take readings both near-nadir and in the direction of the hot spot or specular reflection, better accounting for possible BRF effects when a satellite-borne sensor is off-nadir. Seeing a larger section of the target enables a better accounting for the variation across the calibration target, improving the error budget. This is particularly important for a surface like vegetation, which can vary significantly over space and time (K. Anderson et al., 2011).

This research demonstrates the validity of using a camera system to estimate reflectance in the field. I seek to establish the relation between system choices and system accuracy. Any individual implementation of a camera system would provide limited knowledge of the strengths and weaknesses of using camera-based systems for atmospheric correction. Exploring a number of implementations enabled mapping the benefits of different BRF models, targets, and spectral resolutions. This information shows the potential of both high end and economical solutions, and which sub-systems are the most critical to implementation.

To focus this research, the scope of this dissertation was limited to two camera systems, three BRF models per surface and two types of targets, listed below (Table 1).

*Table 1: Systems and Targets to be tested*

| Cameras | BRF Models | Targets |
|---|---|---|
| -Multispectral<br>-Web Camera | -Kernel Driven (AMBRALS)<br>-Vegetation Property Driven (PROSAIL)<br>-Non-Analytic Solution (Curve Fitting) | -Healthy Turf Grass<br>-Distressed Turf Grass |

### 1.3.2 Choice of Cameras

Testing was limited to light in the visible and the near infrared. This enabled the study to be done with one set of cameras, as it is rare for a single sensor to be sensitive in both the visible and longer infrared regions (Goetz, 2009). The research was limited further to the multispectral bands used by the Landsat 7 Enhanced Thematic Mapper Plus (ETM+) sensor: the blue (450-520 nm), green (520-600 nm), red (630-690 nm) and near-infrared (NIR) (760-900 nm). While there is no standard spectral resolution for remote sensing systems, many satellite-borne sensors have bands similar to Landsat 7 ETM+, including Quickbird, IKONOS, ASTER, LISS-IV, SPOT and GOKTURK-2 (“ITC’s database of Satellites and Sensors,” n.d.).

Reflection recovery was tested using two different cameras: 1) A multispectral camera with bands comparable to the Landsat 7 ETM+ bands provided reflectance data that corresponded directly with the reflectance needed for atmospheric correction. This represented the most straightforward solution to correction. The multispectral camera was built using off the shelf parts to keep costs down, and to demonstrate the feasibility of future low-cost implementations. 2) An off the shelf USB camera was tested as a cheaper, and readily available alternative. Outdoor security cameras already exist, and come with a very wide full field of view, often over 70°, and are sensitive in both the visible and the NIR. Modifications to the camera could be limited to spectral filtering to separate the NIR from the red. Such cameras are significant to this research because they represent an opportunity to gather useful data at a very low cost. Inexpensive cameras are key to being able to use more cameras and calibration sites, or multiple cameras at the same site. They also present an opportunity to get citizens invested in remote sensing at a low cost, in the form of citizen science.

### 1.3.3 Choice of Calibration Test Targets

My dissertation focused on a small-scale system, testing the feasibility of this line of research while keeping costs down. This was done by placing the cameras much closer to the ground, and using an ASD (Analytical Spectral Device) to act as a simulated satellite. Doing this enabled many more data points to be gathered than if a real satellite system had been used. It avoided many sources of increased costs: building and setting up multiple full-scale cameras, increased automation, finding and getting permission to set up at multiple sites, and finding ways to secure the camera system sufficiently high off the ground.

Using a smaller target made it easier to keep the area clear of animals, trash and people at the time of testing. It simplified aiming the radiometer, both in estimating geometrically where it was pointed and in testing the aim. The area was sufficiently small that it was possible to use a piece of near-Lambertian Teflon to cross-calibrate both the camera and the radiometer in each setup, improving accuracy and speeding up data acquisition. While changing radiance into reflectance using a known Lambertian surface would not be feasible for a full-scale system, conversion of digital numbers to reflectance is a problem with known solutions (Moran et al., 1997), and thus was not of interest to this dissertation.

I focused on grass targets, as it is a common surface in any city, and very frequently free of people and structures. Both healthy and distressed grass were used, as they present different spectral profiles (Sonmez et al., 2008). Other urban targets, such as asphalt and roofing materials were deemed undesirable. To work as a calibration target for satellite-borne sensors, the chosen area must be large and uniform, which is rare for urban surfaces. The exceptions to this are roads, parking lots, and airport runways, but these are frequently both painted and covered in vehicles, which would confound the BRF recovery process. Future tests of camera-based systems for reflectance recovery might try additional agricultural or natural surfaces. Wilder grasses, shrubby bushlands, and crops with some volume structure to them would be of the considerable interest since these should present different BRF structures than those examined in this dissertation.

### 1.3.4 Choice of Bidirectional Reflectance Factor Models

By its nature, a sensor used to recover near-nadir reflectance from off-nadir data requires some understanding of BRF. For a camera system, each pixel will view the target surface at a different angle, which provides ample information that can be fed into a BRF model. The model is then needed both to estimate reflectance angles outside the field of view of the camera, and to help differentiate between changes of reflectance due to view angle and changes due to a change in the nature of the calibration target. Two analytic models were chosen to compare their ability at recovering the desired near-nadir reflectance: AMBRALS (the Algorithm for Modeling Bidirectional Reflectance Anisotropies of the Land Surface); and PROSAIL, which is a combination of the Prospect leaf reflectance model, and SAIL (Scattering by Arbitrarily Inclined Leaves) BRF model. Both are well known in the field of remote sensing (Ni & Li, 2000 ; Hu et al., 1997 ; Wang et al., 2013 ; Si et al., 2012 ; Hilker et al., 2011 ; Darvishzadeh et al., 2008), but recover BRF in different ways. The AMBRALS model uses kernel functions (Figure 3) representing different types of vegetation cover, and its inversion is analytic finding relative weights for these covers and kernels (Strahler & Muller, 1996). The PROSAIL model (which is a combination of the PROSPECT and SAIL models) is more complex, using eleven input parameters such as the leaf area index (LAI) and chlorophyll content to simulate multiple interactions with leaves. Because of this, it is not

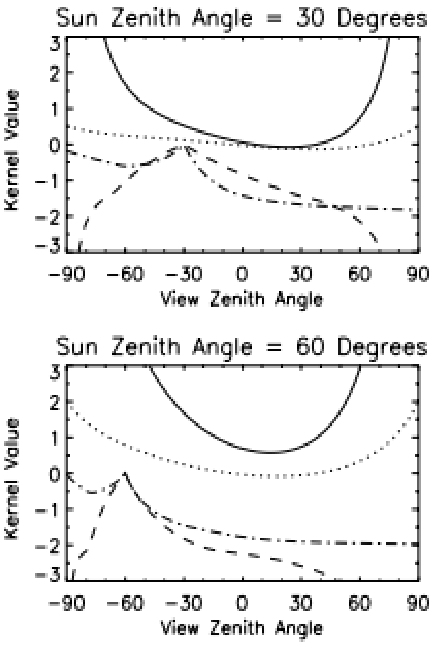

*Figure 3: Kernels used to model vegetation BRF, along the solar principle plane, for sun angles of 30° & 60°. The kernels are called, Thin (solid line), Thick (dotted), Dense (dash-dotted) and Sparse (dashed)*

possible to invert the PROSAIL model analytically, I instead implemented a look-up table (LUT) solution. To explore a non-analytic model for BRF, I tested curve fitting as a means of near-nadir reflectance recovery. Physical models (both AMBRALS and PROSAIL) can be impractical for situations where a researcher is interested only in making a correction for the change in BRF across a scene (Kennedy et al., 1997). There is no need to find the BRF in all possible directions, nor the underlying vegetation parameters. By avoiding estimates of vegetation quantity and quality, this solution should be more valid for surfaces with sparse or no vegetation. I found early on that curve fitting was not a good match for this problem. Working over such a large range of azimuth and zenith angles confounded curve fitting algorithms designed for Cartesian inputs.

### 1.3.5 Environmental Concerns

During the process of data gathering, it became apparent that this was a year with unusual weather with far fewer cloud-free summer days than are typical in southern Arizona. This was taken as an opportunity to observe how the system performed with various amounts of cloud cover. This would provide data more consistent with real world conditions in environments outside the desert. Data from days with clouds present were sorted broadly into Cloudless, Peripheral, and Overhead categories. Cloudless data consisted of data taken on days where there were no clouds, or when clouds remained beneath the tree line. Overhead measurements consisted of data where there was a perceived risk of the clouds covering the sun during the data taking process. Peripheral data comprised all those days that did not fall into either of the other two categories, where there were clouds present, but were assessed to have only the effect of increasing the hemispherical irradiance of the scene. Images of the sky were recorded throughout the day so that a more rigorous classification process could be applied later as necessary.

## 1.4 Dissertation Overview

Section 1 of this dissertation introduces the motivation for this dissertation and the intended scope of the work.

Section 2 describes previous work in the fields of atmospheric correction, measuring vegetation reflectance, BRF and parameters, and systems for measuring these values, and relates how these previous discoveries relate to and have influenced my own work.

In Section 3, the process of estimating various sources of system error is discussed. The camera design decisions motivated by these error specifications are described, as well as the processes for assembling the system. The final part of Section 3 describes the process of calibrating the system, with a focus on laying out the processes for future work by non-engineers.

Section 4 describes the field work done to test the camera system and the processing of the data produced. It performs several experiments to better understand the capabilities and limitations of a camera system and the individual components that seem to be most important. The limits of atmospheric correction possible by these cameras are explored through performing an atmospheric correction with the gathered data and simulating the results for a correction performed with a larger array of ground data.

Section 5 presents the conclusions to this paper and ideas for future work.

In Appendix A, I go into some additional detail on the modifications I found necessary to make on PROSAIL and its inversion, in order to speed the look-up table generation process.

# 2 Theoretical Background

## 2.1 Atmospheric Correction

### 2.1.1 Overview

Atmospheric correction is a rich field of research, filled with a large variety of methods of doing a single task: removing the atmosphere from remotely sensed images. This research is motivated by a desire to better understand and improve atmospheric correction, reducing ambiguity over which form of atmospheric correction is best. In most engineering problems, one can reasonably estimate the benefits against the costs of various approaches, but this is not the case for atmospheric correction.

Atmospheric correction is always important to finding the true value of ground reflectance, and there may be disparities in which correction is best in different instances. What works best over the desert, where top of atmosphere (TOA) reflectances can get to 90% (Dinter et al., 2009), might be different than when the starting reflectance is low, such as in ocean water color studies (Gao et al., 2009). This can be seen in the research of Wu, Wang, & Bauer, (2005), who found that the COST method of correction (Chavez, 1996), while providing good correction in arid environments, worked significantly less well in the NIR when they tested it in the

Midwest, which they attributed to increased moisture in the atmosphere. My research introduces a new tool for choosing between atmospheric corrections, by providing a means to perform long-term studies on methods of correction, and expanding research into environments with a wider range of climates. The next section of the dissertation explores the history of atmospheric correction, its varied methods, and why another tool for comparing them is necessary.

### 2.1.2 Categories of Atmospheric Correction

Atmospheric corrections can be broadly sorted into four categories: image-based, spectrally-based, atmospheric modeling and those based on empirical data. Image-based correction techniques use data from the images themselves. Early examples of atmospheric correction were image-based, using dark objects (Vincent, 1972) and pseudo-invariant features (Ahern et al., 1977) to estimate path radiance. Modern image-based techniques include dark object subtraction (DOS) (Rowan et al., 1974), the COST method developed by Chavez (1996), and refined by Wu, Wang, & Bauer (2005), and the pseudo-invariant feature method (PIF) (Schott et al., 1988). This form of atmospheric correction has an advantage when looking at historical data, where data for a more empirical form of correction may not exist.

Spectrally-based techniques also use data found only in the image, but focus more on the spectrum of the reflected light. In this category are techniques like the Regression Intersection Method (Crippen, 1987), which made use of the spectral principle components of homogeneous targets, or making the use of knowledge water absorption bands in hyperspectral data (Gao et al., 2009).

Atmospheric modeling forms of atmospheric correction work through knowledge of the scattering and absorption properties of the different molecules and particles within the atmosphere. This form of correction is based on extensive measurement of the atmosphere's composition and the effects this has on remotely sensed data. Models of layers of the atmosphere can be used to estimate the quantity of downwelling and upwelling light, as well as its spectral or hemispheric direction. This provides a popular method of correction for work that requires high precision, such as vicarious calibration (Helder, Thome, et al., 2012), however, it can be expensive to access these modeling programs. Examples of atmospheric modeling programs include 6S (Vermote & Tanré, 1997), MODTRAN (Berk et al., 2006), HATCH (Qu, Kindel, & Goetz, 2003), ACORN, ATCOR, FLAASH.

The last group of techniques for atmospheric correction is empirical models. This category of atmospheric correction is of interest to this dissertation, since they have been verified to be very accurate, and thus can be relied upon to verify the accuracy of other atmospheric corrections. Atmospheric modeling programs can be empirically sound if there is sufficient atmospheric data taken at the time of flyover, however, this may require sonde data taken from an airborne platform (Berk et al., 2006). Another source of empirical data is in-situ measurements of reflectance. These measurements can be used with the Empirical Line Method (ELM) or some atmospheric modeling programs. ELM, as described by Smith & Milton (1999), is of particular interest to this project, since it is direct, simple and has been thoroughly demonstrated.

### 2.1.3 Atmospheric Correction Using Models

For all models, the quality of the output depends on the input provided. In cases where not much is known about the atmosphere, variations in the input parameters provided can cause significant changes in the resulting data (Moran et al., 1992 ; Goetz et al., 1998).

In the Moran et al. study, they experimented with many forms of atmospheric correction and the different inputs that could be used for them. This included using atmospheric models using some ground data, atmospheric models done using seasonal assumptions, and more simple corrections, such as dark object subtraction. As can be seen in Figure 1, the results from changing models or even just inputs to a model can result in radical changes in the estimated reflectance of a surface. Goetz et al. (1998) demonstrated the effects of changes within a single modeling program, by exploring which of 13,200 MODTRAN possible models of the atmosphere, generated using different input parameters to MODTRAN, produced the best fit to ground data they had gathered. Mahiny & Turner (2007) showed the effect of four different atmospheric corrections on a binary woodlands / non-woodlands classification, including COST, PIF, and 6S. While all of the corrected images classified more woodlands than the uncorrected images, and found very similar quantities of woodlands, only around 27% of the new woodlands overlapped in all four images. Finally, in a study by Hadjimitsis & Clayton (2004) looking at the color of several reservoirs found that dark object subtraction, a very basic correction, outperformed both ATCOR and 6S when these used their standard atmospheric models. All these studies show that atmospheric correction based on assumptions depends on the accuracy of those assumptions.

### 2.1.4 Empirical Atmospheric Correction

It is possible to improve the accuracy of atmospheric correction with knowledge of the ground or atmosphere. Since my camera system is fundamentally based on measuring the optical properties of the ground, this section focuses on how ground reflectance data can be used with atmospheric correction.

The Empirical line method of atmospheric correction has been demonstrated by Baugh & Groeneveld (2008) to be valid using a large number of data points taken from an airborne platform and by Vaudour et al. (2008), who worked to verify the accuracy of ELM using a larger than average number of sites. Vaudour et al. also confirmed that ELM worked well even when the remotely sensed data was taken at a steep angle. Karpouzli & Malthus (2003) confirmed the validity of ELM at finer resolutions using IKONOS imagery. Qaid et al., (2009) also confirmed its accuracy in their work in Yemen. The empirical line method has been demonstrated to be more accurate than atmospheric modeling methods, such as ACORN and FLAASH (Miller 2002).

Various authors have worked to improve ELM. ELM requires both a light and a dark target to generate the empirical relationship between the digital number (DN) and reflectance. Moran et al. (2001) worked on a refined empirical line method that used in image and radiative transfer methods to eliminate the need for a dark target. Farrand et al,. (1994) found good results with a modified ELM, which used reflectances taken from a spectral library. They compared this modified ELM with the LOWTRAN model, and found LOWTRAN produced worse results, with its output highly dependent on the atmospheric water input. Bartlett & Schott (2009) designed a modified ELM that compensates for clouds in the image, extending the usefulness of ELM. Lach & Kerekes (2008) explored how the angles of surfaces can effect ELM, and how to compensate for these effects. Staben et al., (2012) performed ELM with a quadratic fit, instead of a linear one, on data taken by WorldView-2 with good results.

ELM is a sound basis for verifying other atmospheric corrections. It uses data that is relatively easy to gather and provides superior and more consistent results than corrections based on assumptions. However, current methods of gathering that ground data are too time consuming. The focus of this dissertation is to find a faster way to sample an area to be used with ELM, and I focus specifically on vegetated surfaces

## 2.2 Vegetation

### 2.2.1 Vegetation Reflectance and Health

Large uniform areas of vegetation, managed for food or recreation are common in many parts of the world. These areas have been shown to be valid for use with ELM (Moran et al., 2001). Managed grass in particular has been found to be a pseudo-invariant surface, with good spectral and temporal stability (Clark et al., 2011).

A large body of literature exists studying the optical properties of vegetation. Gates et al.,(1965) wrote one of the early papers on the spectral properties of plants, discussing their reflectance, absorption, and the internal structure responsible for these properties. Understanding the relationship between vegetation's internal properties and its optical properties enables researchers to monitor vegetation health using remote sensing. One of the earlier studies in this field tried to classify separately blighted and healthy corn (Kumar & Silva 1974). Since then, there has been work to relate multispectral remotely sensed data to vegetation quantity (Curran, 1980), chlorophyll content and nitrogen uptake (Bell et al., 2004), and water stress (Sonmez et al., 2008). In the aid of this process, many vegetation indices attempting to measure vegetation health have been generated, such as NDVI and SAVI. These have been cataloged in some detail by Bannari et al., (1995).

### 2.2.2 Vegetation BRF

The bi-directional reflectance distribution function (BRDF) and bi-directional reflectance factor (BRF) of vegetation are of particular interest to this project, where reflectance data are taken over a range of angles. For a given set of input and output angles, BRDF is the percent of light reflected, while BRF is the ratio of the light reflected and the reflectance that would be expected for a perfect Lambertian target. The quantities can be related by the equation (Schaepman-Strub, 2006):

$$BRF = \pi * BRDF \qquad \text{Eq (2)}$$

Many researchers prefer the terms BRDF. My own research has been built upon PROSAIL, however, which produces BRF values. I will use the two terms where appropriate for the work being cited.

In remote sensing, measuring the BRDF of vegetation is already important, as demonstrated by Bacour et al., (2006) normalizing remotely sensed data’s BRDF effect to aid monitoring vegetation cycles. I utilized this field of research to guide my own use measurements of reflectance at multiple angles. BRDF measurement at different wavelengths have been used to characterize vegetation in the same way that measurements of at-nadir reflectance have (Kriebel, 1978 ; Geiger et al., 2001). Sandmeier et al. (1998a) related the physical characteristics of erectophile grass lawns and planophile watercress canopy to their hyperspectral BRDFs, using the laboratory goniometer system at the European Goniometric Facility (EGO). From data gathered like this, models of vegetation were developed, including the Kuusk (Nilson & Kuusk, 1989), Walthall (Walthall et al., 1985) and Roujean (Roujean et al., 1992) models. Wanner, Li, & Strahler (1995) provided some approximations to these BRDF models, to enable them to be used in a linear, kernel driven, form (Figure 3). Kernels enable the use of a simple analytic inversion to the model (Lewis, 1995 ; Wanner et al., 1997). This BRDF model was used with the satellites MODIS and MISR and became the AMBRALS model (Strahler & Muller, 1999).

Improvements to BRDF modeling have continued. Jin et al. (2002) explored combining MODIS and MISR BRDF data to better estimate surface BRDF, demonstrating the value to having more data points in a BRDF estimate. Martonchik, Pinty, & Verstraete (2002) corrected one of the equations used by Jin et al., further improving these results. Liangrocapart & Petrou (2002) developed a two-layer model of BRDF, taking into account the vegetation layer and the bare ground or leaf litter beneath. Snyder (1998) meanwhile worked to extend the Roujean and Wanner models of BRDF into the thermal infrared, where these models are often much weaker.

BRDF models must incorporate some estimate of the hot spot in vegetation reflectance, which is an area of increased reflectance in the retroreflection direction. Hapke et al. (1996) helped define the cause of the backscattering hot spot in various surfaces. Camacho-de Coca et al. (2004) measured the hot spot using POLDER and HyMap on an airborne platform and did some modeling of this effect. They found that these results matched those found by sensors on satellites, showing the hot spot is a scale-free feature. Maignan et al,. (2004) used POLDER data to look at the BRDF of a wide range of surfaces, and compared the performance of several linear models, such as the Roujean and Ross-Li models used by AMBRALS, as well as a non-linear one. They found that none of these accounted well for the hot spot, though the Ross-Li and non-linear models worked comparatively well. They further found that a modified Ross-Li could model this hot spot precisely.

All these BRDF models so far assume light behaves identically regardless of wavelength. This is clearly not the case, as all vegetation is highly reflective in the infrared, resulting in multiple scatterings that would not occur in the visible. To compensate, models have been developed which account for the spectral properties of plants and use these properties in the estimation of the BRDF. A prominent example of this kind of model is PROSAIL (Jacquemoud et al., 2006). The spectral part of this model was built on PROSPECT, developed by Jacquemoud & Baret (1990). The BRF is built on the SAIL (Scattering by Arbitrarily Inclined Leaves) model (Verhoef, 1984). Work continues on refining these models (Feret et al., 2008) and relating spectral changes to biophysical changes in plants.

While important as a BRF model, PROSAIL has also been used as means of assessing the underlying vegetation health. While this is not the focus of my own work, it does present an additional use that would be available for a BRF camera. Many of these papers also provided insight to how to invert PROSAIL. Weiss et al. (2000) used SAIL and measurements at multiple angles to estimate Leaf Area Index (LAI) and chlorophyll content. Because of the lack of an analytic inverse to SAIL, they had to use a look-up table (LUT) solution. PROSAIL has inherited this lack of an analytic inverse (Jacquemoud et al., 2009). When Darvishzadeh et al. (2008) used PROSAIL to estimate LAI and chlorophyll content, they also used a LUT solution which they compared with results for a non-PROSAIL method (Darvishzadeh et al., 2008). L. Wang et al. (2013) used multiple angles, PROSAIL, and a LUT inversion to aid retrieval of vegetation parameters, and tried to find the optimal angles to take spectral data. Si et al. (2012) applied similar techniques for looking for LAI, canopy chlorophyll content and leaf chlorophyll content using multispectral data gathered by the MERIS satellite. They too used a LUT inversion of the PROSAIL model. Since there are a large number of parameters in the PROSAIL model, and some distinct combinations of them may produce spectrally similar profiles, work has gone into limiting the range of its input variables. Vohland & Jarmer (2008) found that linking Dry Matter Content (DMC) and the Equivalent Water Thickness (EWT) in a 1:4 ratio enabled better retrieval of DMC and EWT, as well as other parameters. All these papers provided guidance to my own LUT inversion of the PROSAIL model.

It is important to verify the research done in modeling BRDF or BRF for vegetation. Bacour et al. (2002) designed a method for the comparison of BRDF models and used it to compare the performance of PROSPECT when combined with four BRDF models, including SAIL, finding close performance except for the Kuusk model. Methods are also important to the process of measuring BRDF, which is why Sandmeier et al. (1998b) did a sensitivity analysis of the hyperspectral BRDF of these grasses to various measurement factors, such as sampling rates, change in sun position and Lambertian assumptions. In a multi-year effort to compare and improve BRDF models of vegetation, there was Radiation transfer Model Intercomparison (RAMI) (Commission, 2014), which tested many models over increasingly complex surfaces.

The polarization BRDF (pBRDF) is also of interest to this dissertation. Since the camera is wide angle, there was a question of whether Fresnel reflection would be a significant source of error. Work has gone into measuring pBRDF on the ground (Georgiev et al., 2011; Shell II, 2005) and remotely (Fabienne et al., 2009), relating this to the total BRDF (Georgiev et al., 2010; Zhang & Voss, 2009). Calculations based on these data show pBRDF should not be a concern for this project.

While much work has gone into modeling vegetation, and in spite of its stability in the long term (B. Clark et al., 2011) it is still important to take in-situ measurements of reflectance if vegetation targets are to be used in ELM. K. Anderson, Dungan, & MacArthur (2011) demonstrated that the hemispherical conical reflectance factors (HCRFs) of vegetation surfaces gathered by spectroradiometers in the field showed significant variation in the field from their specifications in the lab. In addition, they found that readings varied more than expected from instrument to instrument. This is also true of pseudo-invariant surfaces. In another study by K. Anderson & Milton (2006), they found that a disused airfield made of weathered concrete, which would generally be assumed to be a target of constant reflectance, showed both seasonal and daily variations in its reflectance values. These variations were ± 7% absolute reflectance seasonally, and ± 1.0% daily at a wavelength of 670 nm.

The use of measured vegetated surfaces is not completely novel to atmospheric correction, but is one that seems to be currently underutilized. The literature studying these surfaces is extensive. This dissertation makes use of this literature to extend existing techniques in situ for long term radiometric monitoring into a new region.

## 2.3 In-Situ Systems

### 2.3.1 Systems for BRDF Measurement

My proposed camera system must use its measurements to estimate BRF in order to relate all of the samples it takes across a scene to a single near-nadir reflectance. General practices for in-situ measurements of reflectance and the BRDF of vegetation were laid out by Robinson & Biehl (1982). Vegetation BRDF measurement is frequently done with a goniometer, moving a spectroradiometer in a hemisphere around a sample, such as developed by Boucher et al. (1999), which they used to verify the accuracy of BRDF models. Examples of goniometers include the  Swiss Field Goniometer system (FIGOS), and the Sandmeier Field Goniometer (SFG) (Sandmeier & Itten, 1999 ; S. R. Sandmeier, 1999). Jensen & Schill (2000) used the SFG to find and model the BRDF of smooth cordgrass, to gather more information about its hyperspectral and directional properties. As goniometers can be quite expensive, Coburn & Peddle (2006) wrote up a method of constructing a low cost, but un-automated, goniometer system for either field or lab use. The use of a goniometer also limits which surfaces can have their BRDF measured. A SFG is around three meters tall; consequently it cannot be used to measure the BRDF of a forest. This motivated Dymond & Trotter (1997) to use an early BRDF camera to measure the BRDF of a forest from an airborne platform. Nandy, Thome, & Biggar (2001) used a calibrated a camera to measure the BRF of a variety of surfaces in the desert. This camera had filters designed to match those of Landsat 7 ETM+ and a near 180° field of view and included a cooling system to keep down read noise. It turned out to be too cumbersome to deploy. Czapla-Myers, Thome, & Biggar (2009) tried to implement another RSG BRF camera, using an off the shelf consumer grade sensor. Unfortunately, this camera had proprietary and inherent image processing built into it, which made the BRF recovery process difficult. One interesting alternative way to measuring BRF was demonstrated by Thome et al. (2008), in which they measured BRF using a stationary one-pixel sensor. By leaving it out for months and letting the sun do the moving, instead of the sensor, the BRF could then be estimated. This, of course, assumes a very static surface.

While there is great trust in the radiometric resolution of spectroradiometers, Ferrero, Campos, & Pons (2006) demonstrated that you can achieve very good radiometric calibration of a camera CCD as well, as long as the temperature is controlled, and the field of view is narrow. We cannot place a 230 kg goniometer (Sandmeier & Itten, 1999) on top of crop plants we wish to measure the BRDF. This motivated Demircan et al. (2000) to use a rotated line CCD to take BRDF. This latter experiment also demonstrated the way that using multiple pixels can speed up the BRDF measuring process, as the measurements with their system took 30 seconds. Cameras have become important to measuring BRDF when the time taken to gather readings becomes a significant issue. This is an issue when measuring a time varying BRDF, like paint drying (Sun et al., 2007), or when taking measurements in a difficult environment, such as underwater (Voss et al., 2000). It should already be the case for many in-situ readings, where the sun is continuously moving.

Time is a factor for people trying to gather large quantities of data, such as people looking at the polarization BRDF (Shell II, 2005). Goniometers have provided BRDFs with high spectral resolution but are limited by their run time. To work around this runtime issue, Filip et al. (2013) developed a novel algorithm to sample BRDF, sparsely sampling BRDF at first, then taking additional samples where the rate of change is high, and therefore decreasing the large number of samples typically needed to sample BRDF. This might be something to consider in future implementations of the BRDF inversions that I use for this camera system, as I currently sample at evenly spaced intervals.

Much work has been done to improve BRDF cameras in labs, using high dynamic range cameras (Kim et al., 2009), novel lighting geometries (Ghosh et al., 2010) and polarization from multiple light sources (Atkinson & Hancock, 2008). An item of interest for later study with this sort of project may be work into accounting for spatially varying BRDF (Dana & Wang, 2004).

Most of these BRDF cameras, including an early example from Marschner et al, (2000) have been built to work in the laboratory, to help improve computer graphics. Many of the in-situ instruments for measuring vegetation BRDF for remote sensing, such as the one developed by Giardino & Brivio (2003), seem to still be Goniometers. This dissertation is part of an effort to move some of this technology from in the lab into the field with in situ camera systems.

### 2.3.2 In-Situ Camera Systems

In-situ optical monitoring systems are often limited to continuous at-nadir radiance or irradiance. To monitor larger areas with such a sensor, Berry et al. (1978) set up such a radiometer to run on 150-foot wires between 50-foot towers. More recently, Gamon et al. (2006) set up a spectroradiometer on a rail, which samples approximately a 1 meter by 100-meter area. G. E. Bell et al. (2002) came up with another solution, using a radiometer and light source mounted on a tractor to monitor turfgrass. These approaches to monitoring large areas are limited by the time that can be invested in moving the sensor from place to place, and the infrastructure required to move them between those places. One exception to this is the system designed by Hilker et al. (2011) that used a rotating imaging spectroradiometer to estimate the chlorophyll and carotenoid content of deciduous and coniferous vegetation, and their growing patterns.

In-situ cameras provide an alternative means of monitoring optical properties. One example is an automatic grass monitoring system designed by Schut et al. (2002), that looks at 3.5 $m^2$ area with pixels on the order of one mm and hyperspectral data, trying to measure the percent grass versus soil and dead material. As another example, Voss & Chapin (2005) developed the NuRADS camera system, which was designed to measure the upwelling radiance distribution in ocean water, and has a field of view over 80°, 6 spectral channels, and takes readings in 2 minutes. NuRADS was used by Gleason et al. (2012) to measure the BRDF of water. This system was later modified by Voss & Souaidia (2010), to make use of multiple NuRADS sensors to measure the upwelling polarization of the ocean and by Bhandari, Voss, & Logan (2011) to measure the downwelling polarized radiance in the ocean. An in-situ system from Wei et al. (2012) measures seawater radiance near the surface, with a 180° field of view. It takes advantage of CMOS technology to have a dynamic range of up to 9 decades. These cameras are all just for the measurement of BRDF or radiance though. Unlike the above systems, my camera system will be working over just part of the hemisphere, and will supplement the data gathered with existing BRDF models.

All the camera systems listed so far have been temperature stabilized. There is a change in camera responsivity with temperature, but this seems to be little noted since many cameras are already cooled to control other sources of noise. This effect is notable in some sensors in orbit, such as the Lunar Reconnaissance Orbiter Wide Angle Camera (Sato et al., 2013) and Landsat 5 (Helder et al., 2004). Algorithms have been developed to compensate for this effect.

Satellite sensors have to deal with issues of spectral mismatch in cross-calibration (P. M. Teillet et al., 2007). This is one of the largest sources of noise in cross-calibration (Chander, Helder, et al., 2013). Algorithms have been developed to compensate for this effect (Chander, Mishra, et al., 2013). These will guide my work if issues do arise due to the mismatch between my filters and the Landsat 7 ETM+ ones.

If it proves possible to do atmospheric correction using web camera images, it may be possible to pair with some of the many cameras already set up to monitor the world. Some existing and proposed networks of cameras are set up to monitor phenological changes (Richardson, et al., 2009 ; Benton, et al., 2008). Cameras are already being used to monitor haze and air pollution ("Camnet," 2012). Individuals, parks, companies and universities also place a large number of outdoor cameras to show traffic, weather, views, or wildlife. Jacobs et al. (2009) have done extensive work on locating these cameras, both on the web, and their corresponding location in the real world. The cameras cataloged by Jacobs et al. produce around one terabyte of images every 2-3 days, which are then stored and accessible at AMOS (Archive of Many Outdoor Scenes) ("AMOS | Project Overview," 2013).

### 2.3.3 Vicarious Calibration Systems

Vicarious calibration is the process of measuring the response of sensors that we do not have physical access to, such as those on satellites. The processes used for ELM and vicarious calibration are related. ELM compensates for the atmosphere in a single image. Vicarious calibration takes similar measurements of in-situ reflectance, but uses another layer of atmospheric correction, enabling the effects of the atmosphere to be separated from the properties of the sensor being calibrated. Vicarious calibration is of interest to this dissertation because it requires the same reflectance data ELM does.

Vicarious calibration is important to maintaining a continuous record of reflectance measurements, tracking changes in sensor sensitivity (Helder et al., 2004) and tracking artifacts in remotely sensed data (Helder & Ruggles, 2004). It can be used to estimate the MTF or other optical properties of sensors (Pagnutti et al., 2010). It maintains data continuity between missions, by relating the readings from previous sensors to newer ones (Helder et al., 2012), and improves temporal sampling by relating readings between current sensors (Thome, D’Amico, & Hugon, 2006) and can be done very accurately using existing methods (Thome, Mccorkel, & Czapla-myers, 2013). Vicarious calibration can also provide validation of data products produced by satellite systems (Y. Wang et al., 2011).

The Remote Sensing Group (RSG) at the University of Arizona has been practicing vicarious calibration on satellites for years (Thome et al., 2004 ; Czapla-Myers et al., 2013), and has helped establish standards for the practice (Helder, et al., 2012). To aid in vicarious calibration the RSG has designed many optical devices, to inter-calibrate radiance readings (Anderson, et al., 2008), automatically take at-nadir radiance readings using LED and silicon sensors (Czapla-Myers et al., 2012 ; Anderson et al., 2013), estimate the BRF of surfaces (Nandy, 2000) and measure laser reflectance for the vicarious calibration of LIDAR systems (S. Biggar, et al. , 2004).

Pseudo-invariant sites are an important part of vicarious calibration (Helder et al., 2013), with significant effort being put into identifying suitable sites manually (P. M. Teillet, et al., 2007 ; Chander et al., 2010 ; Angal, et al., 2011) and automatically (Helder, Basnet, & Morstad, 2010). To monitor these sites, a balance must be found between their suitability and their accessibility (Thome, Geis, & Cattrall, 2005). Different sites may be necessary depending on the bands being calibrated. The alkali flats of White Sands provides good stability for much vicarious calibration (Holmes & Thome, 2001 ; Teillet, et al., 2007),while Lake Tahoe presents a suitable target for calibrating thermal bands (Hook et al., 2004). Bright targets are often preferred, but dark targets have also been used (Parada, Thome, & Santer, 1997; Thome, et al., 2000). If only some of the spectrum can be vicariously calibrated, it is also possible to intercalibrate sensors using sun glint (Hagolle, et al., 2004). In 2001, P. Teillet et al. (2001)

proposed a network of automated test sites to be used for the calibration of satellite sensors, though this appears to have never gone beyond being a proposal. There is ongoing work to create a calibration standard in space (Thome et al., 2010 ; Lukashin et al., 2013). This mission should launch in 2020 (“CLARREO,” n.d.).

Current vicarious calibration methods demonstrate the desirability of having a historical basis of ground readings to compare remotely sensed data against. However, vicarious calibration focuses on arid regions, where there is high uniformity and little change. In this way, sampling a small section can be relied upon to provide information about a larger target. This dissertation seeks to expand the range of existing experiments, moving techniques out of the lab, and out of arid regions. It seeks to expand the usefulness of the system using information technology, in the place of hardware, keeping costs down. It does all this in order to provide an improved methodology towards the validation of atmospheric correction.

# 3 System Design and Calibration

## 3.1 Overview

My research expands the range of a number of existing experiments: Many techniques developed using cameras to measure BRF are currently limited to being used in a lab environment. I apply the extensive work that has been done characterizing vegetation, using readings taken over a range of angles, to move existing techniques for monitoring in-situ reflectance out of arid regions. I increase the usefulness of the camera system, using information technology in the place of expensive hardware to keep costs down. Since there are many possible selections of cameras, color filters, BRF model, lenses, etc., this research characterizes how these choices can be made and affect the quality of the overall system. It is my hope that by doing this, that I can create a road map for future efforts to build in-situ cameras for atmospheric correction.

Section 3.2 explains how the BRF models used by the camera system were inverted, which is the first step to transforming camera images into an estimate of near-nadir reflectance. Section 3.3 explores how these inversions provide insight into the way sources of error in the camera system effect the near-nadir recovery. Sections 3.4 and 3.5 describe how the relationships found between sources of error and the error in the BRF recovery determined the camera design and Lambertian target selection. Finally, Section 3.6 explains the calibration process for the two camera systems.

## 3.2 BRF Model Inversion

### 3.2.1 Introduction

BRF models provide a means of estimating directional reflectance for a given input radiance. BRF models are frequently built with input parameters so that they can be adjusted to better fit an individual instance of a surface. To make these inputs useful, a method is needed for finding input values that create a model close to reality.

A convenient way of finding input values is to use data gathered about the reflectance of the real surface. This requires inverting the model, using what would be the output of the BRF model to estimate the input values that would provide that output. Inversions can be analytical, mathematically relating the measured values to a specific set of input values for the BRF model, frequently deriving from a least squares fit. Inversions can also be non-analytical, such as with look-up tables, iterative or search algorithms and artificial neural networks.

### 3.2.2 AMBRALS Inversion

The AMBRALS model was developed to provide BRDF estimates from data provided by the MODIS and MISR satellite-borne sensors. The BRDF model is built upon a sum of multiple kernels that represent different surfaces and forms of scattering. It is assumed that these surfaces are non-interacting, and thus, can be treated as independent of each other. The BRDF model can be defined as

$$BRDF(\theta_i, \theta_v, \phi, \Lambda) = \sum_{k=1}^{n} f_k(\Lambda) K_k(\theta_i, \theta_v, \phi, \Lambda) \qquad \text{Eq (3)}$$

Where $\theta_i$ is the solar zenith angle, $\theta_v$ is the view zenith angle, $\phi$ is the view-sun relative azimuth angle, $\Lambda$ is the waveband, $K_k(\theta_i, \theta_v, \phi)$ is the BRDF model kernel k and $f_k(\Lambda)$ is the BRDF model kernel weight (Figure 3) for parameter k in waveband $\Lambda$, (Strahler & Muller, 1999). N AMBRALS kernels are superimposed to find the BRDF. Usually three kernels are used: one with constant reflectance, representing isotropic scattering, one for volume scattering and a third kernel for surface scattering. The BRDF model is then fit to the $l$ measurements of reflectance data $\rho'_l$ with weights $w_l$ by a least squares fit, to find the kernel weights $f_k(\Lambda)$. We can simplify this notation some by defining $K_{kl}$ to be the reflectance for a particular pair of incident and view angles for the measurement $l$, so that:

$$BRDF_l(\Lambda) = \sum_{k=1}^{N} f_k(\Lambda)K_{kl}(\Lambda) \qquad \text{Eq (4)}$$

The inversion is found by first deriving matrices of based on the data. It is then possible to rearrange these such that they can be used to derive the values for $f_k(\Lambda)$.

$$V_j = \sum_{l=1}^{N} \frac{\rho_l' K_{jl}}{w_l} \cong \sum_{l=1}^{N} \frac{BRDF_l K_{jl}}{w_l} = \sum_{l=1}^{N}\sum_{k=1}^{N} \frac{f_k K_{kl} K_{jl}}{w_l} \qquad \text{Eq (5)}$$

$$M_{jk} = \sum_{l=1}^{N} \frac{K_{jl} K_{kl}}{w_l} \qquad \text{Eq (6)}$$

Which can then be rearranged to find the inverse:

$$V_j = \sum_{k=1}^{N} M_{jk} f_k \qquad \text{Eq (7)}$$

$$f_k = \sum_{j=1}^{N} M_{jk}^{-1} V_j \qquad \text{Eq (8)}$$

For more details on this inversion, see Strahler & Muller (1996) page 34/252. This inversion has the advantage of having a definite value for input parameters, so long at the matrix $M_{jk}$ can be inverted.

### 3.2.3 PROSAIL Inversion

PROSAIL is a BRF model built on the leaf reflectance model PROSPECT, and the BRF model SAIL. PROSPECT is a hyperspectral model of leaf reflectance and takes into account chlorophyll and pigment contents. SAIL simulates multiple scatterings by arbitrarily inclined leaves for values of leaf density (Leaf Area Index) and the Leaf Angle Distribution. These combine to act as a hyperspectral vegetation BRF model. The strength of this model is that it can better account for the relationship between vegetation parameters and BRF effects. Increased reflectivity leads to multiple scatterings, consequently BRF is different in the visible, where reflectance is low, vs. the NIR, where reflectance is high. BRF effects in the visible change and get closer to those in the NIR when vegetation becomes distressed, and reflectances in the visible and NIR thus become more similar.

PROSAIL is a program simulating multiple scattering, not a set of mathematical equations, and so a non-analytical inversion was necessary. Options for this inversion include the use of artificial neural networks, iterative algorithms and the use of look-up tables. For this research, I used a look-up table (LUT) inversion of the PROSAIL model. A LUT inversion provided the most straightforward non-analytic inversion and has been demonstrated by others in the field, as both artificial neural networks and iterative algorithms are complex enough to be fields of research unto themselves. In addition, the LUT inversion of PROSAIL has been demonstrated to by others in the field (Darvishzadeh et al., 2008; Si et al., 2012; L. Wang et al., 2013).

For a LUT inversion, many possible example BRFs are generated, for a range of input values for PROSAIL. By comparing the BRF measured with the example BRFs in the LUT, it is possible to find input values that most closely approximate the BRF. Using these input values for the closest BRF, it is then possible to estimate the reflectance in other directions.

One advantage of the LUT inversion of PROSAIL is that it provides an opportunity to conform with the surface reflectance in a way that other inversions do not. Vegetated surfaces will have some non-uniformity to them. Simulations show that this can be a significant source of error in the BRF recovery, but one that can be overcome. My PROSAIL LUT inversion uses a number of closest BRF examples to estimate reflectance, in line with the work done by (Weiss et al., 2000). An average of the directional reflectance is calculated using reflectances generated for each example BRF in the desired range of closest estimates. By using multiple example BRFs in the solution, the inversion is better able to account for surfaces divided between different surface types, grass and soil for instance. The LUT inversion will pick grass BRF examples and soil BRF examples, and produce and average of those, in a way similar to how the net reflectance is seen by a distant sensor.

The main disadvantage of the LUT inversion is the size of the look-up table. Each table is made up of examples generated using different input values, in this case, example BRFs. A finite number of examples can be generated, limited by the time that can be spent generating them, and the space that can be dedicated to storing them. Additionally, increasing the number of examples in a table increases the amount of time that must be spent searching for examples that match the measured data.

The limits on the number of examples also limit the number of input value combinations that we can test. It is important then to pick the input values used to generate examples that represent both the range of possible examples and input values well. When (Weiss et al., 2000) populated their look-up tables, they used 100,000 number of randomly assigned values for inputs. I could not find a good justification for this choice, so instead I generated example BRFs that were using input values spaced evenly between the minimum and maximum values (Table 2). These minimum and maximum values taken from estimates used by Darvishzadeh et al. (2008) and Si et al. (2012). When the final analysis of the data was done, I changed these ranges based on data taken from the field (section 3.6.11: LUT Calibration).

*Table 2: List of input values used for the PROSAIL inversion, for the simulation.*

| INPUT VARIABLE | MINIMUM VALUE | MAXIMUM VALUE |
|---|---|---|
| **LEAF AREA INDEX** | $4\ m^2\ m^{-2}$ | $8\ m^2\ m^{-2}$ |
| **LEAF INCLINATION DISTRIBUTION FUNCTION** | 20 | 70 |
| **SOIL REFLECTANCE PARAMETER** | .5 | 1 |
| **CHLOROPHYLL A AND B CONTENT** | $15\ \mu g\ cm^{-2}$ | $55\ \mu g\ cm^{-2}$ |
| **LEAF STRUCTURE PARAMETER** | 1.5 | 1.9 |
| **EQUIVALENT WATER THICKNESS** | .01 cm | .02 cm |
| **DRY MATTER CONTENT** | $.0025\ g\ cm^{-2}$ | $.005\ g\ cm^{-2}$ |
| **CARATEONOID CONTENT** | $8\ \mu g\ cm^{-2}$ | $8\ \mu g\ cm^{-2}$ |
| **BROWN CHLOROPHYLL CONTENT** | $0\ \mu g\ cm^{-2}$ | $0\ \mu g\ cm^{-2}$ |
| **HOTSPOT PARAMETER** | $.1\ mm^{-1}$ | $.1\ mm^{-1}$ |
| **SKYLIGHT PARAMETER** | .1 | .1 |

Some of the variables in Table 2 have the same minimum and maximum values. Because of the eleven inputs necessary for PROSAIL, sampling the range of all possible input values thoroughly while maintaining a limited number of examples for the LUT is difficult. To have N values for each input represented in the LUT, with 11 inputs, there will be $N^{11}$ possible combinations, and thus example BRFs to generate. For N = 2, this is 2,048 example BRFs. For N = 3 this is 177,147 example BRFs. Eliminating some of these inputs decreases the number of example BRFs that need to be generated substantially, and thus enable better sampling of input values elsewhere.

Brown chlorophyll content, the hot spot parameter, and carotenoid content were eliminated as an input because they have been found experimentally by other research groups to be fairly constant. The skylight parameter can be estimated using local measurements at the time of taking readings. Finally, there is the observation by (Vohland & Jarmer, 2008) that BRF recovery results are improved by pegging dry matter content to being 1/4 of equivalent water thickness. This lowers the number of variables from 11 to 6, substantially reducing the number of examples that need to be generated for a LUT.

To try and further limit the number of input values, I performed a sensitivity analysis to estimate the magnitude change of in the example BRF when an input value was moved from its maximum to minimum value for a range of other input variables. By comparing the magnitude of these changes, I hoped to determine if I could sample some inputs less than others. My results, however, showed that the remaining six variables had roughly equal weight when all the Landsat 7 ETM+ bands and a hemisphere of angles were considered.

The BRFs generated for my inversion of PROSAIL were multispectral readings at a wide range of angles. As an additional change to other methods I have seen implementing the LUT inversion for PROSAIL, I experimented with giving different weights to different parts of the spectrum. As stated elsewhere, this multispectral data helps better understand the underlying health and parameters of the vegetation being measured, which we might expect to aid in the BRF recovery. However, since there were three bands in the visible, and one in the NIR, I anticipated that this might lead to results that overweight the visible over the NIR. As the error in estimated reflectance tended to be greatest in the NIR, I set up my inversion such that I could shift the weight given to each band. This enabled me later to experiment with these weights, to see if adding additional weight to the NIR provided a better inversion than one where the weights were equal across the bands.

Because of the large number of example BRFs being generated for this work, additional work was done to optimize the run time of the example generation and match searching code. This work is explained in Appendix A.

## 3.3 Systems Engineering and Error Estimation

### 3.3.1 Introduction

Proper planning is an important step to the success of any project. I took a systems engineering approach to this, simulating the system before designing it. This enabled me to first confirm the feasibility of this method of near-nadir reflectance recovery, and then to maximize the chances of system success while avoiding overdesigning parts unnecessarily and staying within the project budget. Error from different sources was estimated, and these estimates were used to decide the parts, calibration, and data taking methods used in the camera system. This section of the dissertation describes the major sources of error, the methods used to estimate error, how sources of error were weighed against each other, and the camera system design they produced.

### 3.3.2 Finding the Error Budget Target

To perform the systems engineering for this project rigorously, the allowable error in estimated near-nadir reflectance needed a target value. Since these cameras are intended to perform and evaluate atmospheric correction, the relationship between a camera's error in its recovered near-nadir reflectance, and the quality of the resulting atmospheric correction, needed to be understood. Research on the empirical line method (ELM) provides guidance here, as it uses only in-situ spectral reflectance data to do atmospheric correction. ELM literature is contradictory on the requirements for ground targets (B. Clark et al., 2011 ; Smith & Milton, 1999 ; Karpouzli & Malthus, 2003), so I relied instead on a Monte-Carlo simulation of ELM. These simulations enabled me to relate the quantity of cameras and the brightness of targets to the quality of the resulting atmospheric correction.

The simulation worked by comparing an empirical line generated using perfect data to an empirical line generated using noisy data. The simulation generated N calibration targets to be used in an empirical line with reflectance values. Each of these calibration targets was assigned an average error in the estimate of its reflectance. The error was related to the reflectance such that larger values of reflectance would on average have larger values of σ as well. This was consistent with taking real measurements of reflectance and prevented situations where low values of reflectance might produce readings with negative reflectance values. The simulation generated noisy estimates of the reflectance, and used these to generate an estimate of the empirical line. The simulation compared the noisy estimate with the perfect line to generate an RMS error for the run. The simulation would then repeat the process of generating noisy estimates for the reflectance values 1000 times to find an average value of RMS error for N calibration targets with reflectances. The simulation would record this value in a file along with the reflectances and mean error for each of the N targets used in the run.

The simulation generated 1000 random possible set ups with different numbers of calibration targets, reflectances, and average errors. By plotting and combing through this data it was possible to find patterns in the relation between these values. As would be expected, larger numbers of cameras enable looser tolerances in the average error of the camera systems. Also in line with research on ELM, it is possible to get better results with fewer targets if there is a large difference in the reflectances of the targets (Moran et al., 2001). Results showed average RMS errors between the lines below 2% were uncommon, and the absolute limit seems to be an average of 1% RMS error between the lines. Using these results as a guide, I have decided that the error in the camera reflectance estimate should be below 2% (in absolute reflectance, so that the error in an estimate of 50% reflectance should be 50% ± 2%, not ± 1%), as this provides low error in the atmospheric correction while requiring a small number of cameras. (Figure 4)

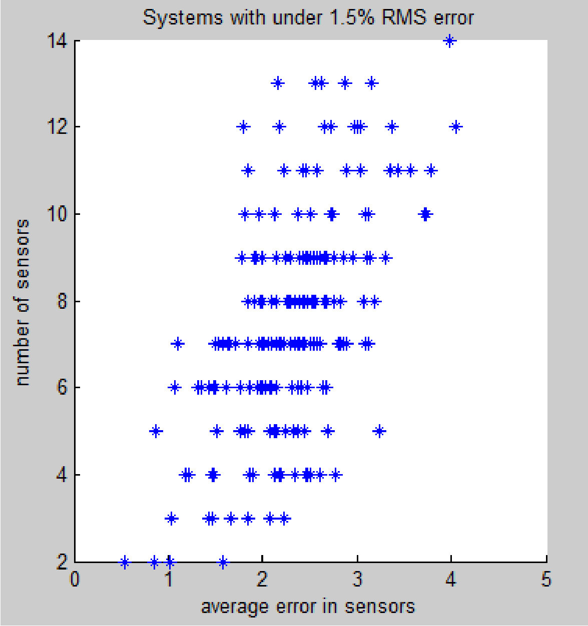

*Figure 4: A scatter plot showing how average allowed error in a camera system (1 sigma, % absolute reflectance) relates to the number of cameras required. The average allowed error also varies with the brightness of the targets, and on the individual camera errors.*

### 3.3.3 Metric Used for Measuring System Error

To aid the design process, I created a simulation of the camera system. The simulation measured a PROSAIL surface and sampled it according to the camera specifications, then tried to recover the BRF using the PROSAIL LUT inverse. A satellite reading of the PROSAIL grass surface was simulated, and the near-nadir reflectance estimated by the PROSAIL inverse was compared with this value. This was performed over a range of satellite values. These were combined into a root mean square as the total system error.

Sources of error were programmed into the simulation to measure their effect on the net error in the BRF recovery. Some level of error was inherent to the system and the simulation, and all estimations of an individual error effect for an error budget were measured from this base error level. When estimating these values, I used four different grass surfaces, generated using random input values plugged into PROSAIL, taken from within the ranges of Table 2 that I deemed were far enough apart to produce significantly different results. Since I did not know the exact health of the grass that I would eventually use, this would enable me to see how the performance varied with surface type, while also limiting the number of simulations I needed to a number that could be run in the time available. I averaged the results of the error for these four surfaces to find the mean value for the total system.

For these simulations, it was necessary to pick a set of parameters to use for generating the LUTs. The full scale camera system is intended to be stationary, and the sun angle will move with respect to it at the time of satellite pass over. In Tucson, AZ, where I ran this experiment, and with the Landsat 7 ETM+ satellite system, at the time of satellite pass over, this would account for an approximately 50° change in the azimuth angle between the sun and camera, and a change of approximately 30° in solar zenith angle between the summer and winter solstice. Since placing the camera in the direction of backscatter presents the problem of the system potentially casting a shadow on its target, I assumed it would be operating in the forward scatter direction. I further assumed that the camera system would work best when it could monitor the forward scatter specular reflection. As such, I ran simulations for the camera at a solar azimuth angle of 180°, with a solar zenith angle of 30°, to represent a best-case scenario. I also ran the same simulations for the camera with a solar azimuth angle or 230° and zenith angle of 60° to represent the seasonal difference in the stationary camera performance.

I found in these simulations that, as expected, the camera performed better at 180° and 30° than it did at 230° and 60°. These changes, while significant, were not so much as to make it seem that the camera system would not work year round.

For the rest of this section, I will be making reference to, and presenting charts for the case of a camera set up at a solar azimuth of 180° and zenith of 30°, because the behavior of these two cases is nearly identical in shape, if slightly different in scale. I do list the differences in the resulting expected errors for both at the end in Section 3.3.14, where I discuss the final error budget in more detail.

### 3.3.4 Error Due to LUT Use

Some amount of error is inherent to the LUT inversion of PROSAIL. It is necessary when estimating the overall error of the system that we measure the error of individual sources, such as read noise and filter choice, that these are measured from these baseline sources of error.

It is also necessary to make some design choices for the set up of the LUT solution, both to implement the problem and to establish this baseline error of the system. When setting up this base system for the simulation, it was sensible to seek an implementation that does not create unnecessarily large sources of error, as this might make error from other sources less apparent, and would ideally also not represent the behavior of the final system. The design decisions that had to be made at this point included the number of samples of the image taken, the sampling of the input values used for PROSAIL in the LUT inversion, the number of BRFs used to find the average used finding in directional reflectance value, and the weights given to each band used in the inversion (see section 3.2.3 for more details).

I began with the sampling rate for the image, and the rate at which to sample the input values for PROSAIL. I desired an estimate of these values prior to running the small scale test, both to aid simulating the effects, and to understand how long I would need to set aside for generating the LUTs for the inversion. I began with what I thought would be a minimum value, sampling the image with an 11 x 11 grid, as this seemed like a minimal amount. A 3 x 3 grid to provide information about the direction of the change in BRF from the center, while a 5 x 5 grid would also provide information about whether the rate of change was increasing or decreasing. Since I had not assumed the angle of specular reflection and maximum value would be in the center of the image, an 11 x 11 grid acts as a 5 x 5 for each quadrant of the image. Testing showed me that this did indeed provide adequate results for the inversion. I used this for all later simulations. For the sampling of the PROSAIL input variables, I varied the value across the range explained in section 3.2.3. I had decided to sample these inputs over an even range and desired a number of samples that seemed a minimum for valid results. I decided that I would use 4 samples over the range for the input values, as this allowed for some variation between the minimum and maximum values, while enabling me to generate LUTs quickly enough that it was possible to run a range of simulations to generate other error values.

For the next step in this, I determined the number of BRFs to use in finding the directional reflectance. Since the tables in the LUT have finite resolution, using a multiple BRF recovered in the LUT inversion enables a finer degree of output in finding directional reflectance. If the measured BRF was in between two example BRFs found in the LUT, then using the sum of the directional reflectance for those two would lead to better results than if we only used one. Similarly, if there was a BRF that was closer to one of the two example BRFs mentioned above, then using a third BRF in the sum might pull the value even closer to the measured values. This argument can be made ad infinitum, though clearly it must also have a limit. If we were to apply every single example BRF used in the LUT, then we would get the same output regardless of the input. I set out to try and find this value experimentally, prior to running other simulations. It would be tempting to find the number of BRF examples to use every time on a case by case basis, but in the field, there will not be reference data to work against. After testing values between 5 and 500 LUTs used, I found that there was not a consistent best value to use. For the rest of these simulations, I ran them using the sum of the 13 best matching BRFs, as this produced good results most often, and seemed enough to gain the benefits of the summation without muddying the results with more distant values. As something to test in the future, I might also weight this summation, such that the closest BRFs are better reflected in the final value.

For the final step in setting up the LUT inversion, I explored the effects of weighting the different Landsat 7 ETM+ bands I used in the inversion. By default, the inversion held the bands to be equal. As the values for the visible tended to be similar to one another, and generally vary less than the NIR, I was concerned that this would overweight the reflectance in the visible. I experimented with different weights for the NIR versus the visible and found that while this did not strongly change the outcome, it did improve the results for the NIR. Since the values in the NIR were most often the largest source of error, I gave increased weight to the NIR values. I found that a 3:1 ratio of weights in favor of NIR over visible light gave the best results. Placing additional weight into the NIR decreased the ability of the PROSAIL inverse to find matching values for the BRF, as it became harder for it to detect things like vegetation health.

### 3.3.5 Error Due to Read Noise

Read noise is random variation in the signal produced by a detector due to quantum mechanic effect, and exists even in a hypothetical perfect system. This is often listed as a specification of the signal to noise ratio for the system, measured in decibels. Read noise can be reduced by cooling the system, or mitigated by increasing the number of images taken and averaging over them. In the case of measuring BRF, the effects of read noise can also be reduced by increasing the number of samples from the image taken, as BRF is generally a smooth function. I chose not to work with a cooled system because for low-cost cameras in the field, cooling will not be an option. As a result, the system tolerance allowed for read noise had to be loose. However, Figure 5 shows how even a small percent of read noise would cause the signal to be drowned out for the signal.

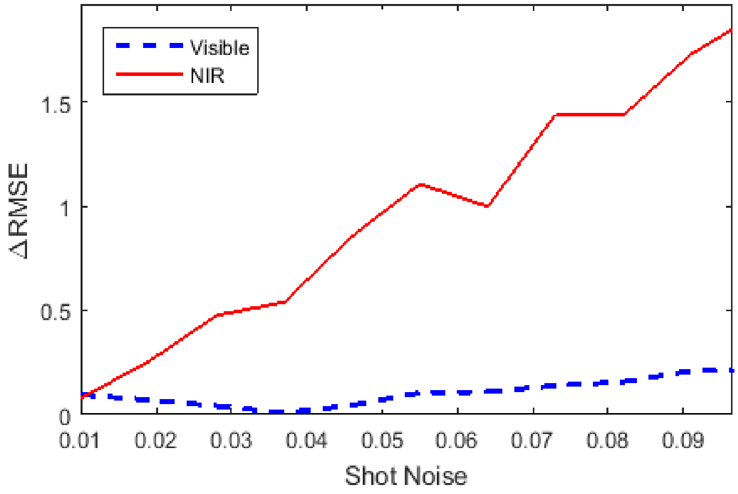

*Figure 5: Simulated results for the change in system error as a function of the read noise. Read noise measured here as a percent of the signal.*

### 3.3.6 Error Due to Error in Angle Measurement

Error from measuring the camera system angles with respect to the zenith and azimuth angles of the camera was considered to be a priority, as an accurate estimate of BRF requires knowledge of the angles from which readings are being taken. This source of system error was broken into two parts: Knowledge of the azimuth and zenith angles of the camera, and knowledge of the roll of the camera system with respect to the optical axis (Figure 6). Error in the zenith angle estimate was anticipated to be low, as it is quite easy to measure with a digital level. The azimuth angle was considered more difficult since it requires knowing the compass direction of the camera system, which is much more difficult to measure. Digital compasses require daily calibration while analog compasses have limitations in their precision. In addition, there is difficulty in setting up to measure this value, given local magnetic fields, and distortion of the magnetic field by equipment. I explain this more in Section 4.1.3. Simulations found the tolerances for the setup and measurement of the azimuth and zenith angles to be fairly loose, particularly in the azimuth direction (Figure 7).

The zenith angle reflects what we would expect for a Lambertian surface, that the brightness is different depending on viewing angle, but changes smoothly with the angle. Azimuth also represents what we know about surfaces in general.

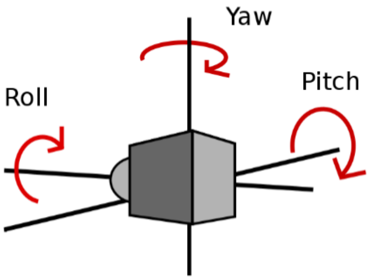

*Figure 6: The roll, pitch and yaw angles for the camera.*

There is increased reflectance in the camera view around the direction of forward and backscatter; in other directions, the reflectance tends to remain symmetric. As the sun angle is known, the results of the inversion will reflect a knowledge of the solar angle, rather than an incorrect measurement of azimuth.

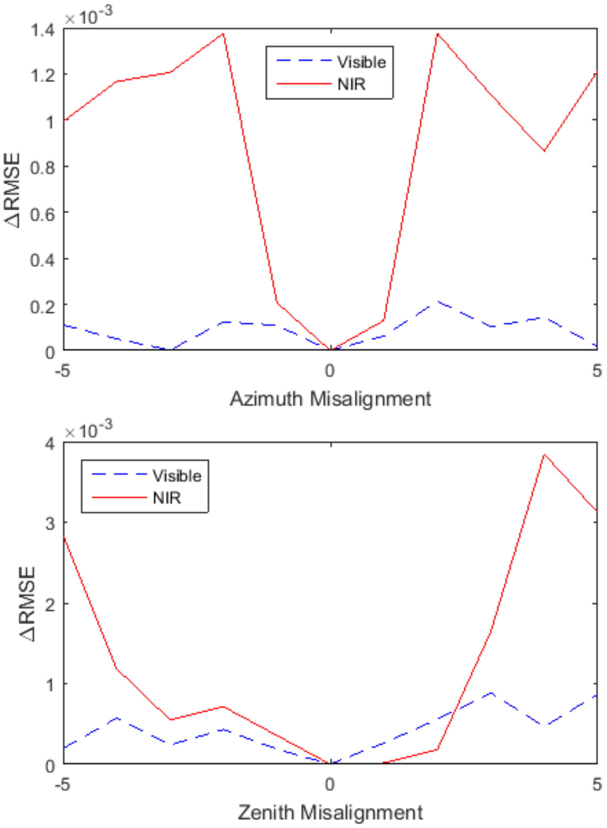

*Figure 7: Simulated results for the change in system error as a function of the misalignment of the camera system in the azimuth and zenith angle with respect to the estimated azimuth and zenith angles.*

This system error analysis showed that while it was necessary to measure zenith angle it would drive the design. It was easy for a digital level to come within 1 degree of certainty in the zenith angle of the camera. The azimuth specifications of ± 5° did end up driving system planning, since analog compasses have a finite level of accuracy, and magnetic fields and local and equipment's effects on the compass need to be planned around. These specifications also drove the time available for taking readings, as it was desirable for the sun to stay within the specification while taking readings for all the color bands. The angular distance traveled by the sun naturally varies with time of year and time of day. In order for the sun angle to stay within this specification, it was necessary to get all the readings for all colors within a span of 5 minutes.

The camera roll was treated as a source of error within the parameters specified for the azimuth and zenith error. The roll angle of the camera system was a weaker source of error than the estimate of the camera's azimuth and zenith angles, though a change in the roll would change for both the phi and azimuth angles measured (Figure 8). The slope of the ground with respect to the camera was treated as being identical to the tilt of the camera with respect to the ground, due to symmetry.

The estimation of camera roll was deemed to be something that could be easily measured, and would have to be, but not an item that would drive the design. The ground slope would also have to be measured, but would not drive the design of the system. I specified that I should have an estimate of this value to within half a degree, for both the ground tilt and the camera roll.

### 3.3.7 Error Due to Pixel Angle Estimate

As in the previous section, the angles of BRF that each pixel is measuring must be known in order to reconstruct the BRF from the image generated by a camera. To do this, it is necessary both to know which way the camera is oriented, as in the previous section, and what the change in the angles is as we move across the pixels in the image plane.

I simulated this error by approximating it as an error in the estimate of the field of view of the system, extrapolating the view angles from that as a linear function. This changed all the angles in the camera by different amounts, while at the same time doing so in a mathematically simple and repeatable way. This simulation provided an estimate of the tolerance of the system to this sort of error, without exploring all the possible ways that the pixel to angle relationship may be wrong. I ignored effects like distortion, since distortion in the image is not a source of error, so long as it is accounted for.

In simulating this effect, it was possible to see that this source of error acts like camera roll, in that a small error in the field of view estimate causes a large change in the error of the system (Figure 9). This corresponds to the way that, like roll, changing the field of view does not cause the readings to move along the BRF surface, but rather distorts the entire estimate.

As a result, the specification for this had to be tighter than the estimate of azimuth and zenith direction of the cameras. The field of view needed to be

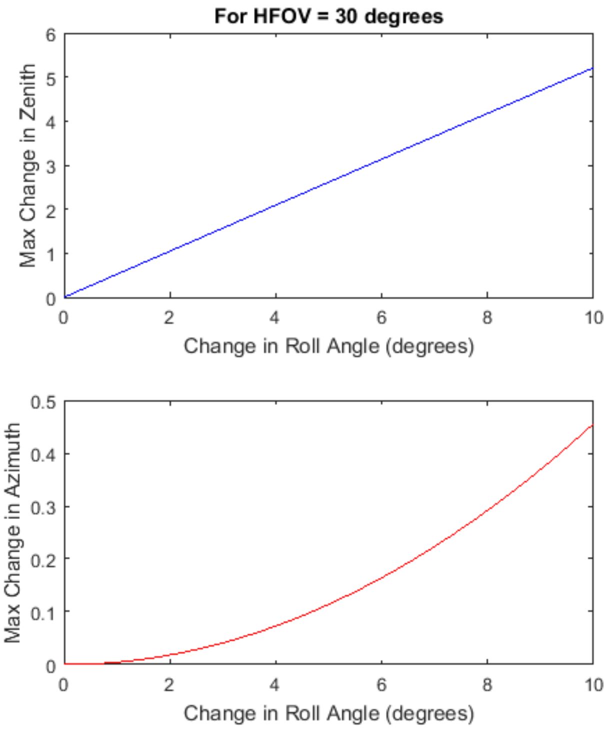

*Figure 8: Estimates in the maximum change in the azimuth and zenith angles (in degrees), produced by changes in the roll angle of the camera.*

known at ± 1.5° in either the azimuth or zenith directions of the camera readings. Even this value was pushing the error budget. I sought to get well below this value.

One factor that was not included in this is that there is some error in the estimate of the angle for each pixel and that this may not be a linear relationship. In Section 3.6.2 we can see that the fit for the angle to pixel ratio is such that there are values both above and below it.

### 3.3.8 Error Due to Digitization

It is necessary at some point to save our data as a digital number. Usually, this limitation is stated as the maximum number of bits. If read noise is low or averaged away, the digitalization will define the maximum radiometric resolution possible for the camera system.

To simulate this effect, assumed the measured reflectances spanned the range of values from 0% to 100%, and that these would discretize according to the number of bits of the system, such that for an 8-bit image, there were steps of approximately 0.4% reflectance, and for a 10-bit image there were steps of approximately 0.1% reflectance.

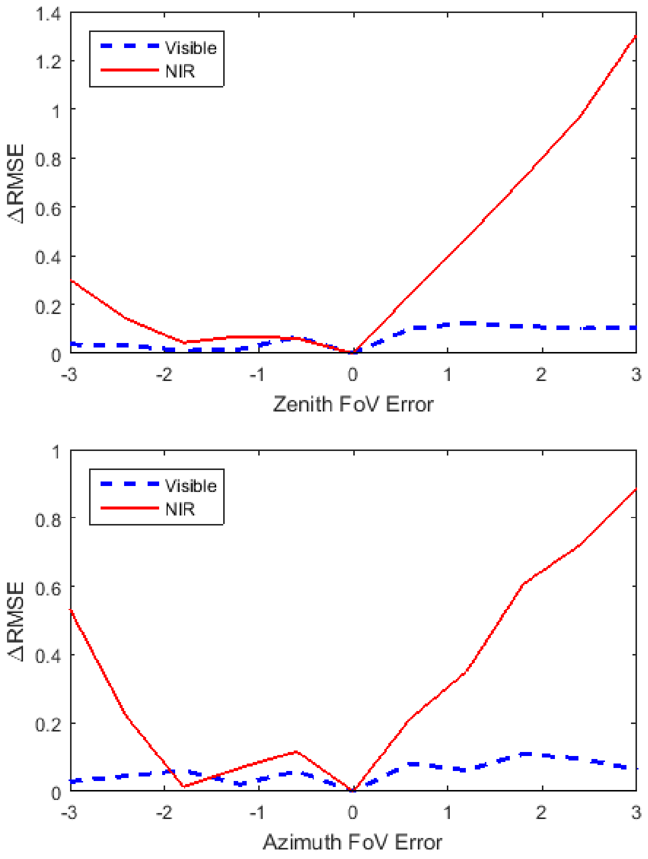

*Figure 9: Simulated results for the change in system error as a function of the misestimate of the field of view of the camera system in the azimuth and zenith directions (in degrees).*

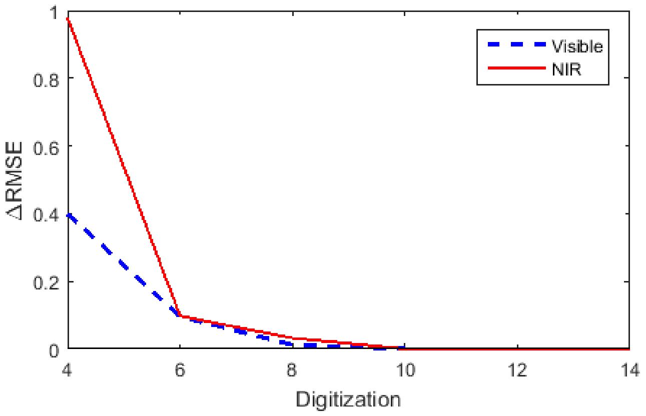

*Figure 10: Simulated results for the change in system error as a function of the digitization of the image.*

In running this simulation, I found that after 10 bits, this was not a significant source of error (Figure 10). At 8 bits, it was a minor source of error. Any digitization less than that would produce a large amount of error. Since 8 bits is an industry minimum, even for consumer web cameras, this specification should not drive the design or selection of the camera.

### 3.3.9 Error Due to Spot Size

When using an imaging system, a point source will not image to an exact point in the image plane. How much a point is allowed to spread out, while still providing us with good information is something that must be estimated for each system. As BRF is smooth and continuous, I expected that this would be a loose specification.

To estimate this as a source of error, I took a BRF generated by PROSAIL, taken over a hemisphere, and applied a mean value convolution to it. After applying the convolution, I then found the mean difference between the smoothed and unsmoothed data. By changing the size of this mean value convolution, and with an estimate of the pixel-to-angle ratio, I could estimate the effects of spot size on the BRF.

I found spot size was not a constraint on this system. Simulations produced the surprising result that even spots comparable in size to the camera sensor did not have a detrimental effect on the BRF. While this is consistent with the observation above that we expect that smoothing a smooth function to have minimal effects, this a larger effect than expected. Consequently, it was approached with some caution. While spot size would not be a driver of the system design, it was something that merited more research on its effects on the complete system.

### 3.3.10 Error Due to Filter Choices

Error due to the range of filters of the transmission of light was likely in this experiment. When interference filters are used at an angle, they will be transparent at a range of wavelengths, λ, determined by the equation:

$$\lambda(\alpha) = \lambda_0 \sqrt{1 - \frac{\sin^2(\alpha)}{n^2}} \qquad \text{Eq (9)}$$

Where α is the angle of incidence, n is the index of refraction of the medium, $\lambda_o$ is the wavelength of transmission for light at a normal angle of incidence. Interference filters are designed to only allow through light at a specified wavelength. When the angle of incidence to the filter is increased, the effective spacing of the reflective surfaces is increased, and the range of light transmitted shifts (Figure 11).

Using this formula, and an estimate of the refractive index of the glass as n = 1.5, for a change in view angle of 30°, there is an approximately 5% change in the wavelength transmitted by the filter. The blue band, for instance, this would mean a change in the center mean of transmission of 24 nm, for a band that is 60 nm wide. It would change the width by of the band by 3 nm, as the short and long wavelengths of transmission change different amounts.

The shift in the spectral transmission of light with view angle is a problem when used with a large field of view system. One way to compensate for this effect is to design the system so that the light passes through the filter when it is at a near 90-degree angle of incidence. In this case, that was not possible since this camera system was designed to be used with off the shelf parts. Performing lens design for a wide field of view system with off the shelf lenses with room for a filter wheel in the center fell outside the scope of this project. In addition, this would be impossible with the web camera system. It was desirable to find a solution that would enable the filters to be in front of the lenses.

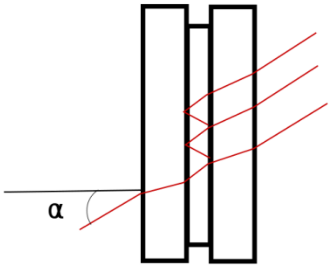

*Figure 11: As the angle of incidence, α, increases, the effective spacing of an interference filter increases.*

In order for the filters in front of the lenses provide a consistent range of color transmission, it was necessary to work with colored glass filters. This meant that while the quantity of transparency would change at off angles, again due to a change in thickness, there would be no change in the spectral range of the light transmitted. The disadvantage of working with commercial off the shelf colored glass filters is that they have a limited set of frequency transmissions available. As can be seen in Figure 12, many of the cut-on and cut-off frequencies can be very similar. These cut-on and cut-off frequencies are not sharp, so a filter that is advertised as a 780 nm longpass filter has more than 10% transmission at 750 nm.

Both these problems meant that there would be some inherent level of difference between the filters chosen for the cameras, and the Landsat 7 ETM+ bands themselves. I

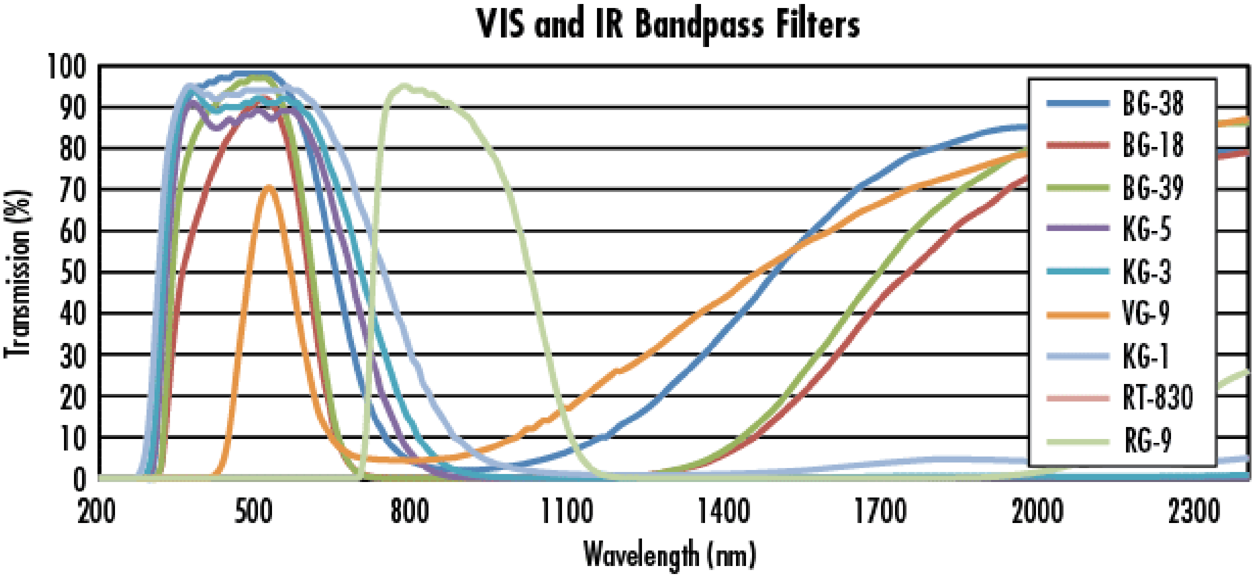

*Figure 12: Example of the transmission of several filters available from Edmund Optics. Figure taken from their online catalog* ("Colored Glass Bandpass Filters," n.d.)

programmed my PROSAIL simulation to estimate this effect by producing reflectances over a specified spectral range. I kept this as a linear sum over the range of spectral reflectance values, rather than accounting for the slope of the filter's transmission over the spectral range. The simulation would then use reflectances taken at one spectral range for the LUTs, and another set for the simulated readings taken. I experimented with both the filter transmission range being wider or narrower than desired, and the center mean of the filter transmission range being offset from the desired center.

I found with this analysis that error for the filter range depended most strongly on avoiding certain spectral landmarks. In the design of the camera system, it was necessary to avoid having the NIR filter avoid the red edge in the red (Figure 13), or its readings would be consistently low. For similar reasons, the red band needed to

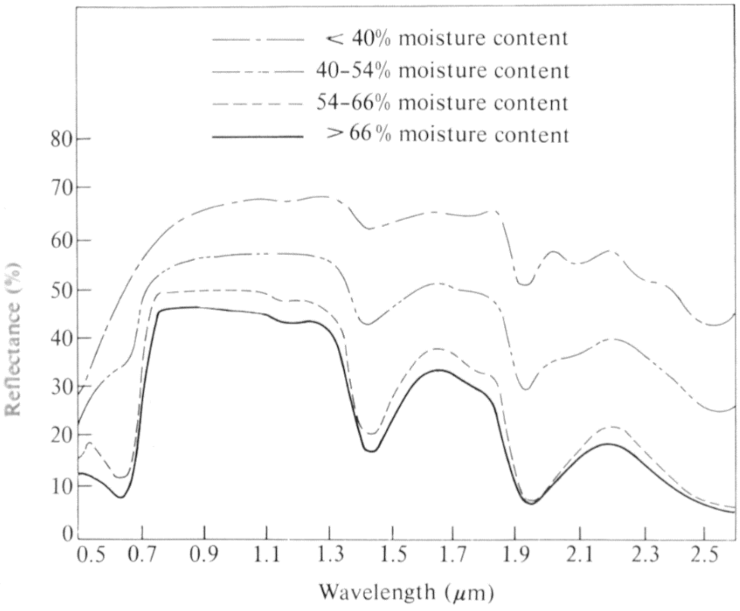

*Figure 13: Examples of vegetation reflectance, over several levels of moisture content.* (Davis et al., 1978)

avoid crossing the red edge into the NIR. There were similar, but small effects from the blue band coming too close to the hump of increased reflectance in the green.

### 3.3.11 Error Due to Fall-Off Estimate

As the angle increases between the object and image, there is a fall off in brightness, due to the change in the projected areas of the source and detector. The combined effect gives rise to the $\cos^4$ law, written:

$$\frac{E_\alpha}{E_0} = \cos^4 \alpha \qquad \text{Eq (10)}$$

Where α is the angle of incident light, $E_o$ would be irradiance for an image parallel to the object plane, and $E_\alpha$ is the irradiance on the tilted plane. Because of differences in lens design, there will be some variation from this relationship. An important factor for this experiment was to separate the change in pixel DN due to the lens from the change in DN due to of the surface BRF. As camera system is designed to have a wide field of view, there will be considerable fall off.

To simulate this effect, my simulation took readings of the ground using a $\cos^4$ falloff, and took the readings for the simulated input that were a percent off the $\cos^4$ falloff. As can be seen in Figure 14, if the falloff is not measured to within 1%, it will rapidly dominate the error budget.

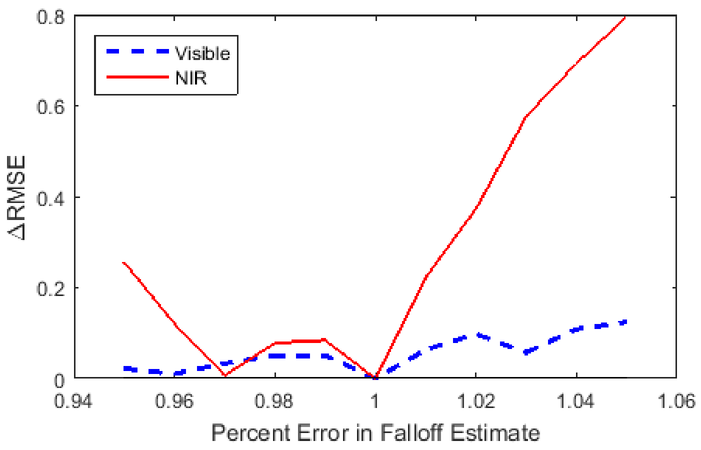

*Figure 14: Simulated results for the change in system error as a function of the misestimate for falloff.*

### 3.3.12 Error Due to Linearity

The digital number produced by the camera is not guaranteed to linearly change with the irradiance falling on it. Some estimate of the linearity must be made in order to confirm this relation. This simulation worked by incorrectly scaling the data, and finding how this affected the PROSAIL inverse (Figure 15). Error due to thermal response was treated as an extension of the linearity calibration. This was a dominant source of error, and like the lens falloff, one that needed to be measured and calibrated for.

### 3.3.13 Error Due to Spatial Sampling

For most of this simulation, it was assumed that the PROSAIL surface being sampled for the BRF recovery uniformly had the same PROSAIL input parameters across it. A real grass surface though could be expected to have some variation in its health. One reason for using the camera to measure BRF over a large area would be to account for variations such as sections of grass that might be distressed due to lack of water, or trampling. However, while the camera helps account for this variation in surface BRF, it is also necessary to understand the limits of this process. This part of the simulation generated random input values for PROSAIL, within limits outlined in Table 2, and arranged them as a checkerboard, to act as a worst case assumption for a varying surface. As I did not know the rate of change that could be expected for a real grass surface, I experimented with checkboard grass surfaces with different ranges of variation, and different rates of change across the surface. The error estimate in used for Table 3 was derived from a median value for these different combinations.

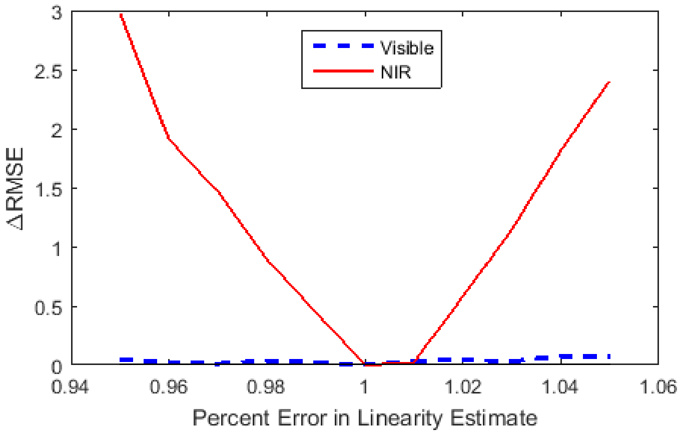

*Figure 15: Simulated results for the change in system error as a function of the misestimate of the linearity of the camera.*

### 3.3.14 Error Budget and Observations

The values for error derived in the previous sections were used to produced the following error budget (Table 3).

*Table 3: Error budget for the camera*

| | | **Solar φ = 180** | **Solar φ = 230** |
|---|---|---|---|
| **Error Source** | **Value Allowed** | **ΔRMSE** | |
| Computation Error | - | 0.49% | 0.27% |
| Read Noise | 0.06% | 1.00% | 1.13% |
| Digitization | 10 bits or more | 0.03% | 0.00% |
| NIR Filter | 750-950 | 0.02% | 0.10% |
| NIR Filter Uncertainty | ± 5 nm | 0.08% | 0.06% |
| Dark Current | - | 0.00% | 0.00% |
| Spot Size | - | 0.00% | 0.00% |
| Linearity Estimate | ± 2% | 0.65% | 0.80% |
| Lens Fall-off Estimate | ± 2% | 0.23% | 0.28% |
| Zenith FFOV Error | ± 1.5° | 0.51% | 0.27% |
| Azimuth FOV Error | ± 1.5° | 0.46% | 0.35% |
| Sun Angle Estimate | 3° | 0.11% | 0.25% |
| Zenith Misalignment | ± 5° | 0.41% | 0.76% |
| Azimuth Misalignment | ± 5° | 0.03% | 0.20% |
| Field Variation | - | 0.46% | 1.21% |
| DN to Reflectance | ± 2% | 0.65% | 0.80% |
| | | | |
| | **Total Error** | 5.13% | 6.46% |
| | **RSS Error** | 1.74% | 2.25% |

While the read noise for the camera is specified to be quite low and is a driver of the design of the system, this can be compensated for by increasing the number of pixels sampled. The filters need to be selected so as to avoid the red edge in the NIR but are otherwise loosely specified. The digitalization is not very tight, and all other specifications for the camera are nominally free. The important drivers of the camera design will be in measuring the set up of the camera, as with zenith and azimuth misalignment, and in the calibration of the camera. This knowledge helped with the camera selection, by eliminating the need for a high-end system, and demonstrating feasibility for the use of the web camera. It ensured that proper time was put into planning the calibration and the necessary steps for the field work.

## 3.4 Camera Design

### 3.4.1 Overview

With the error parameters estimated, it was now necessary to select cameras and components that met the specifications. Many of the specifications were fairly loose, or based on the calibration. This provided a broad range of camera options to select from. Other parts of the camera like the color filters were part of the system to be designed, but not built into the camera or lens. It was possible to let these be independent of other camera choices. This is fortunate for the future of camera systems designed to measure BRF and near-nadir reflectance, as it means that the cameras selected need not be expensive ones; This also made it necessary to find secondary reasons that the camera was suitable for this experiment. These sections provide guidance into how selections may be made.

### 3.4.2 Scientific Camera Selection

To provide more control over the spectral sensitivity of the camera, I selected a panchromatic camera. A camera with a c-mount was preferred, as this provided compatibility with a wide range of possible lenses, particularly inexpensive ones designed for use with security cameras (see section 3.4.3 for more details on why this was desirable). A low number of pixels was also desirable. Both the LUTs generated for the inverse and the images of the turf grass as a calibration target would take up hard drive space. Since it was impractical to run the inversion process using even a few thousand sampled pixels, a smaller array was desirable. A smaller pixel array also made it possible to take multiple redundant images in the same time as a larger array, to decrease the read noise. It was thus undesirable to pay for a more expensive camera with a higher resolution. A final consideration was compatibility. A Point Grey Blackfly was selected as the scientific camera for this experiment, as it met these specifications and the ones from the error budget, and because I was familiar with integrating Point Grey cameras with Matlab.

### 3.4.3 Lens Selection

Lens blur was not a strong source of error, so there was no requirement placed on the quality of the lens for the scientific camera system. A standard consumer grade security camera c-mount lens was selected. Security camera lenses are designed to work in the visible during the day, and the near infrared at night, requiring them to provide adequate lens properties in both spectral regions. By selecting a consumer grade lens, it was possible to purchase several different options, as the most expensive one purchased was $10.50. Lenses for security cameras tend to be poorly specified, providing little information about parameters like distortion. In addition, there are mixed conventions for even specifying the focal length of the lens. In some instances, it is the actual focal length of the optical system. In others the focal length that would produce the equivalent field of view for an older and larger analog sensor. For this small scale experiment, it was necessary to get close to the turfgrass, so the near point of the lens was important but also unspecified by manufacturers. While blur was not an issue, having a different amount of blur depending on the set-up was undesirable, as this would add unaccounted for variation between experiments.

After testing several lenses, one was selected on the basis of the location of the entrance pupil. While all the lenses had a similar field of view, this field of view begins at the entrance pupil of the system. If the entrance pupil was located too far back in the lens system, then the rings to hold the filters would cause vignetting in the image. The lens selected showed some distortion, had the correct field of view, a close near point, and the ability to adjust the focus.

### 3.4.4 Web Camera Selection

The web camera for this project was selected on three primary criteria. The first was whether the camera had a similar field of view to the scientific camera. This would enable the data taken by the two cameras to be more easily compared. The second criterion was compatibility. Many security cameras produce an analog signal which needs interpretation before being read by a digital system. This presented a problem of finding hardware and software that would enable Matlab to operate the camera, and collect the signals produced. Since most modern cameras use CCD or CMOS sensors to detect the light. This created a situation where there would be digital to analog processing taking place in the camera before it had to be processed from analog to digital again at the computer. The noise effects of this unnecessary double conversion were unknown. For both these reasons, a camera with a digital output was desirable. The third and most important criterion was whether it was possible to control automatic features on the camera. Automatic adjustments to brightness, gain and contrast of the image would make it difficult or impossible to compare images taken using different lens filters, as the settings might change each time between them.

I researched web cameras for which it was possible to manipulate their input parameters and found several that tied for the largest number of features it was possible to control. I selected a Creative Live! Cam Sync HD 720P Webcam. This was one of the least expensive cameras as well, which enabled me to put some budget aside in case I needed to try another camera later. This also proved useful, since it enabled me to iterate through the modification process, ordering a new camera after I had discovered ways of permanently breaking the camera in the modification process.

### 3.4.5 Web Camera Modification

The modification of the web camera was necessary in order to make it work in the near infrared. While CCD detectors area sensitive in this region, NIR light is often filtered out to make the sensor output more similar to what is visible to the human eye. This would not have been an issue if a security camera had been chosen, since they are designed to work in the NIR; however, since I could not find one that was digital, affordable, and guaranteed that I would be able to adjust its settings such as contrast and gain, a web camera for

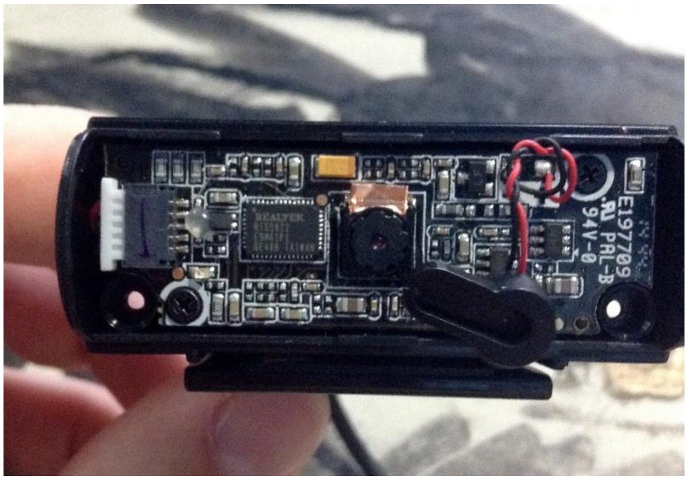

*Figure 16: Circuits inside the web camera, with the lens system glued to the board (center)*

*Figure 17: Examples of images from the web camera (A) with its original filters, (B) with the NIR filter removed and (C) with a 600 nm cut off filter. Vignetting in (C) is due to the lens holder used for this demonstration.*

video chat was substituted. It was necessary to remove the NIR filter from the camera.

The first step to removing the NIR filter was to open the camera (Figure 16). Inside, it appeared that it would be possible to unscrew the lens from the camera, but this did not turn out to be the case. This screw provided some focus control. The lens system was attached to the CCD and circuit board using glue, and not any threading mechanism. This meant removing the lens required cutting and breaking the optics from the board. After doing this, I found the NIR blocking window behind the lens, glued to the optics. This required breaking another component and required some practice to remove in a way that did not scratch the other optics.

After removing the NIR filter, I glued the optics back onto the circuit board. I aligned this by hand, while monitoring the focus and vignetting through the output of the camera. As can be seen in Figure 32, there was some misalignment in this process, causing the lens falloff to be offset, and dark in one corner. Since blur was not a concern (section 3.3.9) and lens falloff was measured and accounted for (section 3.6.7), this was not considered a significant source of error for the process. Figure 17 shows the change in the image resulting from this process, combined with the filters selected in section 3.4.6. Some minor additional modifications were necessary in order to attach the web camera to the rails. This involved drilling a hole in the base, so that it

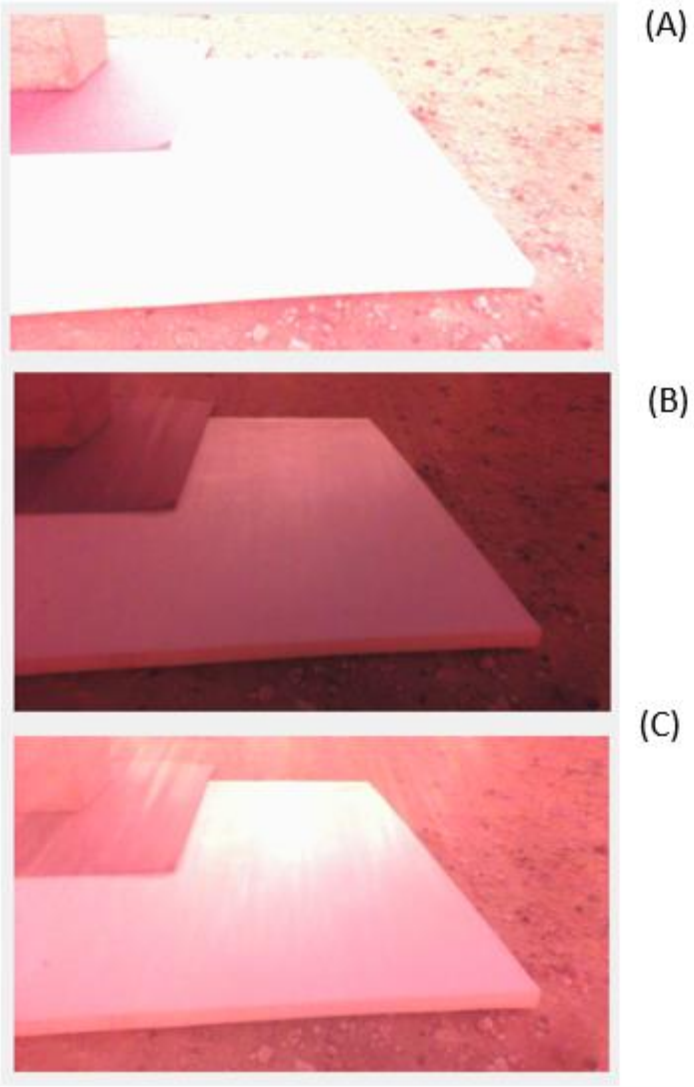

*Figure 18: The web camera would start at a default gain, seen in image (a). When set to automatic mode, it would change to gain setting (b). Resetting it to manual mode would set it to gain setting (c), between those seen in (a) and (b). Restarting the web camera would consistently return it to the settings in (a).*

could be attached to a 1/2 inch diameter pole with a screw, and cropping off plastic parts that interfered with the mounting.

Late in the process of modification, I discovered an additional gain setting that is not accessible directly by the software operating the camera, but instead was adjusted when the camera was set to automatic. Setting the camera to automatic would not change any of the values for the observable settings of the camera once they had been given fixed values, but would for the rest of any session operating the camera adjust a hidden dial for the gain of the system. Repeated experiments over strong changes in brightness showed that if the camera was left in manual mode, this hidden gain dial would stay steady. Curiously, turning the camera to automatic mode, and then back to manual would leave the gain at some middle value between that provided by the automatic setting and the default setting in manual mode (Figure 18). As it was desirable to have a lower gain setting (see the section 3.4.6 for details), I took to resetting the web camera between automatic and manual before each set of readings taken from the turfgrass. While this would have been problematic with an absolutely calibrated system, using a near Lambertian target for the DN to reflectance conversion enabled me to take advantage of this feature of the web camera.

### 3.4.6 Colored Glass Filter Selection

For the scientific camera, the goal was to match the relative spectal response used by the Landsat 7 ETM+ satellite. To this end, it was necessary to use two filters, one in front of the other. One acted as the cut-on filter, while the other would act as the cut-off filter. For the web camera, with which I did not have knowledge of the Bayer filter built into the CCD, this was not an approximation that I could make. Instead, in that case, it was necessary to provide filters that would separate the NIR readings from the color readings. The light from the outdoor scene also flooded the sensor for the web camera, even at its lowest shutter setting, likely because it was designed for indoor use. To compensate for this, neutral density filters were also necessary.

As mentioned in the section on filter choice error (3.3.10), the primary driver for the selection of filters was to have the blue avoid the spectral 'hump' present in the green in vegetation, and for the red and NIR not to cross the red edge in the NIR region. This meant the blue band needed to cut off by 525 nm, and the red and NIR to cut off and on respectively before and after 750 nm.

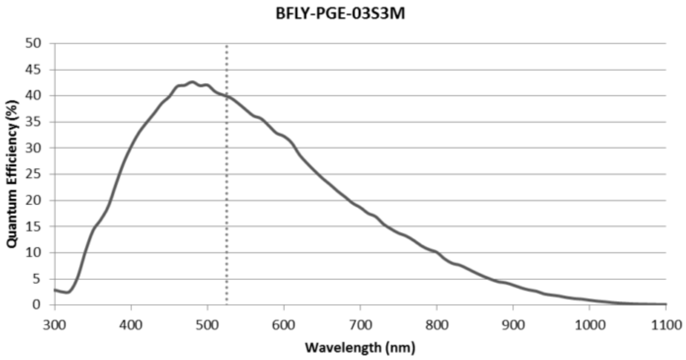

*Figure 19: Quantum efficiency for the scientific camera.*

There are a limited number of readily available blue glass filters, and it was difficult to find a combination that both provided transmission at the required values and did not provide transmission in the NIR. The quantity of light in the NIR would be up to 10 times more than that in the blue, so transmission in the NIR would be significantly detrimental to the accuracy of the measured blue reflectance. It was not possible to compensate for this by adding a third filter to the system, as this would have begun to cause vignetting in the system due to the wide field of view. An additional concern when selecting filters was that it was possible to create combinations that cut on and off at the desired frequencies, but let through very little light. As the blue band is already in a part of the spectrum that both reflects very little light (Figure 13) and does not produce much response in the sensor (Figure 19), there was a risk of substantially decreasing the signal to noise for this band.

Thorlabs provided exact specifications for its filters on its website. Using the numbers they provided, I tested combinations for their combined transmissions. Finding pairs for the other color bands, green, red and NIR, was simpler. While it was necessary to avoid the red edge in the NIR, there were filters readily available to do this.

*Table 4: Colored glass filters used by the camera system.*

| **Camera 1** | Cut-On Filter | Cut-Off Filter |
|---|---|---|
| Blue Band | FGL-435 | FBG-25 |
| Green Band | FGL-530 | FBG-39 |
| Red Band | FGL-610 | FBG-37 |
| NIR Band | FGL-780 | None |
| **Camera 2** | | |
| Color Bands | NB-10B | FGB-37 |
| NIR Band | FLG-780 | NB-20B |

For the NIR, only a cut-on filter was used, as the response of the scientific camera goes to zero as it approaches 900 nm (Figure 19).

As stated before, with the web camera, it was only possible to sort readings into those taken in the NIR spectrum, and those in the visible spectrum, with no simple way to know the extent of the Bayer filter. It was necessary to filter out the majority of the light in this case. As we can see in Figure 20, less than 0.1% of the light is transmitted by the filters. Given the amount of noise in the resulting image, it is likely that the web camera sensor has considerable gain already built into it.

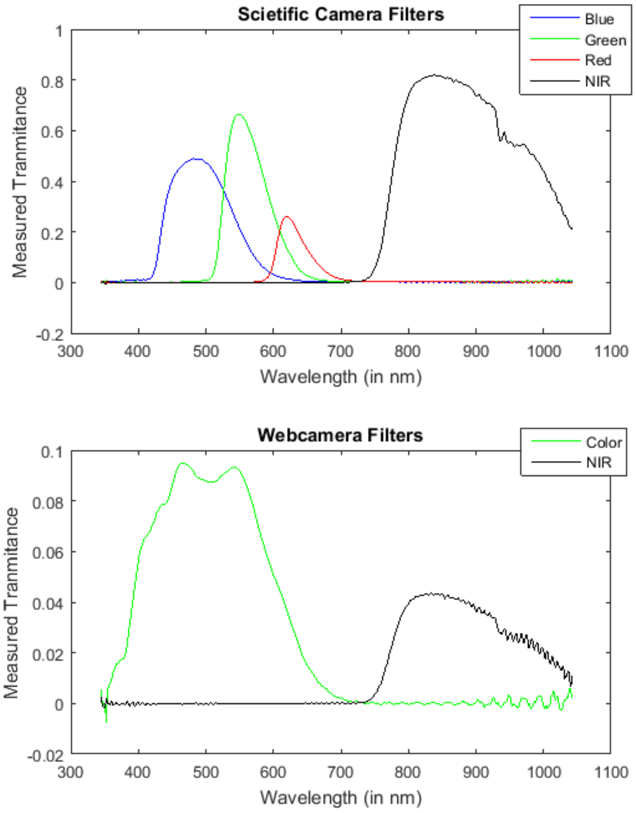

*Figure 20: Measured transmission for the filters used by the scientific and web camera.*

### 3.4.7 ASD Mounting and Distances

A Teflon target was used to convert the ASD data from digital numbers to reflectance, thus the area the ASD could view was limited by the size of the Teflon target. To ensure the area viewed by the ASD and Teflon target were well matched, I calculated the area the ASD would view on the ground, and confirmed this value with an experiment.

An 8° field of view optic was attached to the ASD. This enabled the ASD to measure a large area while staying relatively close to the ground. I calculated that it would view an area 25 centimeters in diameter when it was at a height of 91 cm. The ASD optic made use of a pistol grip that was attached to a camera tripod using a 30 centimeter long 1/4 inch by 20 threaded pole. The pole enabled the ASD optic to be far enough from the base of the tripod that the feet of the tripod were not visible to the ASD or the camera while data was being gathered.

I tested the calculated field of view by aiming the ASD on the tripod at a large sheet of paper in a dark setting. A commercial 1 mW 532 nm laser mounted on another tripod was aimed at the paper. When inside the field of view of the ASD, the reflected laser light generated a distinctive response on the ASD's readout. By moving the laser across the paper systematically, and marking the places where it stopped being visible to the ASD, I was able to map out the area seen by the ASD. I repeated this experiment for the ASD at 0°, 15° and 30°, and confirmed in all cases is stayed within a 1 foot square area, consistent with the size of the Teflon target.

### 3.4.8 Camera Mounting and Distances

The camera system’s field of view needed to overlap with the area viewed by the ASD as much as possible. This ensured that any disagreement between the camera system's estimate of near-nadir reflectance and the ASD's measurement was due to a failure of the camera, and not differences in the areas viewed by the cameras and ASD. My original intent was to have the camera and the ASD cover the exact same area. A large high-quality target proved unavailable, and would have required placing the ASD a considerable distance off the ground. Having complete overlap for the smaller target placed the camera less than a foot from the ground. This was undesirable as it raised concerns of adjacency effects and self-shadowing, as well as requiring unusual mounting to provide a tripod of sufficient width to support the camera, but with negligible height.

Simulations showed error due to the difference in the area covered by the camera and the area covered ASD varied with the amount of variation of the surface, with more uniform surfaces producing less error. The camera covering roughly 4 times the area of the ASD was found to balance the error and the camera distance.

The cameras were mounted side by side. This limited the number of angles that had to be measured for each setup, and made the data taken by the cameras more comparable, by ensuring that the two cameras were being tested on the same surface at the same angle in the same weather conditions. To maximize this crossover, it was desirable to keep the cameras as close together as possible. An arrangement was found where the distance was minimized while avoiding overlap in the filter

*Figure 21: Mounted camera box, with fan and cameras inside.*

wheels and the bodies of the cameras. This placed the center of the web camera lens 2.5 cm above and 5 cm to the left of the optical axis of the scientific camera.

The cameras were mounted to two connected rails. One rail was then mounted to a tripod. The tripod was secured to a 20-pound weight for stability. To limit the amount of stray light in the system, a box was constructed that could block the light from coming in from 5 sides (Figure 21), and was mounted on the rails with the cameras. The exterior surfaces away from the camera and ASD and target were kept white to help keep the system cool, while other surfaces were painted matte black with a commercial grade paint. The box was vented, with a fan mounted inside to help the temperature of the cameras stay below the point where they no longer operated.

## 3.5 Lambertian Target

The disadvantage of using a reflective target to provide calibration between the digital number and the reflectance is that it requires knowledge of the BRF of the surface. This BRF was measured by the University of Arizona Remote Sensing group in their blacklab, using a well known silicon filter radiometer and comparing a Spectralon panel with NIST calibration. This gave measurements of the Teflon's at nadir reflectance for angles of incidence between 10° and 85° at 5° increments, and at 402 nm, 455 nm, 503 nm, 554 nm, 651 nm, 699 nm, 801 nm, 846 nm, and 951 nm. I fit a second degree sine function to this data (Figure 22), which in all cases provided an $R^2$ value of over 0.99. The Teflon, as can be seen here, is within 90% of Lambertian behavior from 10° to 65°, the maximum angle

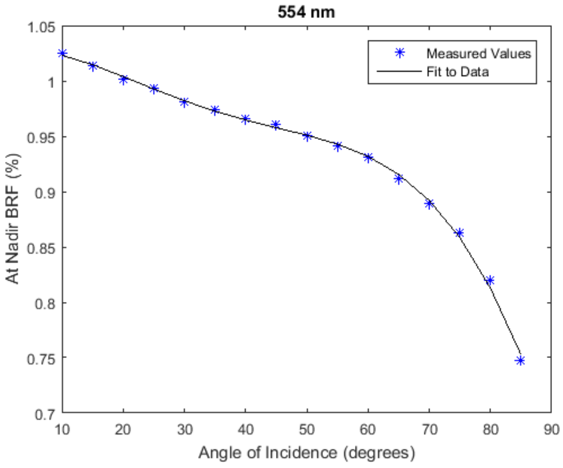

*Figure 22: Measured BRF and a fit of the Teflon target used to convert from digital number to reflectance.*

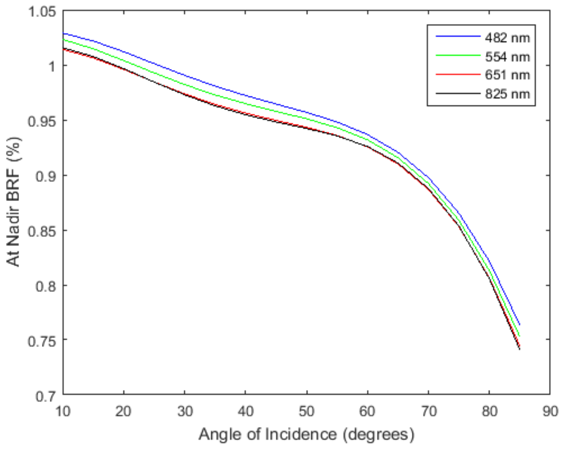

*Figure 23: Comparison of the BRF fit for the four spectral bands used.*

that the camera viewed it. As these measurements were for the reflectance measured at nadir, for an off angle incident ray, where both the source of light and the view angle were off-nadir, it was necessary to approximate the BRF using these data. This was done by assuming that all BRF reflectance could be scaled by the factors in Figure 23. In section 4.2.2 I discuss evidence that this is not true.

## 3.6 System Calibration

### 3.6.1 Introduction

To be useful scientifically, the readout from a detector must be related to the parameter that is being measured. Without this step, readings are numbers without scale or context, providing no information. Within this research, calibration was necessary to change a grid of digital numbers produced by a camera into an estimation of BRF. To do that, each pixel needed to be related first to a view angle, and then to a system of BRF angles related to the ground and sun. The digital numbers produced for these grids had to be investigated for artifacts that might distort the data. Linearity had to be checked to ensure that digital numbers could be accurately mapped to estimates of detected radiance. Differences in the sensitivity of each pixel of the detector and stray light in the system had to be accounted for. Since the system was uncooled, the change in detector response due to temperature fluctuations was measured. Because a Teflon square was used for the cross-calibration of the cameras and ASD, the BRF for the Teflon had to be measured.

This section is intended to provide both an accounting for how I performed this calibration and guidelines in how they can be performed. In order for researchers of remotely sensed data to make use of camera systems for BRF and near nadir reflectance measurement, it may be necessary to find ways to perform the calibration without advanced equipment. Often, the people interested in gathering and using remotely sensed data do not have the engineering background or resources available to perform the sort of optical system calibration that would be more standard for a camera system like this. As such, it is necessary to design a calibration method that would be available for them and rigorously prove that they work. We can see examples of why this would need to be the case in comparing how professional Lambertian paint is manufactured and applied versus how people who actually have to work in the field do it (Knighton & Bugbee, 2005).

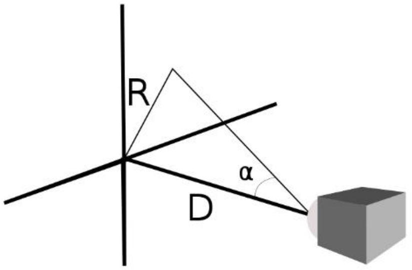

*Figure 24: It is possible to find the view angle α by finding the trigonometric relation between the distance along the optical axis D to the object, and the radial distance R perpendicular to the optical axis, along the object plane.*

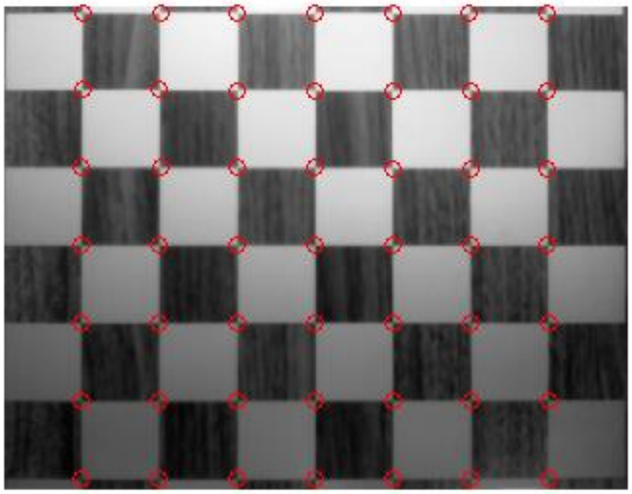

*Figure 25: An example of an image of the checkerboard taken with the web camera. Circles represent the corner points found using Matlab's detectCheckerboardPoints()*

It was not possible for me to do design or find simple calibration methods in all instances, but I hope that the work I have done here can provide a start to such a line of research.

### 3.6.2 Pixel to Degree Conversion

BRF is a measure of both reflectance values and their angular distribution. To use a camera as a means of measuring BRF, it is fundamentally necessary to understand the relationship between the pixels and the angles they are viewing. The relationship between pixel number and view angle can be established by comparing the pixel location of an object with its physical location. The physical location is defined by both the distance from the camera to the object along the optical axis, and the distance of the object from the optical axis (Figure 24). To establish a rigorous understanding of the view angle, we need to map this relationship for many positions and pixel numbers. To provide a large number of points of known radial distance, I used a checkerboard for this calibration. While there exist a number of targets specifically designed for scientific calibration, these tend to be designed for a narrower field of view systems. By using a larger target, I was able to keep the target in focus while making larger changes in distance.

The checkerboard provided a grid of 49 points of known distance. The pixel coordinates of the checkerboard points in the image were found using Matlab's detectCheckerboardPoints() function (Figure 25). This provided coordinates for the points that were accurate and repeatable.

Matlab's detectCheckerboardPoints() function would sometimes fail to find the checkerboard points in an image on the first run, but could be forced to run over and over till it did find them, if it was possible to. In some cases, a point would not be found by the 100th run of detectCheckerboardPoints(). That point was dropped from the analysis of that image. Each checkerboard point was manually assigned a number to track it across all the images.

These checkerboard squares were measured using a digital caliper and found to have a size of 39.8mm. As the camera was moved towards the checkerboard, grid points were lost when they moved off the image, or when Matlab could no longer detect them. Images were taken every 1cm, to provide a large number of images, while keeping the uncertainty of the camera location small relative to the size of the step. For the scientific camera, it was possible to take 25 images from distances of 44mm to 20mm before detectCheckerboardPoints() was not longer able to find any of the checkerboard points. The web camera had 23 images between 45mm and 23mm where checkerboard points could be found. This provided, across all the images, 769 points of known distance for the scientific camera, and 744 for the web camera.

Each camera's field of view was tested separately, rather than in the side by side configuration used when taking data. This allowed the cameras to be centered with respect to the center of the checkerboard, and for confirmation that the checkerboard stayed in the center as the camera was moved forwards and backwards. The latter test confirmed that the camera was aligned with the rail and that estimates of the view angles and distance to the board were accurate. The checkerboard was lit by ambient diffuse light to avoid specular reflections confusing the checkerboard grid detection. Both cameras were tested at the resolution used for the BRF experiment.

The distance used in the field of view is measured from the principal plane of the imaging system, and not from the physical camera. Since all measurements along the optical axis must be done compared to a physical component of the camera, this distance D must be then modified to by a distance Δ to find the distance between the calibration object and the principle plane. Using this combined distance, and knowledge of the height of the object, h, we can find the view angle, α, using the trigonometric relation:

$$\tan(\theta) = \frac{h}{D + \Delta} \qquad \text{Eq (11)}$$

To find Δ, we can compare two images, making use of the assumption that for low amounts of distortion, we can find a constant C, relating the angular size of an object to its image size in pixels, such that:

$$C = \frac{Image\ Size(in\ pixels)}{Object\ Size(in\ degrees)} \qquad \text{Eq (12)}$$

Using images taken at different distances $D_1$ and $D_2$, we can find a value of Δ that allows for a constant ratio C, such that:

$$\frac{Image\ Size\ (D_1)}{Object\ Size(D_1)} = \frac{Image\ Size(D_2)}{Object\ Size(D_2)} \qquad \text{Eq (13)}$$

Which can be rearranged

$$\frac{Image\ Size\ (D_1)}{Image\ Size(D_2)} = \frac{Object\ Size(D_1)}{Object\ Size(D_2)} \qquad \text{Eq (14)}$$

The ratio of the two image sizes remains constant regardless of the value of Δ, leaving only the object ratio dependent on Δ.

$$\left(\frac{h}{D_1 + \Delta}\right) / \left(\frac{h}{D_2 + \Delta}\right) \qquad \text{Eq (15)}$$

The value for Δ can then be solved numerically, by testing values of Δ till one is found where the object size ratio matches the image size ratio (Figure 26: By varying the value for Δ, a ratio of the angular object sizes can be found that equals the ratio of the image locations in pixels.).

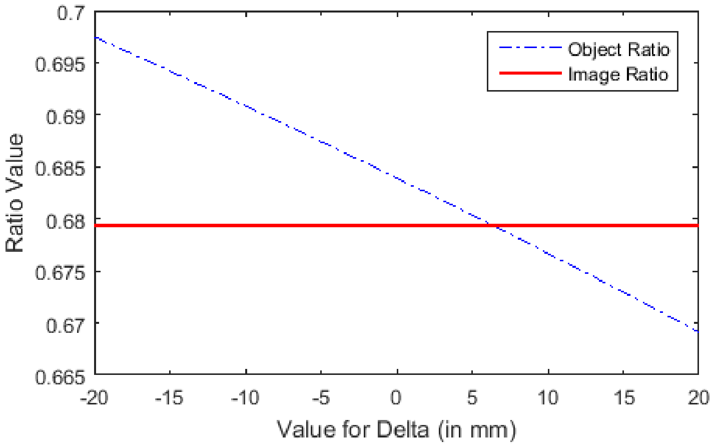

*Figure 26: By varying the value for Δ, a ratio of the angular object sizes can be found that equals the ratio of the image locations in pixels.*

The image size ratio between two images was found by taking the ratio of the average size of a side of a checkerboard square in pixels for each image. Only the average value of the center four checkerboard squares was taken, as these would be the squares with the least distortion. The linearity assumption built into Eq (12) breaks down with distortion as the pixel size of an object becomes dependent on its location in the image, and not its physical size.

The object ratio was estimated for many values of Δ, and then the delta that produced a minimum difference between the image and object ratios was found. Estimates for delta were found using all image pairs 6cm or further apart. Smaller distances between the images were ignored. They provided values of Δ that could be twice the value of those found at further distances. The average value of the estimated deltas was then calculated, giving a value of 4.4mm ± 1.6mm for the scientific camera, and -8.7mm ± 1.1mm for the web camera. This value was confirmed to provide a measured field of view within 1% of the field of view found using the fit between pixels and radial angle found below.

The checkerboard points were also used to find the distance R across the object plane. The squares had a measured spacing of 39.8mm. Their position could be accurately estimated using knowledge of the slope of the board and the distance from the center of the board from the optical axis.

While the camera was aligned with the center of the board such that the center point stayed constant between images, some variation still existed due to misalignment and variations in setting up. This variation was on the order of ± 5 pixels for the scientific camera, and ± 3 pixels for the web camera. The pixel distance between the center of the board and the center of the field of view of the camera was then converted to a physical change in the location of the

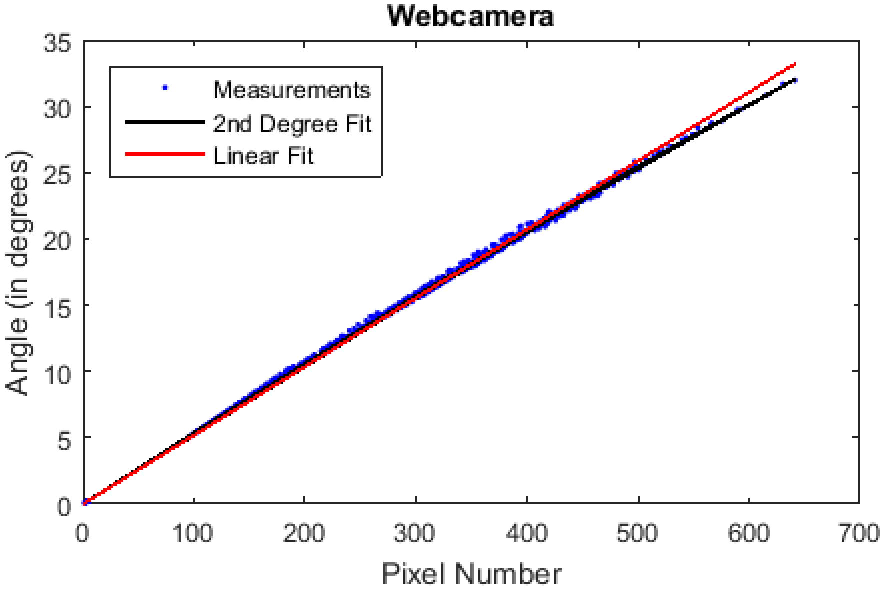

*Figure 27: An example of the difference between the fits for the web camera data, using a linear fit and a second degree polynomial. The fits are very similar up to around 400 pixels, at which point the linear fit begins to diverge from the data.*

checkerboard points using average pixels per square, and the known physical size of the squares. The slope of the board along the x-y plane was measured using the checkboard points. The slope value found using two checkerboard points on the same row varied with the distance of the checkerboard points from the center of the board. This was true both for points further along the row and points in different rows further from the center one. This is consistent with there being distortion in the image. The slope of the board was found using the center four squares and their nine corner points to avoid issues due to the distortion, but still have a reasonable sampling to eliminate error due to pixelation. Each image was assigned its own slope to account for variation in the set up between images. For the web camera, these slopes were very small, with a mean value of 0.02° ± 0.02°. For the scientific camera was there was a larger slope, but lower variation, with a mean angle of 0.97° ± 0.01°. Once the slope and center of the board were found, finding the physical radial distance of the checkerboard points could be found geometrically.

Having established values for R and D for all the corner points, these were then used to find a fit for the relationship between radial pixel distance and radial angle. To provide a physical solution, this fit was constrained to having a zero angle at zero pixels from the center. A second-degree polynomial was found to produce an estimate of the full field of view for the camera more consistent with the measured full field of view than a linear fit (Figure 27). This was the case for both the scientific and web camera, though more strongly for the web camera. Figure 28 and Table 5 show that while the second order term is quite small, the effects are quite noticeable.

*Table 5: The fitted equations for the scientific camera (Eq (16)), and the web camera (Eq (17)).*

$$\alpha = 3.9 * 10^{-6} * R^2 + 0.054 * R \qquad \text{Eq (16)}$$

$$\alpha = -6.9 * 10^{-6} * R^2 + 0.054 * R \qquad \text{Eq (17)}$$

The fit for the scientific camera has a root mean square error (RMSE) of 0.14° and a maximum deviation from the fit of 0.55°, while the web camera's fit has an RMSE 0.18° with a maximum deviation from the fit of 0.61°. This is well within the allowed error in the field of view estimate of 1.5° (see section 3.3.6). The linear fits have larger RMSE values of 0.16° and 0.28°, with deviations from the measured field of view of 0.55°and 1.24°. These are still within the specification, but is an unnecessary source of error in testing the system.

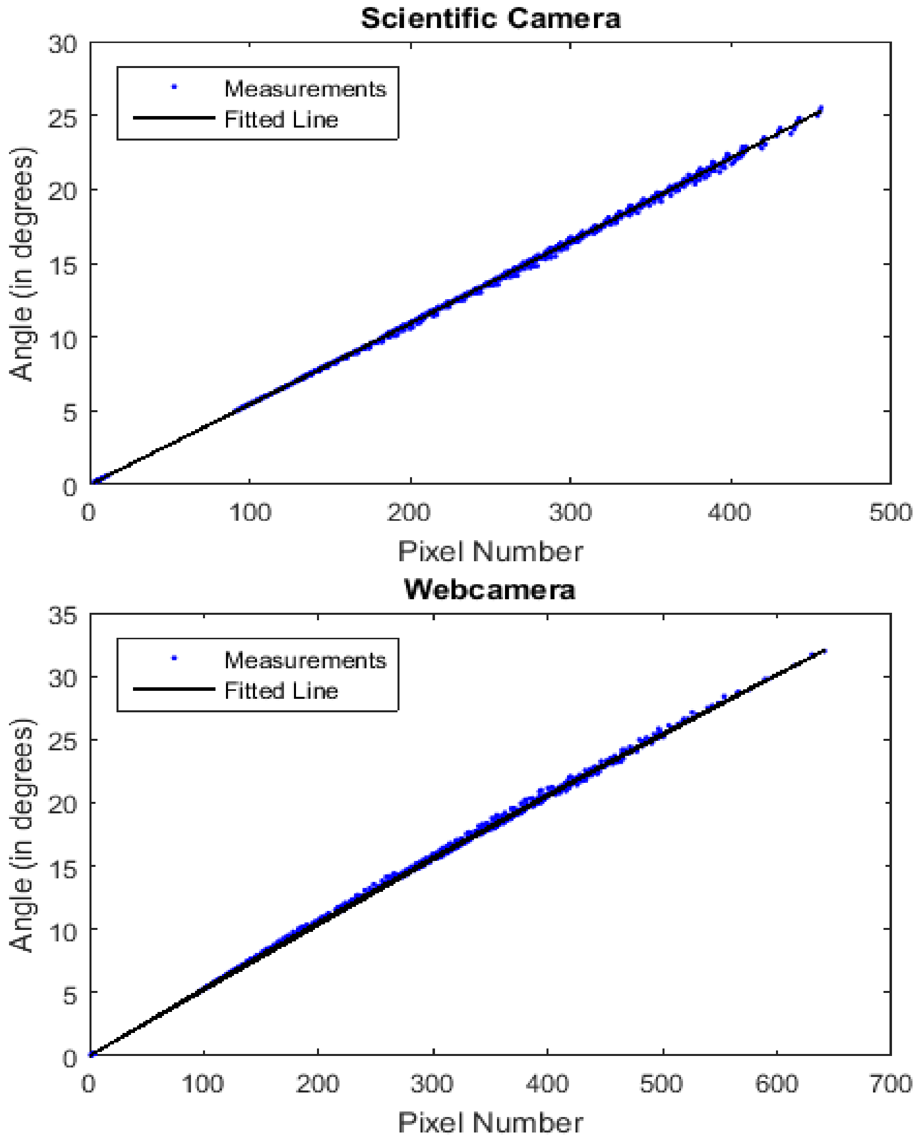

*Figure 28: Diagram of the second degree polynomial fits for both the scientific camera and the web camera. Both pixel number and angle are measured radially from the center of the image.*

### 3.6.3 Converting to Spherical Coordinates

A radial fit provided a large number of points with which to confirm the quality of the relationship between the pixel number and angle produced. There is nothing unusual about assuming radial symmetry to a lens system. BRF, however, is measured in spherical coordinates. It is necessary then to convert the relationship between pixels and angles further into a relationship between how the pixel's angle breaks down into azimuth and zenith components of the BRF (Figure 30).

θ and φ cannot be treated as completely independent of each other in this conversion. While this would be approximately true for a narrow field of view system, in a wide field of view of the system this is not the case. Figure 29 shows how from the camera's point of view, a change in y is equivalent to a change in θ, while a change in x is a change in φ. This is not always the case though, since x and y are Cartesian coordinates, and φ and θ are spherical coordinates. For a large value of y, a change in x will also be a change in θ.

To perform this conversion, I constructed an arbitrary set of Cartesian coordinates in image space. We start with the pixel distances from the center of the sensor, $m_x$ and $n_y$:

$$m_x = m - \frac{l_x + 1}{2} \qquad \text{Eq (18)}$$

$$n_y = n - \frac{l_y + 1}{2}$$

Where $m$ and $n$ and the pixel numbers measured from the top left corner, and $l_x$ and $l_y$

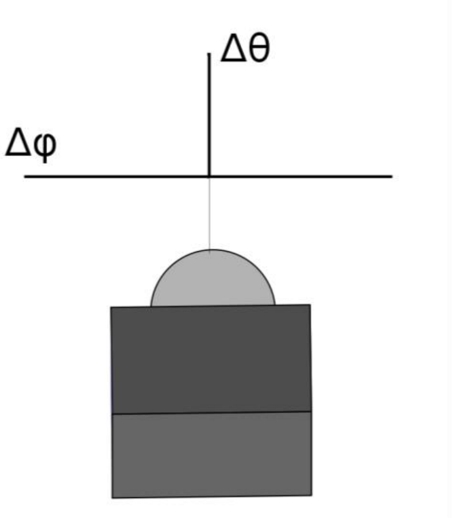

*Figure 29: Illustration of how θ and φ change with the location of a point in a camera's field of view.*

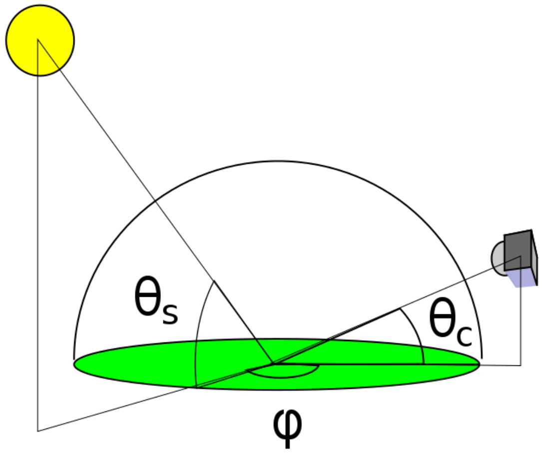

*Figure 30: Picture illustrating the sun zenith angle θs, the camera zenith angle θc, and the azimuth angle φ measured between the solar plane and the camera.*

are the length of the pixel array in x and y respectively. From this we can find the radial pixel distance:

$$r_{pix} = \sqrt{m_x^2 + n_y^2} \qquad \text{Eq (19)}$$

This provides a value to be plugged into the fit developed in section 3.6.2, providing an angle, α. This angle, in turn, provides an estimate of how far the pixel coordinates along the sensor must be from a theoretical thin lens system.

$$z = \frac{r_{pix}}{\tan^{-1} \alpha} \qquad \text{Eq (20)}$$

There is an opportunity at this point to account for the camera's roll angle, β. Roll refers here to rotation of the camera system itself around the optical axis, which changes both the values of θ and φ, and is described in more detail in section 3.3.6. It is possible to include the roll of the camera by rotating the pixel Cartesian coordinates $m_x$ and $n_y$ around the optical axis. This rotation is done using the following equations.

The rotated Cartesian coordinates generated were then converted into spherical coordinates, providing values for the change in θ and φ, and a radial distance which can be ignored.

$$\Delta\varphi = \tan^{-1}(\, n'_y / m'_x) \qquad \text{Eq (21)}$$

$$\Delta\theta = \tan^{-1}(\, z / \sqrt{{n'_y}^2 + {m'_x}^2}) \qquad \text{Eq (22)}$$

$$r = \sqrt{{n'_y}^2 + {m'_x}^2 + z^2} \qquad \text{Eq (23)}$$

While careful conversion to Δθ and Δφ and accounting for roll angle were small sources of error in my set up, it desirable to ensure that methods of estimating their effect are established so that future camera systems would have a method of accounting for them.

### 3.6.4 Changing View Angles into Ground and BRF Angles

Once a value of Δθ and Δφ are associated with each pixel of the camera, it is necessary to translate them into the reference frame for the BRF models. The first step for this is to find at which angles the camera is viewing the ground in a common coordinate system. In doing this, we will want to differentiate between the spherical coordinates, which are measured as an elevation angles and an azimuth from an axis, and BRF coordinates, which are measured as a zenith angles and an azimuth from the solar plane. One reason for having two coordinate systems is that this latter azimuth will change with time as the sun moves. To differentiate between these two coordinate systems, I will denote the spherical elevation and azimuth with Θ and Φ respectively, while BRF zenith and azimuth will be denoted θ and φ.

For the spherical coordinates, I picked a right-handed coordinate system with the x-axis lined up with North, and the y-axis with West. Rotation in Φ is measured in degrees West of North, while Θ is an elevation angle. To convert from camera view angles to spherical coordinates, we use the equations:

$$\Theta = 90° - (\theta_{cent} + \Delta\theta) \qquad \text{Eq (24)}$$

$$\Phi = \varphi_{cent} - \Delta\varphi \qquad \text{Eq (25)}$$

Where $\theta_{cent}$ and $\varphi_{cent}$ are the orientation of the camera, in zenith and azimuth angles measured in degrees. These coordinates can then be converted into BRF coordinates using the formulas:

$$\theta = 90° - \Theta \qquad \text{Eq (26)}$$

$$\varphi = -(\Phi - \varphi_{sun}) \qquad \text{Eq (27)}$$

### 3.6.5 Accounting for Ground Slope

In assessing sources of system error, one of the tightest constraints was the slope of the ground with respect to the camera. BRF is a measure of both reflectance values and their angular relations. Tilting the camera changes the relation between the θ and φ angles measured by the camera. Unlike an error measuring the orientation of the camera with respect to θ and φ, the slope of the camera will have a different effect on the angles measured for each pixel of the camera, with pixels further from the center having the most error. The fundamental relationships between θ and φ change.

The angle for the ground was estimated using measurements of the slope of the Teflon square before each set of readings for the camera was taken, in both the north/south direction, and in the east/west direction. This measurement was repeated before each reading was taken since in some cases, it was observed that there would be a difference of up to half a degree between measurements, likely due to some difference in how the grass settled under the Teflon plate. It has been assumed here that the average of these values for the Teflon slope provides a good approximation of the underlying ground and grass slope.

The camera's view angles for the ground from section 2.6.3 were then adjusted to compensate for the slope of the ground, as were estimates of the sun angle. This was done by rotating the coordinate frame of the existing spherical coordinates around x and y using the vector equations:

$$R_x = \begin{bmatrix} 1 & 0 & 0 \\ 0 & \cos(r_x) & -\sin(r_x) \\ 0 & \sin(r_x) & \cos(r_x) \end{bmatrix} \qquad \text{Eq (28)}$$

$$R_y = \begin{bmatrix} \cos(r_y) & 0 & \sin(r_y) \\ 0 & 1 & 0 \\ \sin(r_y) & 0 & \cos(r_y) \end{bmatrix} \qquad \text{Eq (29)}$$

$$R_n = R_x * R_y \qquad \text{Eq (30)}$$

Where $R_x$ is the rotation matrix for clockwise rotation around the axis pointing North, for a rotation of $r_x$ degrees. Similarly, $R_y$ is the rotation matrix for clockwise rotation around the axis pointing West, for a rotation of $r_y$ degrees. $R_n$ is the combination of these two rotation matrices. Care needs to be taken here, since the values measured for Teflon slope represent a rotation of the coordinate system, while the equations above are rotations of a vector in a coordinate system. These types of rotation are the same, but are in opposite directions, so that rotation of around the x-axis or $r_x$ is a rotation of the coordinate system around the x-axis of $-r_x$.

To apply these equations to spherical coordinates, each value of θ and φ used in the measurement of BRF was assigned a set of Cartesian coordinates on a unit sphere, with r = 1, using the conversion equations:

$$x = r * \cos(\Theta) * \cos(\Phi) \qquad \text{Eq (31)}$$

$$y = r * \cos(\Theta) * \sin(\Phi) \qquad \text{Eq (32)}$$

$$z = r * \sin(\Phi) \qquad \text{Eq (33)}$$

These Cartesian coordinates could then be rotated around the x- and y-axes, where x represented north, and y west, using the rotation matrix from eq #

$$\begin{bmatrix} x' \\ y' \\ z' \end{bmatrix} = R_n * \begin{bmatrix} x \\ y \\ z \end{bmatrix} \qquad \text{Eq (34)}$$

After the Cartesian coordinates are rotated properly, they can be converted back into spherical coordinates using the equations:

$$\Phi = \tan^{-1}(\, y'/x') \qquad \text{Eq (35)}$$

$$\Theta = \tan^{-1}(\, z'/\sqrt{y'^2 + x'^2}) \qquad \text{Eq (36)}$$

$$r = \sqrt{y'^2 + x'^2 + z'^2} \qquad \text{Eq (37)}$$

It is not necessary here to find the value for r, the radius of the spherical components, since we are only interested in the azimuth and elevation of the rotated system. Confirming that the radius is still 1 is a means of checking this rotation was performed correctly.

It was necessary to do compensate for the tilt of the ground as a separate step from the roll of the camera, since the roll of the camera, β, is in the coordinate system of the camera, which will be rotated in both θ and φ directions with respect to the coordinate system ground. This makes combining these rotations into a single step a more complicated geometry problem than applying two rotations to the individual coordinate systems.

Performing this translation enables more accurately estimating the effects of performing this correction than with equation _. A ±1° slope in ground slope can change the zenith angle viewed by the camera by half a degree or more, while changing the azimuth direction by ±2° (Table 6). This change in azimuth uses much of allowed error in estimating Azimuth (described in Section 3.3.6), demonstrating why it is necessary to know the ground slope for this form of camera system. This will be important to future iterations of the system which might have a less ideal surface.

*Table 6: Example of changes in the view angles, and field of view widths of the scientific camera when measuring a tilted ground surface. Table lists camera angles viewed when image is sampled at a rate of 3 times x 3 times. Camera aimed at 180° azimuth, with sun at a 135° azimuth.*

| No Rotation | | | | | FOV |
|---|---|---|---|---|---|
| Zenith | | 60.81 | 60.98 | 60.81 | |
| | | 44.97 | 44.97 | 44.97 | |
| | | 29.19 | 29.02 | 29.19 | |
| FOV | | 31.61 | 31.97 | 31.61 | |
| | | | | | |
| Azimuth | | 202.65 | 225.03 | 247.35 | 44.69 |
| | | 203.38 | 225.03 | 246.62 | 43.24 |
| | | 202.65 | 225.03 | 247.35 | 44.69 |

| | | $r_x$ = 1 | | | FOV |
|---|---|---|---|---|---|
| Zenith | | 61.19 | 60.99 | 60.43 | |
| | | 45.35 | 44.98 | 44.61 | |
| | | 29.59 | 29.03 | 28.83 | |
| FOV | | 31.60 | 31.95 | 31.6041 | |
| | | | | | |
| Azimuth | | 200.32 | 222.65 | 245.00 | 44.68 |
| | | 200.64 | 222.20 | 243.85 | 43.22 |
| | | 199.20 | 221.40 | 243.85 | 44.65 |

| | | $r_y$ = 1 | | | FOV |
|---|---|---|---|---|---|
| Zenith | | 59.88 | 59.98 | 59.88 | |
| | | 44.05 | 43.97 | 44.05 | |
| | | 28.27 | 28.02 | 28.27 | |
| FOV | | 31.61 | 31.97 | 31.61 | |
| | | | | | |
| Azimuth | | 200.73 | 223.32 | 245.86 | 45.13 |
| | | 201.30 | 223.32 | 245.29 | 43.99 |
| | | 200.24 | 223.32 | 246.34 | 46.10 |

| | | $r_x$ = -1 | | | FOV |
|---|---|---|---|---|---|
| Zenith | | 60.43 | 60.99 | 61.19 | |
| | | 44.61 | 44.98 | 45.35 | |
| | | 28.83 | 29.03 | 29.59 | |
| FOV | | 31.60 | 31.95 | 31.60 | |
| | | | | | |
| Azimuth | | 204.88 | 227.29 | 249.57 | 44.68 |
| | | 206.03 | 227.74 | 249.25 | 43.22 |
| | | 206.04 | 228.54 | 250.69 | 44.65 |

| | | $r_y$ = -1 | | | FOV |
|---|---|---|---|---|---|
| Zenith | | 61.73 | 61.98 | 61.73 | |
| | | 45.90 | 45.97 | 45.90 | |
| | | 30.12 | 30.02 | 30.12 | |
| FOV | | 31.61 | 31.97 | 31.61 | |
| | | | | | |
| Azimuth | | 204.69 | 226.85 | 248.96 | 44.27 |
| | | 205.57 | 226.85 | 248.08 | 42.52 |
| | | 205.14 | 226.85 | 248.51 | 43.38 |

### 3.6.6 Camera Misalignment

For the main camera near-nadir reflectance recovery experiment, the two cameras were fastened to an optical rail side by side, and the rail was used to measure the roll, zenith, and azimuth angles (Figure 31). Before these angles could be used to change the view angles into global BRF angles, it was necessary to estimate the camera's alignment with the rail. The scientific multispectral camera and the web camera had their alignment with the rail confirmed, as described in the calibration section 3.6.2. However, the web camera was knocked out of alignment early during testing. Due to schedule constraints, this misalignment had to be tolerated and measured later.

*Figure 31: Measuring the zenith and azimuth angles with respect to the optical rail.*

To measure the misalignment of the web camera, I found the pixel distance between the images taken by the two cameras for a small light source at a large distance from the cameras. Since there was a physical gap between the two cameras, points close to the camera system would show up in different pixels. To do this experiment, I first had to find the distance necessary to have a light source show up in the both center pixels for the two camera sensors if they had been perfectly aligned. To solve this, I estimated the angular difference between two pixels in both the scientific camera and the web camera. The value I found was 0.025°. This angle was then used to find the distance, D, for a triangle such that:

$$\tan(0.025°) = \frac{3.8\ cm}{D} \qquad \text{Eq (38)}$$

Which gives a distance of approximately 90 meters. To perform this experiment, I set up the cameras outside at night in a controlled area. I centered the field of view of the scientific camera on a light source 100 meters away. Since the light source had some size in the images, I used centroiding software to find the center of the light source in each image. To do this it was necessary to turn the image into a binary image, where all points below a certain threshold were black, and all above it were white. I tried these with multiple levels of brightness, to confirm that the center found was the same regardless of the parameters I put in. The variation I found in these values was less than a pixel. I repeated this experiment with three different light sources of different brightness to confirm that this was also not a factor. The variation I found due to this was also less than a pixel.

In this way, I could directly measure the pixel difference between the two images directly. The value I found for this was that the center of the image from the second camera was approximately 64 pixels to the left and 91.5 pixels above what was expected if the two cameras were perfectly aligned. Using the calibrations from section 3.6.2, this gives an angular difference between the two cameras of +4.8° in the zenith direction and -3.5° in the azimuth direction. When combined with uncertainty in the knowledge of the direction that the camera is facing, this is outside the specification for knowing the angle of the camera to within 5°. Since this is the case, we know that this was a necessary step for getting useful information out of the web camera.

To measure if there was also a roll angle associated with this misalignment, several images of the Teflon on the ground were examined, and a slope for it across the image was found. By comparing the slope across several images, it was found that the web camera also had a change in its roll angle of approximately 0.3°.

### 3.6.7 Measuring Lens Falloff

A camera viewing a uniformly illuminated object will not produce a uniformly illuminated image. Generally, as view angles increases, the illumination will decrease. I measured this effect for my cameras in order to differentiate between changes in measured radiance due to target BRF and those due to the lens falloff.

My plan was to use the flat field produced by a large aperture integrating sphere to approximate a Lambertian surface, and to measure the difference between the field measured, and the $\cos^4$ effect expected in the thin lens approximation. However, set up for the test showed a problem with this approach: A uniform Lambertian should be brightest when viewed at an angle perpendicular to the surface. I assumed that the camera could be ensured to be perpendicular to this surface by finding the point where readings were at a maximum. The camera was visually aligned to be perpendicular to the output of the integrating sphere, then its angle was adjusted to find the maximum. Two maximums were found, at approximately ± 10° from the visual approximation of alignment with the integrating sphere. These maximums were approximately 10% brighter than when the system was visually aligned. That there were two maximums, as well as the angular difference between them and a reasonable alignment showed that approximating that the output of the integrating sphere as being Lambertian was a mistake.

To compensate for this, I instead consistently aligned the cameras with a fixed point in front of the integrating sphere and measured the irregularity of the integrating sphere output by taking measurements with the ASD over a range of angles. Table 7 lists the angles used. Measurements were more densely packed for central angles since this was where the large irregularity was. Wider angles also resulted in hitting the edge of the sphere. The angles listed in Table 7 are the angles measured for the orientation of the ASD. These angles were then translated into theta and phi angles in a manner similar to that used in section 3.6.5.

As I do know the mechanics for this behavior, I sought the best fit, which was a 4th-degree polynomial function (Figure 32). Rather than being Lambertian, the output of the sphere was approximately uniform with some variation across the surface, with an offset from the center in the peak of the function.

*Table 7: List of angles measured to estimate the uniformity of integrating sphere output.*

| Pitch | Yaw |
|---|---|
| 0° | 0°, ± 3°, ± 6°, ± 9°, ± 12°, ± 15°, ± 18°, ± 21°, ± 24°, ± 27°, ± 30°, ± 33° |
| ± 5° | 0°, ± 5°, ± 10°, ± 15°, ± 20°,± 25°, ± 30° |
| ± 13° | 0°, ± 5°, ± 10°, ± 15°, ± 20°,± 25°, ± 30° |
| ± 20° | 0°, ± 5°, ± 10°, ± 15°, ± 20° |

I also performed a fit on the color data over a range of angles, going for a lowess fit using a quadratic function, which gave me a fit with $R^2$ of 0.9998 for the scientific camera and 0.966 for the web camera (Figure 32). Assuming an approximately uniform output for the integration sphere, it can be seen here that the scientific camera and lens has something approaching the power of cosine drop off that we would expect with a lens system. The web camera system has an odd drop off in the direction of negative theta. This is consistent with a misalignment of the lens, which could have happened in section 3.4.5: Web Camera Modification. With this in mind, it would be good for future web camera systems to be selected for easier modification and alignment of their lens system.

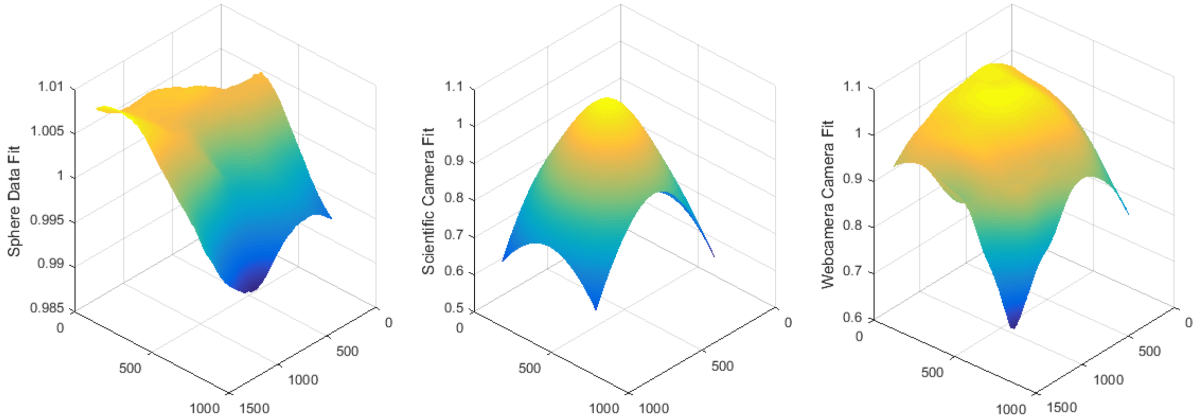

*Figure 32: Fits for the measurements of green band for the sphere uniformity, scientific camera falloff, and web camera falloff, for pixel numbers measured from the top left corner. All plots are scaled here by the value found at an azimuth and zenith angle of 0°.*

### 3.6.8 Linearity Calibration

The linearity of the cameras was tested using two methods: Changing the number of the bulbs in the integrating sphere, and changing the settings on the camera. For the scientific camera, it was possible to change the shutter speed, directly affecting the time the sensor was exposed to light. For the web camera, the relevant parameter that could be changed was the exposure value. There were complications with this latter calibration, which I will explore more at the end of this section.

Due to time constraints, it was only possible to take these data points with 1, 2, 6 and 10 bulbs when measuring with different numbers of bulbs in the sphere. Each bulb provided approximately the same irradiance. We can see that the linear fit for both cameras is fairly good for the limited number of points available. Adjusting the shutter speed of the camera provided more levels of incoming flux to confirm this linearity (Figure 33). This test was performed during the multiple bulb measurements, providing additional data to reinforce the linearity of the data. We can see that for the scientific camera that these fits are generally good, with an $R^2$ of 1 (Figure 34). It was planned that if there was non-linearity in this data, it would be necessary to adjust the DN values for that, but this step was not necessary.

Performing this calibration also confirmed the actual shutter speed of the camera, which could be adjusted to an arbitrary precision, but would 'snap' to an exact value. This experiment enabled finding what these exact shutter speeds were.

For the web camera, adjusting the camera settings to confirm the linearity was more difficult. Since the web camera had fewer digital levels and had a smaller dynamic range, it was

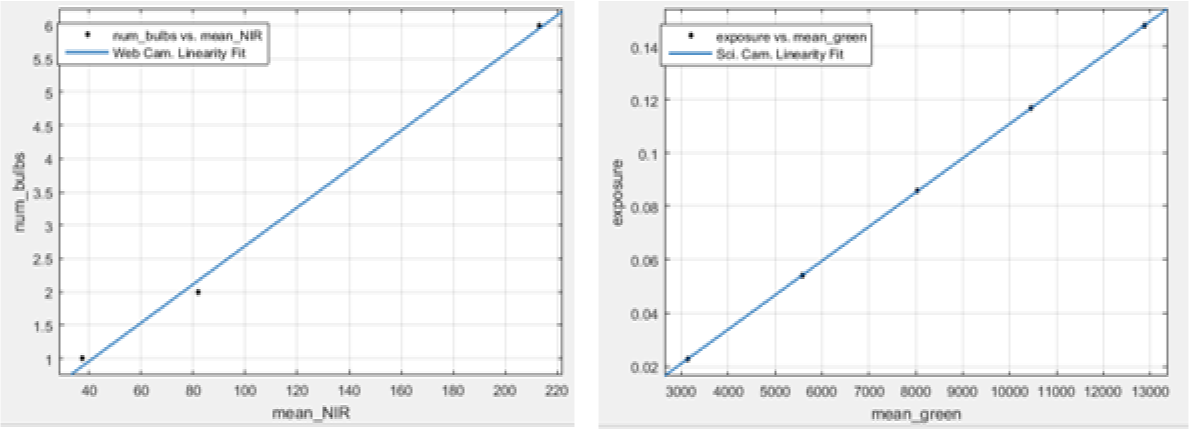

*Figure 33: Linearity fit for the number of integrating sphere bulbs used for the web camera in the NIR (left) and the scientific camera in the green (right).*

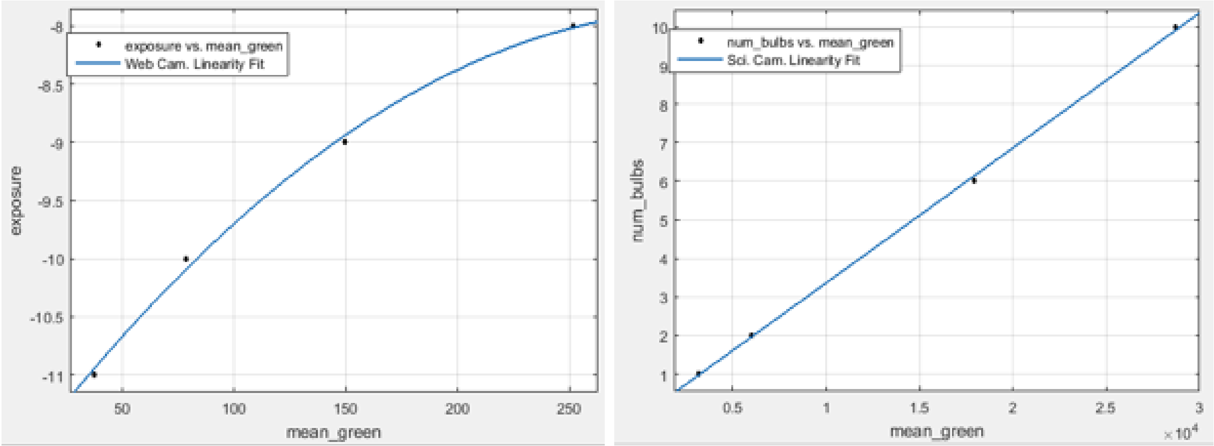

*Figure 34: Linearity fit using the camera exposure settings for the web camera in the NIR (left) and the scientific camera in the green (right).*

more difficult to get accurate readings over a large range of values. The relationship between the web camera 'exposure' and the readings is clearly non-linear (Figure 34).

If the exposure used by the web camera is the exposure value as used in photography, then we would expect the data to fit the equation:

$$EV = \log_2 \frac{f/_{\#}}{t} \qquad \text{Eq (39)}$$

Where EV is the exposure value, f/# is the f-number and t is the exposure time in seconds. This can then be rearranged to be:

$$t = \frac{f/_{\#}}{2^{EV}} \qquad \text{Eq (40)}$$

This is the reverse of the web camera's behavior, where increasing the exposure value provides more light to the system.

For an alternate definition of exposure is given by Greivenkamp (2004):

$$H = E't \qquad \text{Eq (41)}$$

Where H is the exposure (measured in $J/m^2$), E' is the image plane irradiance (in $W/m^2$), and t is time (in seconds). This should provide a linear relationship between the web camera readings, and the 'Exposure' setting, but this is also not the case. It is unclear here what the exposure setting is changing inside the web camera.

It was not possible to find a fit that consistently worked between all the ranges of values taken. As a result, the higher exposure values for the camera cannot be used to evaluate the linearity of the system, and the estimate made with the bulbs was necessarily the limit to what could be done.

This also meant that while it was theoretically possible to use multiple exposure values for the web camera in order to increase its effective dynamic range, in practice this required more analysis behavior of the exposure values used by this camera. Examining these processes for the web camera was instructive in reasons not to use web cameras for scientific work: While they might save costs individually, the time lost in adapting them, and learning their internal mechanisms is almost certainly a net loss for a project.

### 3.6.9 Temperature Response Relation Calibration

There are two parts to accounting for the effects of temperature on the response of the camera: The dark current of the camera, consisting of electrons generated by the sensor due to the ambient temperature energy and the change in sensor response with respect to the change in temperature. The latter is a less known source of noise since its effects tend to be minor, and are mitigated when measurement systems are in an environment with a controlled temperature. Research on this subject tends to show up most frequently for space fairing sensors. As the fluctuations of temperatures in the desert can also be fairly severe, I accounted for them for my camera system as well.

Measuring the temperature of the sensor, both in the field and in the calibration was done with a Thorlabs TSP01 USB Temperature and Humidity Data Logger, with external probes attached to the exterior of both cameras. This sensor provided a software suit to measure and record the temperature of the probes, with an accuracy of ± 0.5° C. It did not integrate with Matlab, but produced text files that could be imported. It was not necessary to absolutely calibrate the temperature sensor. Since it was used in all the readings taken, it would provide the necessary measurement of the relative change in temperature, which could then be correlated with the response of the sensor.

As the probes were attached externally to the cameras, instead of internally, directly on the sensor, there would be a delay between a change in external temperature and that of the internal temperature. The delay between temperature changes can be estimated using a chart of the response versus temperature using a steady source of light. Measurements of the external temperature should flatten out before the response change does. We can measure this difference. It was observed that the difference between the points where they flatten was negligible. To make sure this delay was not an issue with the field readings, the temperature used for calibrating those readings was the average over the entire time that readings were taken.

Heating and cooling the camera system for this experiment also focused on finding a low cost and readily available method of testing. The temperature of the camera system and the ASD was adjusted using a Nesco American Harvest FD-61WHC, employing cardboard to contain the hot air and provide insulation. While this heat source is designed for dehydrating food items, it was found to provide a large and steady temperature change, when compared to other consumer grade items. Cardboard, while unconventional, provided adequate insulation, and was easy to rebuild into shapes conducive for testing the camera system while incorporating the heating element. Providing holes for the cameras did not significantly change the range of temperatures that the heat source could produce. At its max settings, it produced temperatures for the cameras in excess of 55°C, which was the maximum specified temperature for the cameras, and which matched well with the possible temperatures in southern Arizona. At its lowest setting, the heating element provided cooling to the camera system by blowing air on it, lowering the temperature to the range of 40°C, depending on the ambient temperature around the camera system.  By alternating between these settings, it was possible to consistently produce a wide range of temperatures.

For the dark current calibration, I blocked the input to the sensor while recording their output at various temperatures. For the ASD, and scientific camera, it was possible to black them out using lens caps. For the web camera, which did not have a lens tube, it was necessary to wrap it in black foil. When the difference in signal was measured for all these sensors at the maximum and minimum temperatures, there was a negligible difference in the dark current. For the web camera there was no signal, regardless of temperature. For the scientific camera, and the ASD, there was a change in the signal of just a couple DN, with a signal in the thousands. I decided that adjusting for the dark current with respect to the temperature was overworking the problem in this case, and treated the value as a constant.

For the response vs temperature calibration, I made use of an integrating sphere owned by the Remote Sensing Group. This provided a means of having steady, near-Lambertian light source. For a more low cost and readily available options, there has also been research into using sunlight as a source (Thome et al., 2008), and blue sky calibrations (Dymond & Trotter, 1997) for cameras. Researching those further fell outside the scope of this project.

With the camera and the ASD, temperature changes were measured using two bulbs in the integrating sphere. This provided enough light in order to be significantly above the dark current, without flooding the web camera. For the cameras, the digital number assigned was the average measured over the center 50 pixels for the sensor. The center pixels were found to provide a steadier signal than an average taken over the entire sensor. The lens array was also left on both cameras for these readings. It was impractical to remove the lens array for the web camera, and this kept the methods consistent between the two cameras.

When measuring the change in response, I observed that this had a spectral aspect to it. With the scientific camera, the readings in the blue, green and red went down when the temperature increased, while the NIR had a positive change in readings when the temperature increased. For the web camera, only the blue had a negative change in readings when temperature increased, while the green, red and NIR all had positive changes. The ASD had all positive changes. For all cases, the change in the NIR is more positive than the change for the blue.

The amount of change was generally very small, as can be seen in Table 8.

*Table 8: Estimates of the % change in signal per degree Celsius.*

| | Blue | Green | Red | NIR |
|---|---|---|---|---|
| Scientific Camera | -0.5% | -0.1% | -0.3% | 0.2% |
| Web Camera | -0.18% | 0.07% | 0.07% | 0.07% |
| ASD | 0.025% | 0.025% | 0.038% | 0.033% |

For the ASD, and the web camera, these changes in response were small enough that they might be neglected. For the scientific camera, they were large enough to affect the data when there could be a 15°C change in temperature over the course of a day. Changes in the blue, green and red would be negative while the NIR would be positive as temperatures increased. This would improve the apparent health of the grass as the temperature increased, as might be measured by the NDVI.

$$NDVI = \frac{(NIR - VIS)}{(NIR + VIS)} \qquad \text{Eq (42)}$$

Where NIR and VIS are the measured reflectance in the near infrared and visible.

### 3.6.10 Digital Number to Reflectance Conversion

To convert the measurements made by the cameras and ASD into estimates of reflectance, it was necessary to perform a calibration between the digital numbers and reflectance. This may be done by absolutely calibrating the system, or reading by reading. In the latter case, a near-Lambertian target with reflectance near 100% is used to estimate the downwelling light, and is then ratioed with the light reflected from the surface being measured, such as turfgrass.

$$\frac{R_{LAMB}}{R_{SURF}} = \frac{DN_{LAMB}}{DN_{SURF}} \qquad \text{Eq (43)}$$

Where $R_{LAMB}$ and $R_{SURF}$ are the reflectances of the Lambertian and the surface whose reflectance we are trying to measure, and $DN_{LAMB}$ and $DN_{SURF}$ are the digital numbers our radiometer measures. Ideally, the downwelling radiation measured should be only the direct solar radiation, but in practice it will be the global irradiance.

For absolute radiometric calibration of the cameras, the DN produced by the camera is associated with a known radiance. This method is of interest to the project, because it is the one that would have to be used by an end user of a fully developed camera system for radiometric calibration. Absolute radiometric calibration requires an estimate of the downwelling radiation to provide an estimate of the reflectance. Since this would have required additional equipment or work on the atmospheric analysis, I decided against this route for the preliminary testing of the system. I explored the option more in the section 4.2.7.

For this experiment, I used a sheet of Teflon as a near Lambertian reflector. This sheet of Teflon is described in more detail in section 3.5. At the beginning of the day the Teflon sheet was placed in the field of view of the ASD. This was confirmed by shading the area from direct sunlight and using a consumer grade 1 mW 532 nm laser mounted on a tripod. The laser's point produced a distinctive peak in the readings when within the field of view of the ASD. After all parts of the Teflon were confirmed to be within the field of view of the ASD, the position was marked, and the camera was aimed to also have the Teflon within its field of view.

The ASD readings were converted to a reflectance estimate using Eq (43), modified according to the non-Lambertian behavior noted in Figure 23. The cameras used a similar process, but the Teflon did not fill their field of view, so it was necessary to use the falloff data derived in section 3.6.7 to estimate the digital number that would be measured in the sections of the field of view without the Teflon.

# 4 System Evaluation

## 4.1 Field Work

### 4.1.1 Introduction

One method of evaluating the quality of BRF models, and their inversions, is to compare the root mean square error between an actual BRF and an estimated BRF over the hemisphere of possible input and output angles (Roujean, Leroy, & Deschamps, 1992 ; Hu et al., 1997 ; Liangrocapart & Petrou, 2002). This method did not meet the needs of this project since it required either acquiring or building and testing a goniometer, both challenging tasks. In addition, satellite systems often view the Earth from a limited set of angles. SPOT, IKONOS, LISS-IV, Quickbird, and ASTER are all capable of viewing the earth off-nadir, but all do so by less than 31°. All these satellites have sun-synchronous orbits, which will limit the possible sun angles in an image. Similarly, the camera system is likely to view the calibration target from an angle closer to the ground for practical reasons. Since BRFs and their models can change significantly at steep angles (Figure 3), it makes little sense to give equal weight to steep sun and sensor angles which are both less likely to occur in practice, and more likely to produce inaccurate estimates of at-sensor radiance. Doing so would unnecessarily reject camera systems that would work under operational conditions.  Thus, as others have done, I took measurements at a limited number of angles, based on those that are likely and logical to exist (Goodin, Gao, & Henebry, 2004 ; Gianelle & Guastella, 2007). Simulations I performed to examine the PROSAIL BRF, as in section 3.3, recovering the reflectance for zenith angles between 0° and 30° found the largest error in recovery to be either at-nadir or at a zenith angle of 30°, with all other angles producing values between those extremes. For my testing, I focused on data taken at 30°, since placing the ASD sensor at zenith produced self-shadowing problems that would have been difficult to account for.

### 4.1.2 Metric for System Quality

This experiment was kept small scale to enable testing the feasibility of the use of cameras for radiometric correction while keeping the investment of time and money reasonable. For a grass target, a large patch of Princess Bermuda turfgrass was selected. Princess Bermuda turfgrass was ideal for the small scale experiment since it is a planophile breed of grass with small leaves, which prevented the grass from having large amounts of self-shadowing. This was a concern, since in a full-scale camera system, looking at something closer to 30 by 30 meter plot of tended, would not be expected to have to deal with this problem. Princess Bermuda is quite thick, which provided a high LAI, and prevented soil from showing through.

The grass existed at a site owned and maintained by the Karsten Turfgrass Center of the University of Arizona and was used with their kind permission. It was regularly mowed and fertilized to maintain uniform greenness throughout the months measurements were being taken. While the mowing did mean that the length of the grass did change some days between readings, this was preferable to the grass becoming long to the point of being a volume structure.

Each day where measurements were taken, a different patch of grass was selected for the readings being taken that day: healthy grass or distressed grass. While taking readings from the same target on consecutive days would have been desirable, to eliminate natural variation in grass health as a potential source of unaccounted for variability, proved impossible due to intermittent weather. In addition, taking data often distressed the patch of grass surrounding that used for the calibration target, through periodic covering with the Teflon and foot traffic around the equipment.

The area used for a small scale grass calibration target was constrained by the size of the Lambertian object available for converting the ASD data from digital numbers to reflectance. A specially manufactured 1-foot square Teflon target was selected for this. Simulations showed that depending on the level of surface variability (see section 3.3.13), that it was important for the camera to cover as much area in common as possible, otherwise the area sampled by the ASD may not be representative of the area sampled by the camera system.

The majority of these experiments were done on the scientific camera, as the results from the web camera were disappointing. Since it took time to grow each look-up table, and it was necessary to grow different look-up tables for each camera, due to their differing fields of view, it did not make sense to confirm or compare the poor performance of the web camera in all instances.

To measure the range of error in the system, it is necessary to take more than one reading in a similar setup. With the sparsity of clear sky days, it was frequently not possible to take readings at similar angles for days in a row. Instead, it is necessary to compare readings throughout the day. As the sun advances across the sky, there will be different solar zenith and azimuth angles. It is hoped that this will change things enough that the weaknesses of the system will be exposed. The mean value difference and the standard deviation of the difference over the course of a day will be the values reported here, and used to evaluate the overall system quality.

### 4.1.3 Measuring Zenith, Azimuth, and Roll Angles

I used a Suunto MC-2G compass to align the camera and ASD with the desired angles East of North. This was a two-step process because of distortions in the magnetic field caused by the equipment itself. In the first step, the compass was held well away from the equipment and used to sight a distant object at the correct azimuth. If no convenient object was present, I would create one by attaching a colored cloth to the fence surrounding the Karsten Turfgrass Center. Once an object at the correct azimuth was found or created, it was possible to take the compass, place it alongside the camera or ASD, and shift them until the compass again sighted the object. The local magnetic field was 10° 2' E ± 0° 20', and was included in the estimate of Azimuth.

After the azimuth was determined, I would find the roll angle of the camera and ASD. This was done by placing the rails of the camera system and the head ASD so that they were level with respect to the zenith angle, then measuring their roll angle. Attempts were made to decrease this roll angle to within less than half a degree by adjusting the height of the legs of the tripods. It was necessary after this step to again check the azimuth angle again. This was iterated until the roll angle was within ± 0.2°. After this, the zenith angle of the camera and ASD were adjusted to 45° ± 0.2° and 30° ± 0.2° respectively.

## 4.2 BRF Experiments

### 4.2.1 PROSAIL LUT Range Calibration

In simulations, it was possible to see that both the range of the LUT used, and the number of BRF examples averaged in the recovery influenced the accuracy of the recovered reflectance. As a part of the analysis, I decided to confirm this behavior with the measured data. This provided an opportunity to confirm the range of inputs used for the PROSAIL inversion were calibrated to provide optimal data from the measured data.

To limit the number of look-up tables that needed to be generated, I began this process by looking at the data produced over several days, focusing on a single time of day, 11:30. This placed the sun high in the sky, which would minimize the effects of the non-Lambertian nature of the Teflon. Since clouds tended to get stronger as the day went on, this provided the clearest set of data to compare between. I examined both distressed grass and healthy grass with the camera at several different angles with respect to the ASD, focusing on clear days. I began by exploring the effects of the spatial sampling rate and the blur of the image on the resulting PROSAIL BRF recovery.

I performed the experiment using a mean of the 15 closest BRFs found to estimate the reflectance that should be observed by the ASD (see section 3.2.2 for more details on using multiple BRFs in the PROSAIL inversion). Experience with the simulation of this system indicated that it provided enough samples to take advantage of the averaging power of the BRF recovery algorithm. At the same time, this provided few enough examples that there should be significant changes in the resulting BRF estimate if some change to the LUT generation process should reorder which tables were closest to the readings. I confirmed this was also the case with the field data.

The result of these analyses was to find that the blur and sampling had no substantial effect on the resulting BRF estimate. Blur had very little effect on the output. No blur or a blurring via a mean value convolution of the image using a 15 x 15 grid did not substantially change the resulting BRF values produced. This was unexpected, as there were concerns that it was possible to sample a self-shadowed point, and thus find an incorrect estimate of BRF.

Testing the sampling rate lead to inconsistent results. I tested the results from the series of surfaces mentioned earlier with the PROSAIL program and a sampling rate of 1 x 1, 3 x 3 and 5 x 5, to confirm that when more pixels were added, the values converged on one that was closest to the expected value. This was not the result I found. Instead, I found cases where 1 x 1, 3 x 3 and 5 x 5 image sampling were each the best answer. After a very small number of samples of the image, the estimate of BRF provided converged on a single value, which did not always happen to be the right value. Sampling a single center pixel, and a 3 x 3 grid both provided substantially different values, but samples taken on odd grids of 5 x 5 to 31 x 31 provided very little change in the recovered BRF for PROSAIL. Some minor variation in the numbers after this point indicates that the additional samples were enough in order to rearrange the BRFs that were considered closest, but there was not enough to produce significant changes in the BRF estimates produced.

I needed a metric to determine which was the proper number of image samples to use in the rest of the analysis. I narrowed down the options to an image sampling rate of 3 x 3 or 5 x 5. Sampling only the center pixel defeated the purpose of using a camera system, while rates higher than 5 x 5 produced results consistent with the 5 x 5 sampling, so there was no reason to use these. As in section 3.2.3, where I set up the LUTs for the simulation step of this dissertation, a sampling the image in a 3 x 3 grid provided samples in each corner of the image, which would provide knowledge of the direction of the BRF. A 5 x 5 sampling of the image would provide both knowledge of the direction of change for BRF, as well as an estimate of its rate of change. A 5 x 5 image sampling rate also provided the result closest to the fixed values that came after.

One concern with the fixed values was that they might be an artifact of the LUT inversion. I had found in my early experimentation with the field data that in some cases it was possible for an extreme outlier data point to cause the LUT inversion to fixate on a particular solution, even if this solution was wrong. It was possible that by expanding the sampling rate, the chances of sampling one of these outliers increased, and was forcing the inversion into a fixed answer. Further investigation into this problem in the inversion is merited.

A 3 x 3 sampling of the image required generating 64% fewer estimates in PROSAIL than did a 5 x 5 sampling of the image. Since these two samplings produced similar values, sampling the image with the 3 x 3 grid provided an opportunity to sample the possible inputs for PROSAIL more finely or over a larger range, which could provide improved estimates for the BRF. The initial analysis showed that the default PROSAIL values used from Table 2 did not cover distressed grass well. It was not possible for the inversion with the initial range specified for to find input values that produced reflectances in the red that were near or above those in the green. To represent these values, it was necessary to increase the range of the input values used for the chlorophyll content and the water content of the leaves. This produced worse results for the healthy grass though. To compensate for this I added to the number of tables sampled in the range for the leaf water content.

I experimented with the possible input ranges and their sampling rates that would be possible if I used a smaller sampling rate for the images. I began in this part to experiment with sampling the input values at different rates. The performance was improved in some cases by increasing the sampling rate, as with the leaf area index, and the chlorophyll content. In experimenting with values that I had previously held to a constant single value, carotenoid content, brown pigment, and the hotspot parameter, only small effects were found by varying these parameters.  I found through experimentation that some performance improvement could be made by varying across skylight. This doubled the number of tables it was necessary to generate, though. To compensate for the increased number of tables, I also experimented with decreasing the sampling rate of various inputs. I found little effect for decreasing the sampling rate for the soil reflectance. I ended up with the sample ranges and rates listed in Table 9.

*Table 9: A list of the input values used for PROSAIL in the experiment comparing increased sampling of the image versus increased sampling of the PROSAIL input values.*

| INPUT VARIABLE | MIN VALUE | MAX VALUE | SAMPLED INPUTS |
|---|---|---|---|
| **LEAF AREA INDEX** | 2 | 10 | 6 |
| **LEAF INCLINATION DISTRIBUTION FUNCTION** | 10 | 80 | 4 |
| **SOIL REFLECTANCE PARAMETER** | 0.2 | 0.8 | 3 |
| **CHLOROPHYLL A AND B CONTENT** | 5 | 80 | 6 |
| **LEAF STRUCTURE PARAMETER** | 1.1 | 1.9 | 4 |
| **EQUIVALENT WATER THICKNESS** | 0.001 | 0.03 | 6 |
| **DRY MATTER CONTENT** | 0.00025 | 0.0075 | 6* |
| **CARATONOID CONTENT** | 8 | 8 | 1 |
| **BROWN CHLOROPHYLL CONTENT** | 0 | 0 | 1 |
| **HOTSPOT PARAMETER** | 0.1 | 0.1 | 1 |
| **SKYLIGHT PARAMETER** | 0.075 | 0.125 | 2 |

I performed an experiment to choose between the sampling the image at a higher rate, and sampling the input values for PROSAIL at a higher rate. I looked at data taken with the camera at a 45° angle with respect to the ASD, for both healthy and distressed grass, as this would provide the most insight to when the system was working under non-ideal circumstances, and when a greater range of values for the inputs might benefit it the most.

*Table 10: Change in the estimated performance due to image sampling rate, when viewing healthy and distressed grass with ASD azimuth angle of 180° East of North and camera azimuth of 225° East of North. Mean Error is the difference in the reflectance measured by the ASD and the reflectance estimated by the camera system in the direction in the ASD. Reflectance estimates and measurements were generated throughout the day and the mean error is the mean of the error in these data. Similarly, the STD is the standard deviation in these data taken throughout the day. These errors are further split into an error for the NIR and an average of the error found for all three of the visible bands. These errors are expressed as the linear change in the reflectance, R (or ρ), rather than the percent change in the readings.*

| | Image Sampling | Mean Visible Error | Mean NIR Error | STD Visible | STD NIR |
|---|---|---|---|---|---|
| Healthy Grass | 3 x 3 | 0.96% R | 6.5% R | 0.58% R | 2.8% R |
| | 5 x 5 | 0.79% R | 6.5% R | 0.22% R | 2.3% R |
| Distressed Grass | 3 x 3 | 5.7% R | 7.8% R | 1.6% R | 5.2% R |
| | 5 x 5 | 4.8% R | 6.9% R | 0.74% R | 5.2% R |

I found that the increased ranges for PROSAIL input values improved the results for the cameras. However, the performance increase from the increased sampling for the image was greater than the performance increase from the increased sampling of the PROSAIL input ranges. As a result of this experiment, I focused on sampling a 5 x 5 grid of the image, and with a blur of a 5 x 5 mean value. While blurring the image did not show itself to significantly improve the process, it was mathematically simple to do, and avoided concerns for self-shadowed pixels. I did not vary over the skylight parameter in this case because it required generating too many example BRFs.

The final value to adjust in the PROSAIL inversion was to adjust the weights given to each band. Unlike in the simulated case, I found that providing unequal weights to the visible and NIR was significantly detrimental to the overall results of the inversion. The visible reflectances produced by the field data showed considerably more variation than the simulation data, particularly in the red and green bands. This made them more important in processing the field data than they were with the simulation. I gave the bands equal weights within the PROSAIL inverse.

### 4.2.2 Effect of Sun Angle on Recovery

It became evident while first examining the data that the Teflon target had a non-Lambertian specular reflection in the forward scatter direction (Figure 35). As a ratio of digital numbers was used to find the reflectance (Eq (43)), increased reflectance in the forward direction by the Teflon artificially lowered the estimated turfgrass reflectance for both the cameras and the ASD. When there was an azimuth offset between the detectors, the specular reflection would result in diminished readings for one and not the other (Figure 35). This decreased the correlation of the reflectance estimates for the two detectors, increasing the system error.

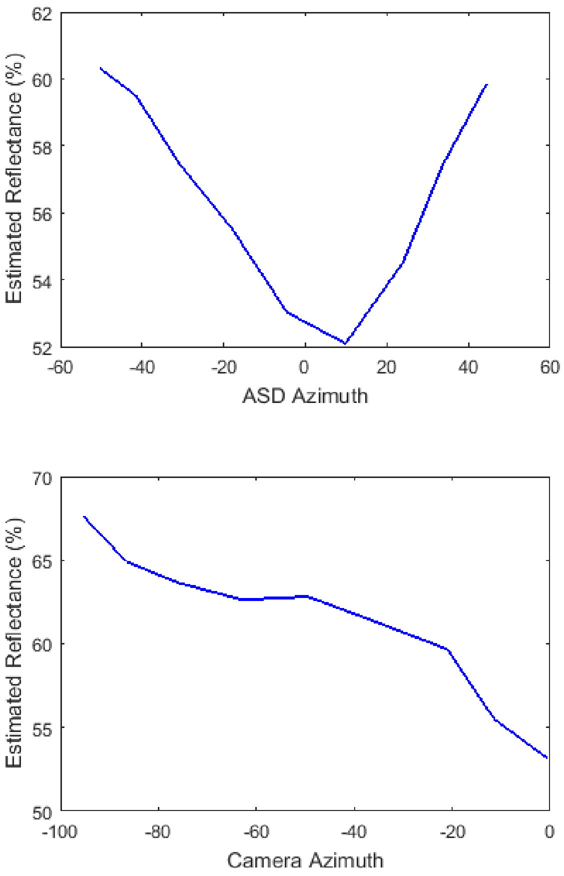

*Figure 35: Estimates of the NIR reflectance, found for the ASD using a simple ratio, and found using PROSAIL for the scientific camera. Azimuth is measured here from the forward scatter direction of the solar plane. Example is healthy grass with the camera at a 45° azimuth angle with respect to the ASD. Data from left to right was taken from 10am to 2pm.*

The mean change in the reflectance measured by the ASD over the course of a day was 9.2% reflectance for the NIR band, while the mean change for the visible bands was 1.6% reflectance. The error in reflectance estimates due to the Teflon target's specular reflection made it difficult to evaluate the absolute error in the system due to the camera design. However, it is possible to evaluate the relative error of the different configurations. To aid the comparison of data taken on different days, I limited the data points I examined to those that had been taken at a time of day that crossed over all the available data sets, and took the same number of data points from each set. This placed the sun in a common region for all of the data sets, preventing changes in the mean error of the system that would be due to a change in the range of sun angles used. Table 11 shows how this range change effects the estimated error. Excluding wider solar angles, which this data would not have in common with other sets, produces a higher average error for the system.

*Table 11: Change in the estimated performance due to the sun range used, when viewing healthy grass with ASD azimuth angle of 180° East of North and camera azimuth of 225° East of North. The definition of error used here is further explained in Table 10.*

| | Mean Visible Error | Mean NIR Error | STD Visible | STD NIR |
|---|---|---|---|---|
| Full Data Range | 0.79% R | 6.53% R | 0.22% R | 2.32% R |
| Limited Data Range | 0.83% R | 6.65% R | 0.27% R | 2.87% R |

### 4.2.3 Effects of Camera Angle on Recovery

I examined the results of viewing the grass at various angles to better understand this as a source of error (Table 12). As could be expected from section 4.2.2, the mean error in both the visible and NIR range increased with the difference in azimuth angles for the cameras and the ASD.

*Table 12: Change in the estimated performance due to camera view angles, when viewing healthy grass with ASD azimuth angle of 180° East of North and camera view azimuths of 180, 225 and 270° East of North. The definition of error used here is further explained in Table 10.*

| Camera Angle | Mean Visible Error | Mean NIR Error | STD Visible | STD NIR |
|---|---|---|---|---|
| 0° | 0.39% R | 1.36% R | 0.12% R | 1.31% R |
| 45° | 0.83% R | 6.65% R | 0.27% R | 2.87% R |
| 90° | 3.5% R | 15.18 %R | 0.2% R | 1.91% R |

The standard deviation over the range of readings taken is not as high as might be expected. While the accuracy is lower at the higher difference in azimuth angles, the resulting reflectance estimates cluster, giving it high precision. It is possible the system could be calibrated to better account for the mean error which is either due to specular reflection or some element of the camera system.

The data set taken with a 0° difference in the azimuths for the cameras and ASD should have the least amount of error due to the Teflon's specular reflection. For this data set, both the visible and the NIR are within the specifications set for the system to be considered successful (see section 3.3.2). If we consider only the standard deviation in the difference between the estimated reflectances for the ASD and the scientific camera, and assume that the offset can be calibrated for, then both the 0° and 90° azimuth difference data sets are within the specifications required for success. It is likely that the 45° data set would be within this specification, if not for the angle of specular reflection also crossing the cameras field of view over the hours analyzed (Figure 35). Future work is merited to confirm these results in cases where specular reflection could be avoided or accounted for.

### 4.2.4 Camera Comparison

To understand the limits of cameras to find BRF, I experimented with both a scientific camera and a web camera. I began with the average reflectance values recovered in a best case scenario, where the camera and the ASD are at the same azimuth angle, and viewing healthy grass.

*Table 13: Camera performance comparison when viewing healthy grass with camera and ASD azimuth angles of 180° East of North. The definition of error used here is further explained in Table 10.*

| | Mean Visible Error | Mean NIR Error | STD Visible | STD NIR |
|---|---|---|---|---|
| Scientific Camera | 0.39% R | 1.36% R | 0.12% R | 1.31% R |
| Web Camera | 1.23% R | 9.24% R | 0.25% R | 2.80% R |

The web camera's performance across the board is worse than the scientific camera, but is particularly poor in the NIR. To better understand the limits of the web camera implementation of the BRF camera system, I examined its performance with healthy and distressed grass, with a 45° angle between the camera and ASD.

*Table 14: Camera performance comparison when viewing healthy grass with ASD azimuth angle of 180° East of North and camera azimuth of 225° East of North. The definition of error used here is further explained in Table 10.*

| | Mean Visible Error | Mean NIR Error | STD Visible | STD NIR |
|---|---|---|---|---|
| Scientific Camera | 0.83% R | 6.65% R | 0.27% R | 2.87% R |
| Web Camera | 2.45% R | 10.74%R | 0.76% R | 6.24% R |

*Table 15: Camera performance comparison when viewing distressed grass with ASD azimuth angle of 180° East of North and camera azimuth of 225° East of North. The definition of error used here is further explained in Table 10.*

| | Mean Visible Error | Mean NIR Error | STD Visible | STD NIR |
|---|---|---|---|---|
| Scientific Camera | 4.02% R | 7.58% R | 0.50% R | 4.94% R |
| Web Camera | 5.11% R | 14.24% R | 0.62% R | 6.28% R |

The web camera continues to produce poor results in both these cases. With the distressed grass, the reflectances produced by the web camera are closer to those of the scientific camera than in other cases. This is possibly because of the limitations of the PROSAIL inverse. The errors in this case are already high, and the finite size and range of the LUT inverse limit how far the estimated reflectance can be moved from the measured data. Examining the data used to produce the reflectance estimates for the web camera, I identified three sources of performance issue: Camera dynamic range, interaction with the PROSAIL LUT inverse, and read noise.

Dynamic range was not included in the simulations as a possible source of error, but is the most clear source of error within the web camera data. The web camera data was taken at two different exposure settings. At the higher exposure setting, there are cases where the DNs produced reach the maximum possible value of 255 when viewing the Teflon. Because DN for the peak reflectance of the Teflon should be higher than the recorded value, the estimated reflectance for the vegetation will be too high. This can be observed in Figure 36, where there are reflectance values as high as 20% in the green. If the lower exposure setting for the web camera was used, in many cases the measured DN for the turfgrass was zero. Thus, at the lower exposure setting, many of the reflectances are also in error, and too low.

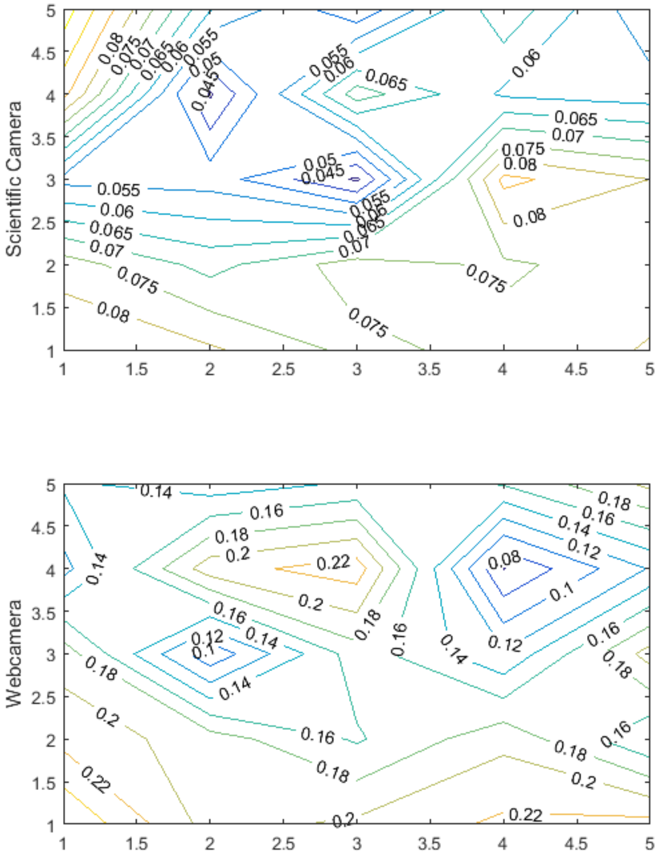

*Figure 36: Contour maps of the estimated reflectance across a set of samples for the scientific camera and web camera. Data point is one taken at noon using healthy grass, with camera and ASD azimuth angles of 180° East of North.*

This leads to the second source of error I listed: interaction with the PROSAIL LUT inverse. One of the strengths of the

PROSAIL inverse is that the reflectance bands are interdependent, based off the physical reflectance mechanics of vegetation. As such, a non-physical reflectance such as 20% or 0% reflectance in the green makes it impossible to find an example BRF in the PROSAIL LUT that closely matches the reflectance data. Because of this, even if the reflectance data for other bands does not hit the top or bottom of the dynamic range, one band doing so will reduce the quality of the reflectance recovered for all the bands. For this analysis, I found that the numbers produced by the higher exposure value produced better results.

To demonstrate that overestimating the green reflectance was a significant source of error in the other bands as well, I reran the PROSAIL inverse on the web camera reflectance data, with no weight given to data from the green band (Table 16). This improved the performance across the visible spectrum, including in the green band, with both healthy and distressed grass. For unknown reasons, excluding the green band from the inversion also produced slightly worse results in the NIR.

*Table 16: PROSAIL inversion comparison, run with and without reflectance from the green band. Performed on healthy and distressed grass with ASD azimuth angle of 180° East of North and camera azimuth of 225° East of North. The definition of error used here is further explained in Table 10.*

| **Healthy Grass** | Mean Visible Error | Mean NIR Error | STD Visible | STD NIR |
|---|---|---|---|---|
| With Green R Data | 2.45% R | 10.74%R | 0.76% R | 6.24% R |
| Without Green R Data | 0.73% R | 11.45% R | 0.17% R | 6.27% R |
| **Distressed Grass** | Mean Visible Error | Mean NIR Error | STD Visible | STD NIR |
| With Green R Data | 5.11% R | 14.24% R | 0.62% R | 6.28% R |
| Without Green R Data | 4.00% R | 16.61% R | 0.17% R | 6.30% R |

The final source of noise I noticed in the web camera reflectance data was read noise. This random noise in the web camera readings is visibly high, even with the blur convolution applied to it (Figure 36). Both the cameras have some fluctuations in their reflectance values, but the web camera in particular jumps between 22% and 8% reflectance without a pattern.

### 4.2.5 Environmental Effects on Reflectance Recovery

An additional concern with the BRF camera is the site where it is set up and the weather conditions when it is being operated. Grass has good temporal stability and uniformity in its spectral signature when it is maintained (B. Clark et al., 2011), and can be used for calibration provided that it is monitored (P. M. Teillet et al., 2007). However, when turfgrass is not maintained it can have considerable changes in reflectance, due to wear and water stress.

One motivation for this research is to move surface monitoring out of the desert to learn more about the atmosphere in other regions. This makes the camera performance in the presence of clouds of interest. It is possible that the increased non-direct light would defeat the BRF recovery. I contrast here the recovery with healthy and distressed grass, and clear days with days with overhead clouds. These classifications were made, as per Figure 37 and Figure 38.

*Table 17: Scientific camera viewing healthy and distressed under different cloud conditions grass with the ASD aimed at 180° East of North, and the camera aimed at 225° East of North. The definition of error used here is further explained in Table 10.*

| Healthy Grass | Mean Visible Error | Mean NIR Error | STD Visible | STD NIR |
|---|---|---|---|---|
| Clear Day | 0.83% R | 6.65% R | 0.27% R | 2.87% R |
| Overhead Clouds | 0.76% R | 6.91% R | 0.27% R | 3.11% R |
| Distressed Grass | | | | |
| Clear Day | 4.02% R | 7.58% R | 0.50% R | 4.94% R |
| Overhead Clouds | 4.58% R | 7.72% R | 0.61% R | 5.19% R |

The PROSAIL LUT inversion I implemented is less capable of modeling distressed grass than healthy grass. The majority of the change in error between healthy and distressed grass is in the visible range. PROSAIL was unable to compensate for the increased reflectance in the green and red for distressed vegetation. This may have been due to the range of inputs used to generate the LUTs, though experiments to a better range for input variables did not succeed. As an additional experiment, I tested the linked values of Equivalent Water Thickness and Dry Matter Content. I fixed these values to each other, based on the work by (Vohland & Jarmer, 2008), to keep the size of the LUTs down. I repeated the analysis for the distressed grass,

*Figure 37: Examples of healthy (left) and distressed grass (right)*

*Figure 38: Examples of Clear weather (left) and Overhead clouds (right)*

changing the ratio between Equivalent Water Thickness and Dry Matter Content from 1/4 to 1/2, and found that this produced no better results. Exploring the capacity for PROSAIL to be compatible with distressed grass is an area for future research.

Having clouds overhead had little impact on the data quality. This is not because the data is unchanged; there are discrepancies in the ASD reflectance between the data sets of up to 6% for readings taken at the same time of day. It is not an artifact in this case of the data already having a maximum in error, as it was the case with the web camera data viewing distressed grass. This may be a result of finding reflectance using the ratio method. Measuring the Teflon before each reading set should provide some information about the skylight as well, and any decreased transmission that might result. Cloud cover's effect on estimated BRF is a problem that should be looked into in more detail in a case where absolute radiometric calibration is available.

### 4.2.6 Quality of AMBRALS Correction

The analysis so far has been for BRF data. AMBRALS is instead a BRDF function. The BRF of a surface is a measure of its percent reflectance as compared to an ideal Lambertian. BRDF is the measure of the percent of light reflected from one direction to a second direction. The quantities are related, but not the same. Thus, before making use of the AMBRALS inversion, it is necessary to convert the BRF data I have been using into BRDF data. This can be done with Eq (2), which is just linear multiplication by π. After the BRDF numbers are calculated, we can convert these back to BRF numbers using the same equation. As the AMBRALS algorithm is a set of linear equations, these steps cancel out, and can be skipped.

To begin the analysis of the quality of AMBRALS as an inversion in for the camera system, I sought proper image sampling rate for this algorithm. As there were no example BRFs to generate, it was possible to sample at a much higher rate than was possible with the PROSAIL algorithm. As can be seen in Figure 39, increasing the sampling rate does not consistently improve the quality of the resulting inversion. The error is smaller in the visible bands, but shows a similar pattern, where some higher sampling rates produce more error than a lower rate. Sampling 201 x 201 pixels of the image also produced poor results. All this indicated that no sampling rate could be relied upon to produce quality results across all sets. To perform the analysis, I selected a sampling rate of 19 x 19, as this had the best performance across the bands in the initial analysis.

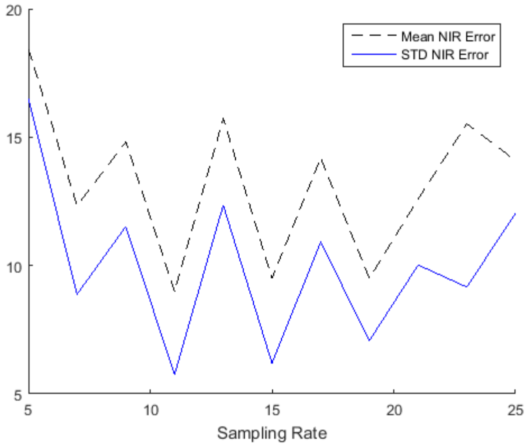

*Figure 39: Mean and STD of NIR error taken over the common range of times used, for image sampling rates of 5 x 5, 7 x 7, 9 x 9 etc. Data for healthy grass with the ASD aimed at 180° East of North, and the camera aimed at 225° East of North.*

*Table 18: Inversion performance comparison when viewing healthy grass with ASD azimuth angle of 180° East of North and camera azimuth of 180° East of North. The definition of error used here is further explained in Table 10.*

| | Mean Visible Error | Mean NIR Error | STD Visible | STD NIR |
|---|---|---|---|---|
| PROSAIL | 0.39% R | 1.36% R | 0.12% R | 1.31% R |
| AMBRALS | 0.83% R | 6.73% R | 0.15% R | 2.31% R |

*Table 19: Inversion performance comparison when viewing healthy grass with ASD azimuth angle of 180° East of North and camera azimuth of 270° East of North. The definition of error used here is further explained in Table 10.*

| | Mean Visible Error | Mean NIR Error | STD Visible | STD NIR |
|---|---|---|---|---|
| PROSAIL | 3.5% R | 15.18% R | 0.2% R | 1.91% R |
| AMBRALS | 5.01% R | 8.65% R | 0.74% R | 2.00% R |

*Table 20: Inversion performance comparison when viewing distressed grass with ASD azimuth angle of 180° East of North and camera azimuth of 135° East of North. The definition of error used here is further explained in Table 10.*

| | Mean Visible Error | Mean NIR Error | STD Visible | STD NIR |
|---|---|---|---|---|
| PROSAIL | 4.02% R | 7.58% R | 0.50% R | 4.94% R |
| AMBRALS | 6.56% R | 7.74% R | 4.56% R | 4.56% R |

AMBRALS in general performed less well than PROSAIL. In some cases there were non-physical results with AMBRALS, where the surface was predicted to have a negative BRDF. AMBRALS did outperform PROSAIL in the NIR with distressed turfgrass, where AMBRALS performs nominally better, and when the healthy grass is viewed with a difference in azimuth angle of 90°. As discussed in the previous section, it is possible that PROSAIL's performance is due to the calibration of its LUTs, and could outperform AMBRALS with additional work.

### 4.2.7 Absolute Calibration Experiment

Two methods were tested for converting the digital numbers found with the camera and the ASD into estimates of reflectance: ratioing the reflectance of a near-Lambertian target and the grass surface, and radiometric calibration of the cameras and ASD. The latter is consistent with what an end user would want to use in the field.

The integrating sphere was used for the radiometric calibration, as it has strong temporal stability, and a known output. This enabled the calibration of both the cameras and the ASD at the same time. To find the irradiance incident on the detector, E', we use the camera equation:

$$E' = \pi L(NA)^2 \tag{44}$$

Where L is the radiance of the sphere, and NA is the numerical aperture of the camera system. A confounding factor in this process is that with a webcamera, elements like the NA of the system may not be known. Thus I sought to develop a calibration that was independent of knowledge of the intrinsic properties of the camera.

There is significant disparity between the spectrum of the sphere and the sun (Figure 40). The camera using one of its filters when illuminated by the sphere produces a DN that we may estimate by summing over the range of wavelengths, λ:

$$DN_{Sphere} = \int_0^\infty L(\lambda)_{Sphere} * R(\lambda)_{Sensor} * T(\lambda)_{system}\, d\lambda \tag{45}$$

Where L(λ) is the spectral radiance on the sensor, R(λ) is the spectral responsivity of the sensor to light, having units of radiance per DN, and T(λ) is the spectral transmission of the camera, which is unitless and accounts for both filter transmission, and system light loss. There will be a similar equation for the response of the camera when illuminated by the sun.

$$DN_{Sun} = \int_0^\infty L(\lambda)_{Sun} * R(\lambda)_{Sensor} * T(\lambda)_{system}\, d\lambda \tag{46}$$

If we take the ratio of the sun and sphere DNs then, we have:

$$\frac{DN_{Sun}}{DN_{Sphere}} = \frac{\int_0^\infty L(\lambda)_{Sun} * R(\lambda)_{Sensor} * T(\lambda)_{system}\, d\lambda}{\int_0^\infty L(\lambda)_{Sphere} * R(\lambda)_{Sensor} * T(\lambda)_{system}\, d\lambda} \qquad \text{Eq (47)}$$

Which I rearrange:

$$DN_{Sun} = DN_{Sphere} \frac{\int_0^\infty L(\lambda)_{Sun} * R(\lambda)_{Sensor} * T(\lambda)_{system}\, d\lambda}{\int_0^\infty L(\lambda)_{Sphere} * R(\lambda)_{Sensor} * T(\lambda)_{system}\, d\lambda} \qquad \text{Eq (48)}$$

For this camera system, the transmission filters will cut off all frequencies above $\lambda_2$ and below $\lambda_1$. If we assume that over this range that response and transmission are approximately constant over the transmitted spectral range, we can simplify Eq (48) by pulling R and T out of the integral and canceling them:

$$DN_{Sun} = DN_{Sphere} \frac{\int_{\lambda 1}^{\lambda 2} L(\lambda)_{Sun}\, d\lambda}{\int_{\lambda 1}^{\lambda 2} L(\lambda)_{Sphere}\, d\lambda} \qquad \text{Eq (49)}$$

The DN here depends on the band being measured. I attempted to absolutely calibrate the camera using the data I had taken, and these equations.

To find the reflectance from an absolute calibration, it was also necessary to estimate the downwelling solar radiation. I found this value using the program SMARTS, downloaded from

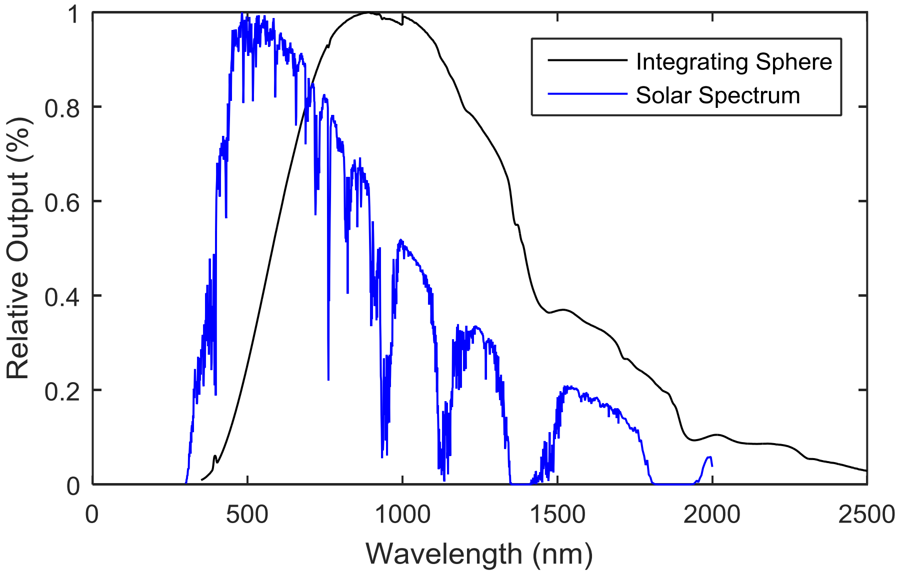

*Figure 40: The peaks for the sphere and the solar spectrum are about 400 nm apart, necessitating a relationship between the DN generated during calibration and the DN generated by the sun.*

the National Renewable Energy Laboratory. SMARTS was designed by C. Gueymard (1995, 2001) to provide estimates of the value for the solar spectrum for various estimates of the atmospheric composition. It was possible to run SMARTS by providing values of the atmospheric composition, such as humidity, which were recorded nearby by both the sensors on the site, and at the university. Values which were unknown could be estimated using an average atmosphere.

The reflectance values produced by this experiment were not of use: The reflectances derived this way were generally far too low, and did not show the distinct increase in NIR reflectivity expected (Figure 13) This latter problem was more significant, since it meant that there was a non-linear error.

Further examination of the problem also undermined the equations used. The approximation that over the range filter transmission, that response and transmission are close to constant, could only be true with two assumptions: 1) the response and transmission stay close to the same value across the range being summed while 2), the range is limited because the transmission or response go to zero. Clearly these both cannot be true, except for a narrow filter with a very sharp cut-on and cut-off. As discussed in section 3.4.6, this is not the case for colored glass filters. It was assumed that even if this did not give a precise radiometric calibration, it would provide an estimate of the quality of this technique, though this does not seem to have been the case.

It is possible there was some bug in the code that prevented this calibration from working, but due to time constraints, this could not be perused more deeply. I consider this a warning that the absolute radiometric calibration of the camera can be more complicated than anticipated. My experience leads me to believe that this is not a good direction of research in particular for the web camera, as trying to absolutely calibrate it further demonstrated that its settings are mysterious and unreliable.

### 4.2.8 Conclusions

The error of the results produced for these measurements was worse than projected. Some measured values for the ASD also seem to not reflect reality well. This seems to be in part be due to the limits of using the digital number ratio to convert to reflectance.

There are two type of error in systems: Consistent offset, as seems to be the case with the data taken, and random variation. If the error is random variation, then the issue is that the system must be redesigned or rethought to work. If the error is an offset by a consistent amount, then calibration of the system can bring the estimated value better in line with the measured values.

Another persistent source of error is the greenness of the grass, which seems to be very high, with a BRF of up to 15%. It is quite possible this originates from the fact that the turfgrass is treated in order to increase its greenness. This may violate the parameters assumed for the PROSAIL program. The PROSAIL program also did not respond well to the distressed grass, never producing a value of reflectance where the green and red have equal reflectance, as we'd expect. This may also be a failing of PROSAIL, where there is an expectation for the vegetation to be healthy. It also seems to be where the AMBRALS model breaks down, so this may not be an uncommon problem in the field, and should be investigated in more detail.

## 4.3 Empirical Line Algorithm

### 4.3.1 Introduction

In this section, I demonstrate how to perform an ELM correction. The data points used for this correction were limited to those gathered for other parts of this experiment. The quality of this correction is thus limited, as in a full scale system there would be additional cameras to have readings taken from all the surfaces at the time of satellite flyover. I make use of a soil target for this example. While this is a surface that neither of my existing BRDF recovery codes is calibrated for, it does provide a necessary bright target for the ELM correction.

To place the effects of the resulting correction in context, I performed a COST correction on the same data set. COST was chosen for this comparison as it is also a simple correction and has been a standard for atmospheric correction when in-situ data is not available (Allan, Hamilton, Hicks, & Brabyn, 2011; De Santis & Chuvieco, 2007; Foody et al., 2001; Islam, Yamaguchi, & Ogawa, 2001; Nguyen, Glenn, Nagler, & Scott, 2015; Rahman, Csaplovics, & Koch, 2005). I compare the resulting ground reflectance and spectral signature separability of the two corrections.

### 4.3.2 Data Set

An area roughly centered on the Karsten Turfgrass Center was selected for this atmospheric correction (Figure 41), as this was where data were taken, and a wide variety of surfaces are available adjacent to the center, ranging from agricultural to urban. The data were offset from Turfgrass Center to reach some areas of interest

Data from the Pleiades-1A satellite was selected for this demonstration. It provided a high enough spatial resolution to contain multiple pixels to sample from the areas measured in the BRF tests. In addition, Pleiades-1A has bands similar to those used by the camera system and Landsat 7 ETM+ and had good temporal crossover with when the readings were taken. The image was taken at an angle of 11.2 degrees, which lowered the uncertainty in the reflectance by being near-nadir.

### 4.3.3 ELM Correction

*Figure 41: A false color map of area used for the example ELM correction.*

To perform an ELM correction, at least two targets are necessary: a light target and a dark target. Moran et al. (2001) showed that it was possible to perform an ELM correction using only a light target, and an estimate of the haze. For this example, to increase the robustness of the ELM correction, I used reflectance estimates of a grass target, a soil target, and an estimate of the haze in the image.

Estimating the reflectance of the grass is a process that I have already explored in depth in section 4.2. Because of the forward scattering bias found in the Teflon target used for estimating reflectance, reflectance values were obtained using readings taken at times when the forward scatter into the camera was at a minimum. Readings were taken of the reflectance of the grass for five days in the week before the satellite overpass. There are stable reflectance estimates in the readings for four of these days with one reading acting as an outlier to all the others. This outlier was discarded, and a spectral reflectance in the direction of the satellite was estimated using an average of the remaining reflectance estimates.

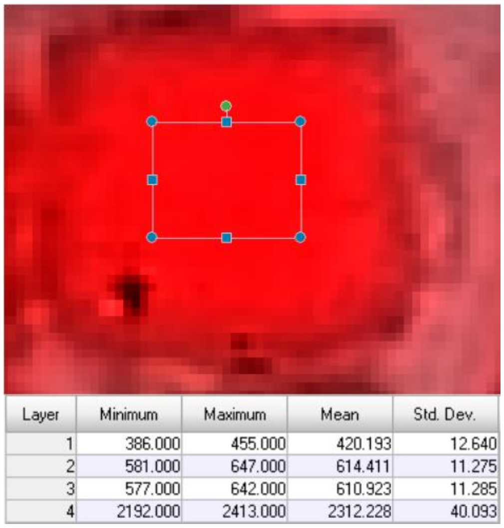

| Layer | Minimum | Maximum | Mean | Std. Dev. |
|---|---|---|---|---|
| 1 | 386.000 | 455.000 | 420.193 | 12.640 |
| 2 | 581.000 | 647.000 | 614.411 | 11.275 |
| 3 | 577.000 | 642.000 | 610.923 | 11.285 |
| 4 | 2192.000 | 2413.000 | 2312.228 | 40.093 |

*Figure 42: False color of turfgrass area used to estimate DN and Reflectance. Layer order is Red, Green, Blue, NIR.*

*Table 21: The estimated reflectance in the direction of the satellite for the four spectral bands, and their mean with outlier 9/24 excluded.*

| | **Sept. 23** | **Sept. 24** | **Sept. 25** | **Sept. 28** | **Sept. 29** | **Mean w/o Sept. 24** |
|---|---|---|---|---|---|---|
| **Blue** | 4.11% | 3.54% | 4.05% | 4.00% | 4.16% | 4.08% |
| **Green** | 11.37% | 18.23% | 10.31% | 13.12% | 11.56% | 11.59% |
| **Red** | 4.81% | 12.16% | 4.48% | 6.40% | 4.91% | 5.15% |
| **NIR** | 75.12% | 65.53% | 69.28% | 75.44% | 71.12% | 72.74% |

The next step in using ELM with the turfgrass was to find the DN associated with it. The reflectance measurements above were made in a variety of locations on a square of turfgrass at the Karsten Turfgrass Center. I took the mean of the DN from this surface for use in the ELM correction (Figure 42)

As a second point for this empirical line, I examine image haze. ELM relies on a bright object and a dark object. In the absence of a dark object, it is possible to use the DN associated with an object of zero reflectance (Moran et al., 2001). However, the selection of a dark object can have significant impacts on the effects of haze (Campbell, 1993) (Figure 43). I used the histogram method of estimating the haze in the image, as this enabled me to find the average darkest pixels across the scene (P. M. Teillet & Fedosejevs, 1995).

Close inspection of the spectral histogram shows that while there is a significant drop off in DN values, there exists a nearly continuous spectrum of DN all the way to zero (Figure 44). The haze in the image must be greater than zero, thus it is necessary to pick a significance threshold for the DN related to haze. P. M. Teillet & Fedosejevs (1995) recommend a threshold of 1000 DN per bin, while Bucher (2004) recommends that we exclude the lowest 0.1% of DN values. As the recommendation by Bucher represents a more general function, I estimated the threshold this created.

To avoid additional processing of the DN associated with the image, I assumed an approximately Gaussian distribution to the DNs. Using the ERF function:

$$ERF(x) = \frac{1}{\sqrt{\pi}} \int_{-x}^{x} e^{-t^2} \, dt \qquad \text{Eq (50)}$$

Which represents the integral over a Gaussian of mean 0 and variance 1/2, it can be shown that excluding the lowest 0.1% of values would place the bin desired to be approximately 3.3σ from the center. Plugging this value in turn into a normal function with σ = 1:

$$f(x) = \frac{1}{\sqrt{2\pi}} e^{-\frac{x^2}{2}} \qquad \text{Eq (51)}$$

It can be shown that at x = 3.3σ the height of the normal function is ~1/234 the height of the peak of the value. Using this relationship as a guideline, I estimated the significance threshold for the four bands using their peak values (Table 22). The cut off frequency for each band is in fact near the 1,000 DN

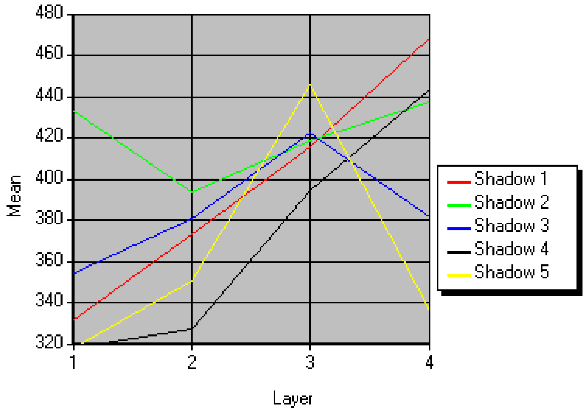

*Figure 43: The mean DN per band for several shadows contained within the scene to be corrected.*

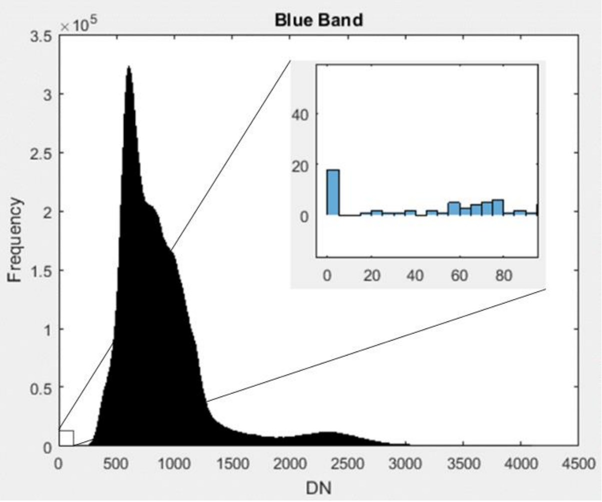

*Figure 44: A hsistogram of the blue values for the example image, demonstrating the significant falloff at around 300 DN, but still near continuous values to zero.*

recommended by P. M. Teillet & Fedosejevss, providing confidence that these are in fact the proper cut off values.

*Table 22: The cut off frequencies estimated for each band found using the 1:234 peak to edge ratio, and the Haze DN estimated by this histogram cut off.*

| **Band** | Blue | Green | Red | NIR |
|---|---|---|---|---|
| **Cut off Frequency** | 1,378 | 1,189 | 927 | 628 |
| **Haze DN** | 265 | 238 | 173 | 213 |

The reflectance of the darkest surface for these darkest pixels was set to 1%, in line with the observation by Moran et al. (2001) that there is rarely a completely black object in the scene.

Soil provided a bright target for the visible spectrum for this ELM correction. BRF readings were taken in the days after the satellite overpass, both on days when the soil was dry and on days when it was wet. As extensive readings were not taken of the soil reflectance at the Karsten Turfgrass Center, and the BRF recovery algorithms were not calibrated to be used with it, some work was necessary to determine the best reflectance estimate.

The measured soil BRF values were then run through both the PROSAIL and AMBRALS code. Experiments were performed to see if altering the range of PROSAIL input values used from the defaults generated for the grass targets would improve the soil recovery estimates. Changing the range of input values for the LUTS generated for the PROSAIL reflectance recovery was found to produce unpredictable results. Additionally, the PROSAIL estimates did not change significantly with the soil moisture, where there was a significant change in soil brightness.

The reflectance estimates created with these new LUTs were compared with ASD readings taken at the same time as the camera measurements. I found a set of PROSAIL input values that reflected the surface properties and produced good estimates of the ground reflectance measured by the ASD. These inputs were then used with the BRF data already measured by the camera to estimate the reflectance in the direction of the satellite sensor. Another estimate of the reflectance in the direction of the satellite was made using the AMBRALS code. There was little agreement between the PROSAIL and AMBRALS values, or between the AMBRALS values for the two days where soil BRF readings were taken (Table 23).

*Table 23: Reflectance estimates in the direction of the satellite for the two days readings were soil take using both PROSAIL and AMBRALS, as well as the reflectance estimate produced by COST for comparison.*

| | PROSAIL (Oct. 3rd) | PROSAIL (Oct. 8th) | AMBRALS (Oct. 3rd) | AMBRALS (Oct. 8th) | Mean | COST Estimate |
|---|---|---|---|---|---|---|
| Blue | 18.76 | 18.76 | 26.37 | 30.3 | 23.54 | 24.4 |
| Green | 21.61 | 21.61 | 30.23 | 32.43 | 26.47 | 26.4 |
| Red | 25.84 | 25.84 | 33.1 | 38.5 | 30.82 | 31.4 |
| NIR | 33.39 | 33.364 | 55.73 | 36.51 | 39.74 | 39.3 |

As these numbers did not generally agree, I compared the numbers produced by AMBRALS and PROSAIL to the reflectance estimates produced by a COST correction to the image (see section 4.3.4). The average spectral difference between the COST corrected reflectance on the soil area and the estimates produced using the BRF data was approximately equal in all cases. PROSAIL had the correct line shape but was consistently below the COST estimates. AMBRALS values were closer to the correct average reflectance but had the wrong line shape. As no one correction stood out as better than another, I took the mean value of the four estimates and found that it produced values within 5% of those of COST. Placing these values into a fit of the data also produced a good fit to the existing values found for the haze and grass, particularly for the green band. Digital numbers for the soil were derived in the same manner as for the turfgrass surface (Figure 45).

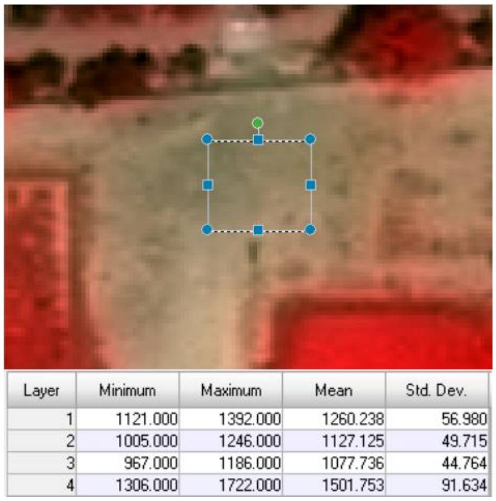

| Layer | Minimum | Maximum | Mean | Std. Dev. |
|---|---|---|---|---|
| 1 | 1121.000 | 1392.000 | 1260.238 | 56.980 |
| 2 | 1005.000 | 1246.000 | 1127.125 | 49.715 |
| 3 | 967.000 | 1186.000 | 1077.736 | 44.764 |
| 4 | 1306.000 | 1722.000 | 1501.753 | 91.634 |

*Figure 45: False color of soil area used to estimate DN and Reflectance. Layer order is Red, Green, Blue, NIR.*

Having derived digital numbers and reflectance values for the two surfaces and the haze, it was then possible to perform a linear fit to the data, finding the slope, *a*, and intercept, *b*, relating the reflectance, R, to the DN (Figure 46).

$$R = a * DN + b \qquad \text{Eq (52)}$$

### 4.3.4 Cost Correction

A COST correction was also performed on the image to compare the results to the quality of the ELM correction performed for the previous section. COST was chosen for this comparison since it is a simple correction and a standard for professionals .

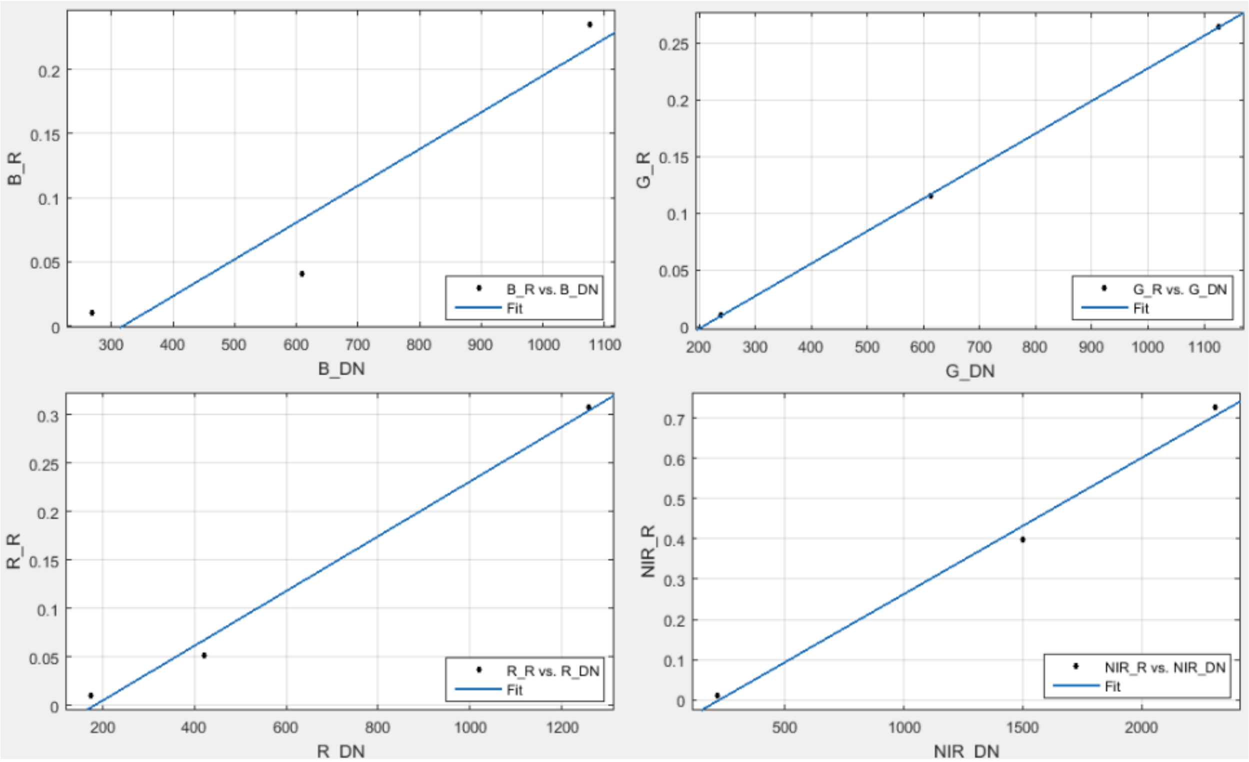

*Figure 46: Fits relating the DN to Reflectance values for the four spectral bands using the data derived above.*

The COST algorithm was developed by Chavez as a means of providing a cost-effective atmospheric correction when in-situ readings are not available (Chavez, 1996). This would provide a means of radiometrically correcting remotely sensed data where it is impossible to take in-situ readings, such as historic data. COST was an improvement on the Dark Object Subtraction (DOS) algorithm. While DOS accounts for the additive effects of haze in an image, COST also takes into account the multiplicative effects of atmospheric transmission.

Both COST and DOS are built off the following equation relating the surface reflectance, R, to atmospheric and radiometric properties:

$$R = \frac{\pi(L_{sat} - L_{haze})}{\tau_v * (E_0 * Cos(\theta_z) * \tau_z + E_{down})} \qquad \text{Eq (53)}$$

Where $L_{sat}$ is the radiance in measured by the satellite, and $L_{haze}$ is the radiance scattered by the atmosphere in the direction of the satellite. $\tau_v$ and $\tau_z$ are respectively the atmospheric transmittances from the ground to the sensor, and from the top of the atmosphere to the ground. $E_o$ is the solar spectral irradiance at the top of the atmosphere for the day when the readings were taken. $\theta_z$ is the zenith angle of the sun, and thus $Cos(\theta_z)$ accounts for the ground angle with respect to a plane normal to the sun's irradiance. $E_{down}$ is the downwelling irradiance due to atmospheric scattering.

To derive the reflectance of the surface from the DN found by the satellite, we must first transform the DN measured into an estimate of the radiance on the sensor, $L_{sat}$, using the gain and bias of the sensor. These variables are measured via onboard calibration units and by vicarious calibration. This equation is most often written:

$$L = DN * Gain - Bias \qquad \text{Eq (54)}$$

Though there are also instances of other definitions (ASTRIUM, 2012; Chavez, 1996). The correct equation to use is the one defined for the satellite data available.

The COST algorithm is a simplification of Eq (53), designed to use only the image data and metadata, without in-situ readings. $L_{sat}$, $E_o$, and $\theta_z$ will all be known, and $L_{haze}$ can be derived from the image itself. This can be found using Eq (54) and by finding the DN associated with the haze, as is explained in Section 4.3.3. This leaves to be found values for the variables $E_{down}$, $\tau_v$, and $\tau_z$.

To remove $E_{down}$ from the equation, Chavez estimates it to be 0. $\tau_v$ and $\tau_z$ are more difficult to find, with

$$\tau_v = exp(-t * sec(\theta_v)) \qquad \text{Eq (55)}$$

$$\tau_z = exp(-t * sec(\theta_z)) \qquad \text{Eq (56)}$$

Where *t* is the optical thickness of the atmosphere and $\theta_v$ and $\theta_z$ are the view angle of the sensor and sun zenith angles. If we were then to set $\tau_v$ and $\tau_z$ equal to 1, this would be Dark Object Subtraction. Instead, Chavez makes the empirical observation that $\tau_z$ is often very close in value to $\cos(\theta_z)$. Similarly, $\theta_v$ can be approximated with $\cos(\theta_v)$. This enables finding the surface reflectance without an estimate of the atmospheric thickness, giving us the equation:

$$R = \frac{\pi(L_{sat} - L_{haze})}{(E_0 * Cos^2(\theta_z) * Cos(\theta_v))} \qquad \text{Eq (57)}$$

Chavez further modifies this equation by setting $\cos(\theta_v) = 1$, which is true for cases where we are viewing the scene from at nadir. As this is not the case for the data gathered using the Pleiades satellite, I do not make this approximation.

### 4.3.5 Comparison of Reflectance Statistics

A comparison of the images produced by the COST and ELM corrections shows that while they produce similar values, the ELM correction has higher reflectance values across the image in the green and NIR, with more similar reflectances to COST in the blue and red. The range of reflectance values is also larger in the ELM image than in the COST image (Table 24)

*Table 24: The mean and standard deviation of the four bands of the COST corrected and ELM corrected image.*

| | Blue | Green | Red | NIR |
|---|---|---|---|---|
| $\mu_{ELM}$ | **16.57** | **19.40** | **19.64** | **34.80** |
| $\mu_{COST}$ | **16.97** | **17.60** | **19.85** | **30.30** |
| $\sigma_{ELM}$ | **12.06** | **12.81** | **13.71** | **17.17** |
| $\sigma_{COST}$ | **11.27** | **12.22** | **13.74** | **14.65** |

ELM correction differs most from the COST correction in the blue band for bright targets. In the green and NIR it differs for bright targets and to a lesser extent vegetation. The red behaves in the opposite manner and has stronger reflectance for COST than ELM in areas that would typically be dark in both images: roads, grass, etc. (Figure 48).

The ELM and COST corrections are very similar for the red band. The difference between the two corrections less than 0.3% reflectance (Figure 47). For the green band, ELM produces values of reflectance that are consistently above those produced by the COST correction. This is an unexpected result since the fit for the green band for the ELM correction is one the closest produced (Figure 46) and two of the points in that fit, the haze DN and the soil reflectance, are shared with those in the COST correction. The ELM blue band finds values of reflectance both above and below those produced by COST in different areas. This implies that there is a difference in both the offset and slope between the ELM and COST corrections. Finally, in the NIR band, we see the largest scale and range of difference values between ELM and COST, and the majority of these differences are ELM estimating a reflectance higher than that of COST. The NIR will generally produce the largest differences, being frequently the most reflective of the bands.

COST and ELM in this correction have produced significantly different numbers, despite sharing the same dark value, and nearly the same values for the soil reflectance. The average reflectance values for the ELM correction are higher than the average values for the COST correction. In addition, the reflectances are spread over a larger range for the ELM correction.

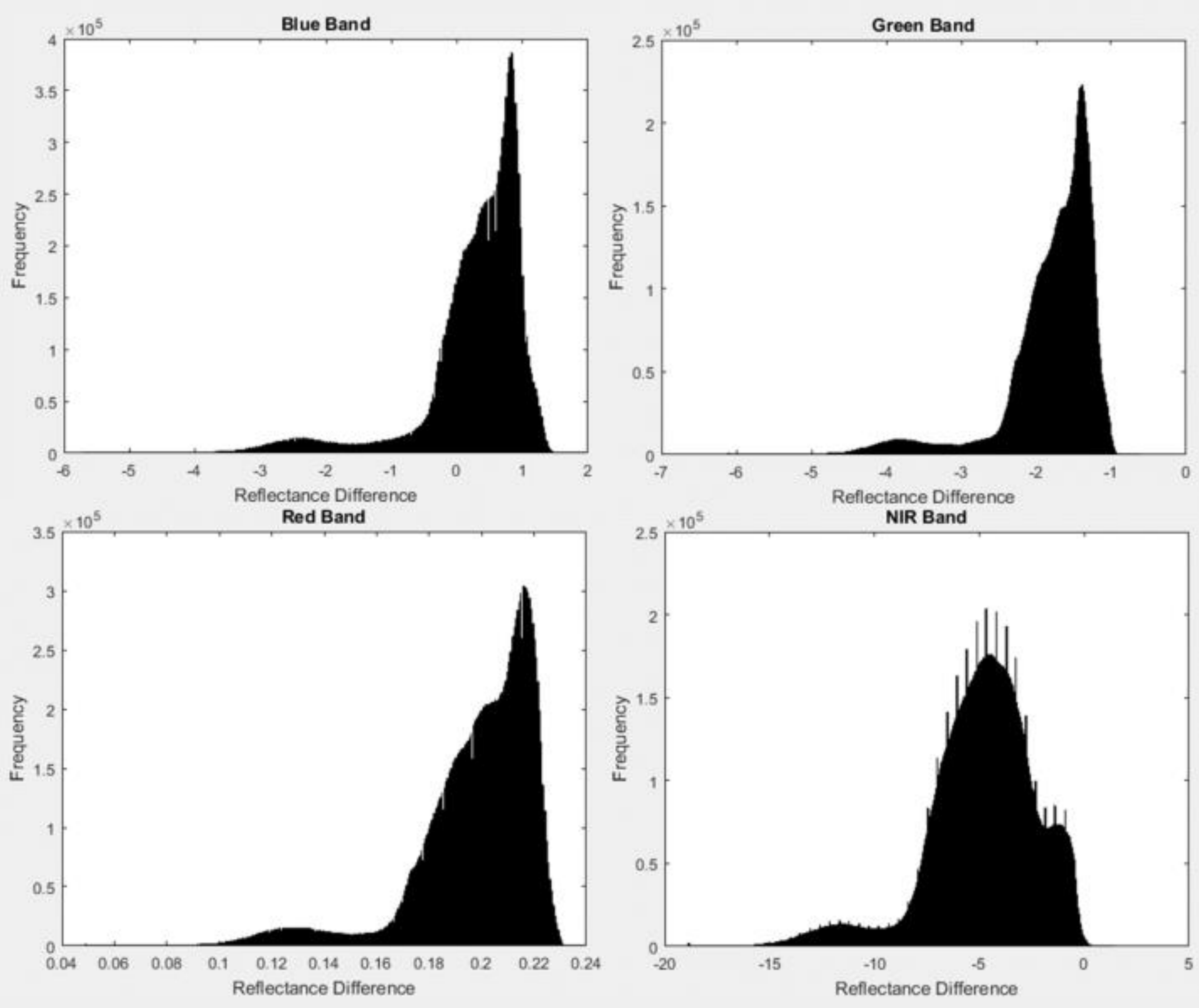

*Figure 47: Histograms of the difference images produced by subtracting the ELM correction from the COST correction.*

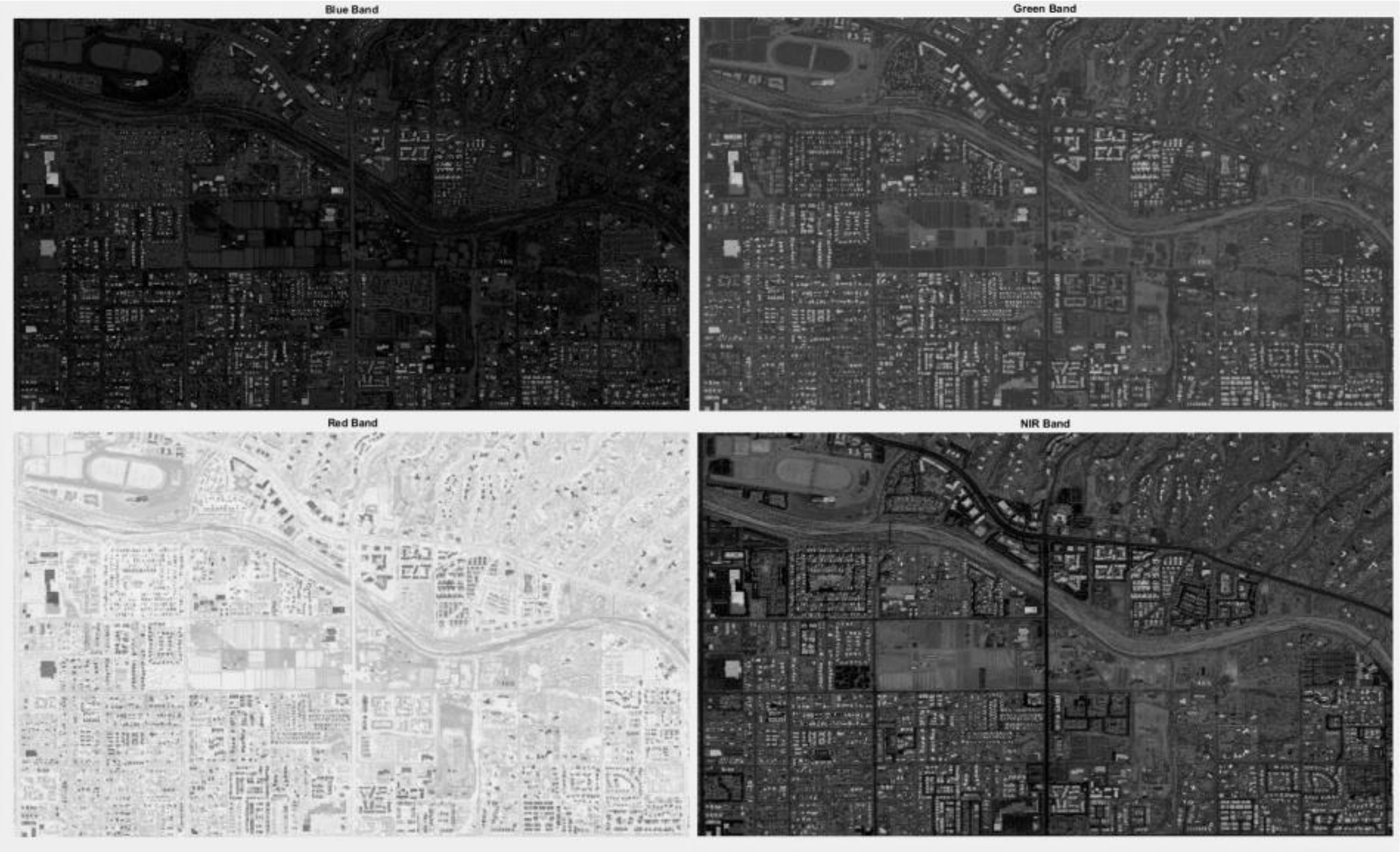

*Figure 48: Difference images for the four spectral bands created for the COST and ELM corrections. White represents the maximum absolute difference between the two images for that band, while black represents areas where there is no difference.*

### 4.3.6 Spectral Signature Separability

The spectral signature separability is used to estimate the difficulty differentiating between two spectral signatures. I examine two different measures of signature separability: The Euclidean distance, which represents a linear distance between the two signatures, and the divergence, which represents how a well a maximum likelihood classification could differentiate between the signatures. To examine the signature separability differences in the context of these images, I selected four surfaces for three different surface types (Table 25)

*Table 25: Surfaces used for measuring the spectral signature separability, grouped into surface type.*

| Vegetation | Soil | Urban |
|---|---|---|
| Turfgrass | Soil | Gravel |
| Field Grass | Sand | Parking Lot |
| Crops | Plowed Dirt | Bright Roof |
| Trees | Scrubby Desert | Dark Roof |

Surfaces that would be difficult to differentiate spectrally were preferred. As an example, I compared the signatures of heavily maintained turfgrass of the Karsten Turfgrass center and of several fields of grass used as soccer fields and school play areas.

Example areas were selected for each surface arbitrarily. The separability statistics for the surface types were computed by taking the average separability of every combination of surfaces within the surface type. For all three surface types in this example, ELM's Euclidean distance was larger than COST's, while COST's divergence was stronger than ELM's. While ELM's results have a wider spectral spread than COST, there is also a blurring of the classes. The peaks of the signatures are further apart for ELM, but the signatures are also wider and become wider faster than they move apart. This happens with all three surface types: For vegetation, where the spectral distances are low, to urban, where the spectral distance is fairly large. The superior correction for performing a classification will depend on the decision rule selected for the image classification process.

*Table 26: A comparison of the spectral separability of the ELM and COST corrections performed on the data set.*

| | **Vegetation** | | **Soil** | | **Urban** | |
|---|---|---|---|---|---|---|
| | ELM | COST | ELM | COST | ELM | COST |
| **Euclidean Distance** | 15.22 | 13.08 | 19.4712 | 17.93 | 75.5361 | 69.96 |
| **Divergence** | 20.47 | 38.74 | 71.5133 | 90.44 | 601.1 | 672.80 |

### 4.3.7 Conclusions

The ELM correction gives answers that are similar to the COST algorithm, both in terms of the raw statistics, and in the potential performance of classification of the image. It is impossible to say which correction is more accurate without additional spectral ground data taken at the time of satellite flyover. Though differences exist between the corrections, these results indicate that even for ground data of limited accuracy that it is possible to do an accurate correction using ELM. In the next section I confirm this through simulation.

## 4.4 Atmospheric Simulation

### 4.4.1 Introduction

To further relate the research in this paper on camera systems to their purpose on improving remotely sensed images, in this section I simulate the effect of using noisy data to performing an ELM correction on a real image. In the previous section, I explored how to use my own data to perform an ELM correction. In section 3.3.2, I simulated the effects of creating an empirical line using noisy data, to measure how far an empirical line created with noisy data would be from the true line. Here I use simulated readings from Landsat 8 OLI data, forcing the simulated ELM correction to be performed on sites that can be found within the image, rather than ideal ones. This clarifies the quantity and types of sites that would be most important within a full-scale system.

### 4.4.2 Data Set

I used Landsat 8 OLI data of Tucson and the surrounding area for this simulation, limiting the area to a square 60 km around the center of Tucson (Figure 49). Landsat 8 OLI data were a natural choice for this experiment, as the full-scale camera system is intended for use with Landsat 7 ETM+, Landsat 8 OLI, or similar satellites-borne sensors. Using a 60 km square enabled me to examine a large number of pixels while retaining a reasonable simulation time.

Two clear days were selected for use: July 1st, 2015, and August 4th, 2015. Clear days were preferred to ensure that poor numbers were not the result of only selecting calibration sites that happened to have increased haze. Using more than one day provided assurance that the results would not be unique to that day. Landsat 8 OLI data within this date range provided both uncorrected and atmospherically corrected data of the same area.

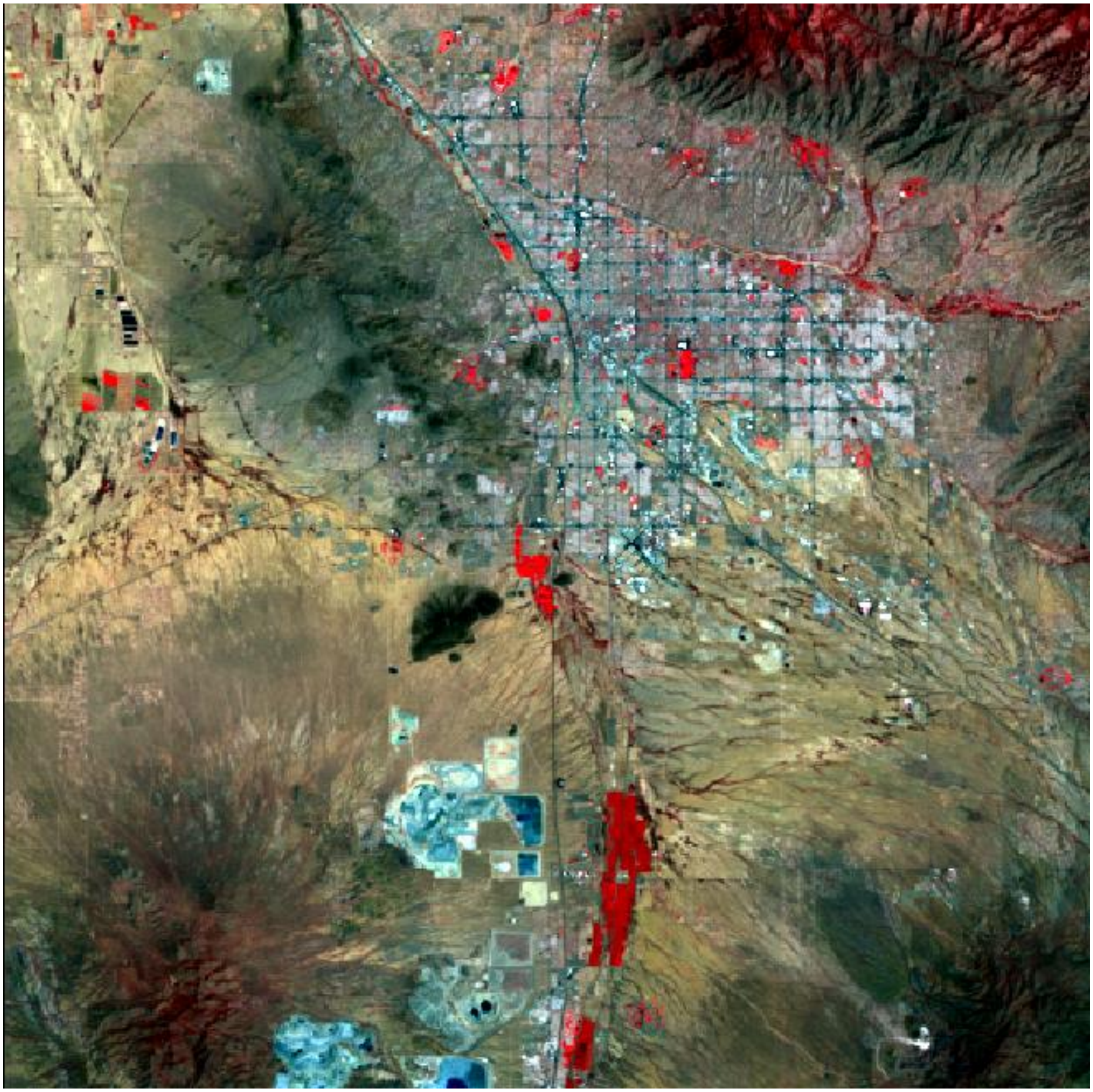

*Figure 49: False color image of the area of Tucson used for the ELM simulation.*

### 4.4.3 Methods

For an empirical line correction, both the surface reflectance and top of atmosphere (TOA) digital number for some pixels must be known. For this simulation, I used numbers provided by the TOA and surface reflectance products available for Landsat 8 OLI data. Calibration targets were selected from four categories: water, vegetation, soil and bright roofs (such as for a large mall). Single pixels were selected to represent each site to better simulate what would be possible to measure using a single camera site. All targets were selected to provide at least 9 surrounding pixels of the same class. This was necessary as in a full-scale system, a large target is necessary to ensure that the 30 m Landsat pixel and the area measured cross over without spectral mixing. Pixels were selected from the same area for both images when possible. As the data taken in June and August showed different phenology, different vegetation areas were sometimes assessed for each date.

The simulation of ELM took as inputs the number of each site category to be used in the correction, and the average error of any estimate of the reflectance to be assigned to the measurements. Example sites within the class were selected at random and then assigned reflectance values based on the Landsat surface reflectance product. The reflectance from the Landsat surface product for each band of each site was independently modified by adding a value from a normal function with 0 mean and standard deviation equal to the error entered at the start. These modified reflectance values and a haze value generated as in section 4.3.3 were used to compute lines for each band relating DN to reflectance for each of the four bands.

This ELM correction was then applied to the TOA image, changing it to a reflectance image. The values for this ELM corrected reflectance image were subtracted from the Landsat surface reflectance product for the same area, producing a difference image. The mean and RMS difference were calculated from this image, and treated as the RMS error in the simulated  This process was repeated 200 times for the number of water, vegetation, soil and bright roofs sites and the error value selected, to find an average value independent of the individual sites picked in each pass of the simulation (Figure 50).

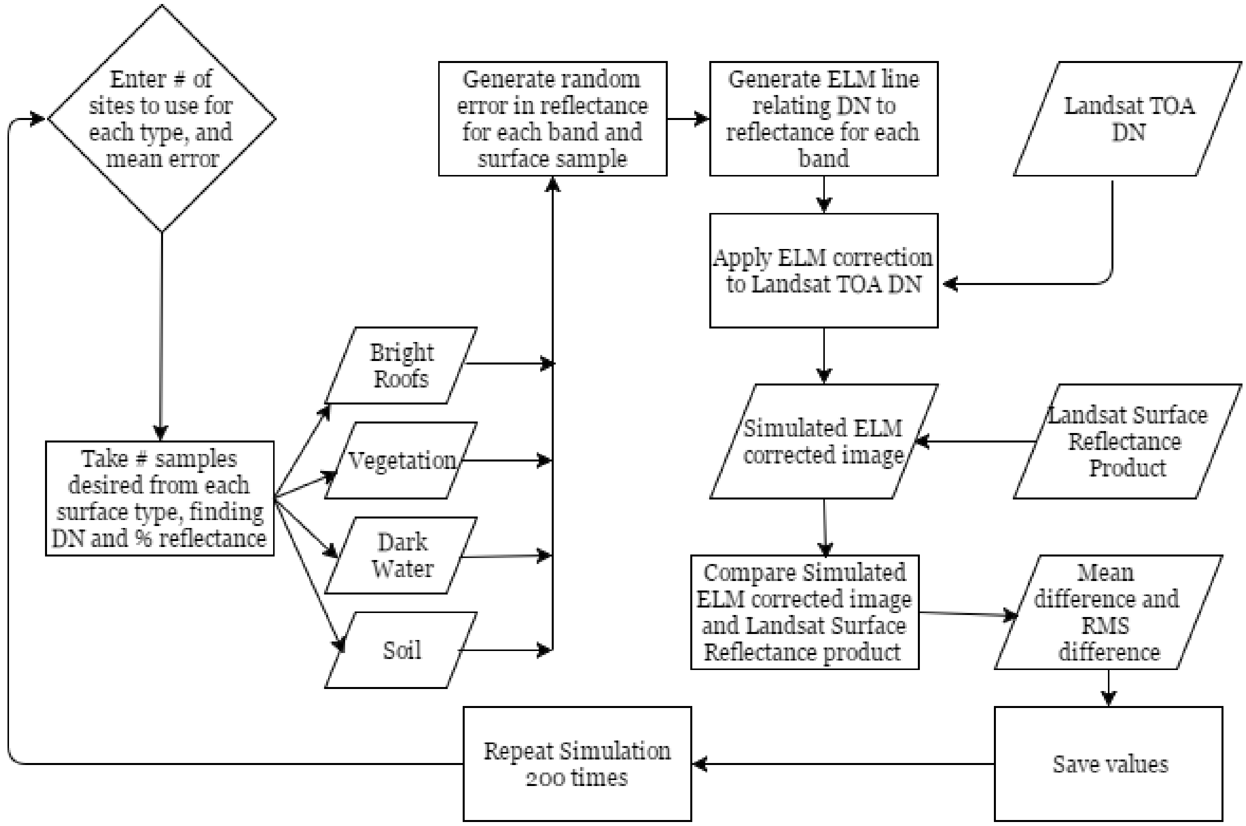

*Figure 50: Flow chart of ELM simulation.*

### 4.4.4 Comparative Setups

I examined both the average and RMS error between the images. The average error between the two images in the visible tended to be substantially lower than the RMS error, showing that the ELM correction provided values both above and below that of the Landsat surface reflectance product. I use the RMS error value for the rest of this analysis to represent the maximum error. The errors produced by the two dates were also considerably different. The error in the visible bands for the data taken on August 4th was significantly higher than the error present in the data for July 1st, with the opposite was true in the NIR. I use the average RMS error of these two dates for the rest of the analysis of this simulation.

I began by analyzing the simulation in situations where no error was introduced into the reflectance readings in order to understand the baseline performance of the ELM correction. I found there was an inherent amount of error between the image produced by ELM and the Landsat surface reflectance product and the amount of error between the images depended strongly on the surfaces used for the correction. Each surface type provided a different amount of correction to the TOA DN image. Examining how each surface corrects these data on its own, using the haze as a dark point, we can see that the soil provides the best correction on its own, followed by the bright roof and then vegetation. The dark water provides the worst correction on its own by a large margin (Figure 51). This is expected, as a correction with two dark targets will have large changes in the slope of the empirical line for small changes in the DN or reflectance estimate. The vegetation is unique in providing a better correction in the NIR than in the visible spectrum, which is consistent with the above observation and with it being much less reflective in the visible.

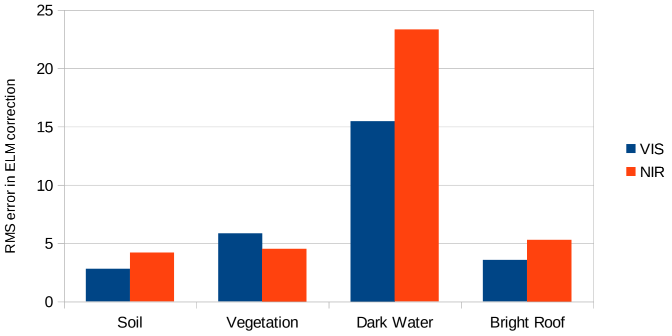

*Figure 51: RMS error in the ELM correction when performed using only the using only the surface type listed, and the haze values.*

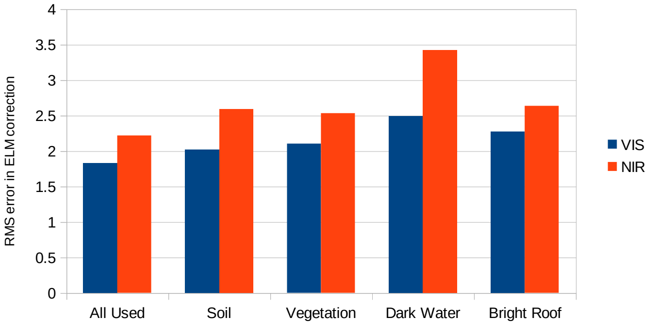

*Figure 52: RMS error in the ELM correction when all surfaces are used, and when the surface listed is removed from the correction.*

For a comparison, I instead starting with an ELM correction performed using one of each surface type, and removing one at a time from the correction. Each surface type when removed produced a similar amount of error when removed from the correction (Figure 52). Removing the soil or the vegetation target worsens the image by a similar amount, with the bright roof providing a slightly larger change. The largest change comes from removing the dark water, showing its importance, even if it does not provide the best correction on its own.

The error between the two images can be further decreased by increasing the number of sites used (Figure 53). There does appear to be an upper limit to the amount of correction that is possible, at around an RMS error in reflectance measurements of 1.5%. Increasing the number of soil targets appears to be more helpful to the correction than increasing the number of vegetation targets, but both improve the correction.

Next I tried introducing error into the system, to see its effect on the quality of the recovered correction. The correction is surprisingly resilient as error in the measured reflectance is increased, provided there are enough samples to begin with (Figure 54). With just four sites, one of each surface class, there is a change in the RMS error in the ELM correction of 0.5% reflectance, for a change in the mean error in surface reflectance from 0% to 5% reflectance. With more sites, there is a similar change in the RMS error in the correction, though they begin with a smaller values.  This result is consistent with the expectation from section 3.3.2's simulation, that as the quality of the measurements decreases the resulting atmospheric correction can be improved by increasing the number of sites monitored.

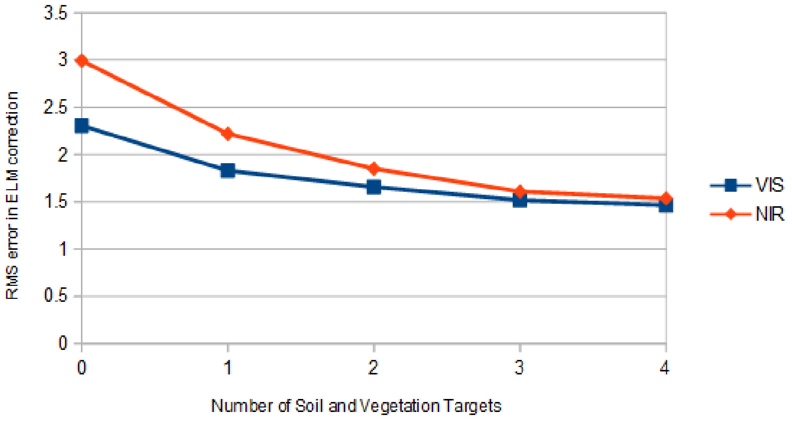

*Figure 53: RMS error in the ELM correction when the number of dark and bright targets are held constant at one, and the number of vegetation and soil targets are increased.*

### 4.4.5 Discussion

This simulation shows that it is possible to create a good atmospheric correction using a number of surface reflectance estimates and that the quantity of estimates is far more significant than the quality of the estimates. Introducing noise to the reflectance estimates does impact the resulting atmospheric correction, but only by a fraction of a percent of the reflectance measured. This is promising for the use of

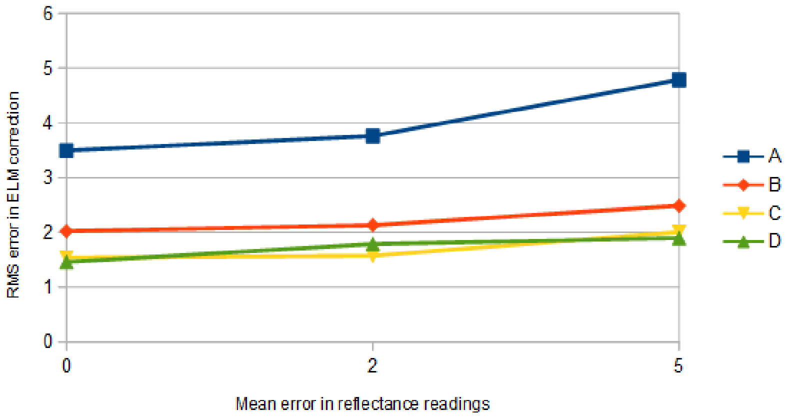

*Figure 54: RMS error for the combined bands in the ELM correction. The error in the measured reflectance readings is increased for an ELM correction performed using A) a single soil target, B) One bright roof, dark water, soil and vegetation target, C) One bright roof and dark water target, with four vegetation and three soil, D) One bright roof and dark water target, with seven vegetation and three soil.*

cameras in estimating reflectance, as it shows that exacting measurements of the surface reflectance are unnecessary. This simulation also demonstrates the need to begin an investigation the potential for cameras to measure the reflectance of new surfaces with different reflectances such as water and bright roofs.

# 5 Conclusions

## 5.1 Conclusion

For this dissertation, I have explored the process for designing, calibrating and testing a BRF camera system. My goal in this has been to take existing work on empirical atmospheric correction, vegetation BRF and in-situ cameras, and expand their range and overlap. I take cameras and techniques are being used in labs and move them into the field. I use of work on vegetation BRF and modify it to be used with a camera system, rather than a single pixel hyperspectral sensor. I seek to take the empirical line method of atmospheric correction and move it from a niche process for a limited amount of high precision results to one where it can be automated.

I examined the process of building the camera system both in simulation and practice. My initial modeling of the empirical line method showed that an estimate the directional reflectance of a surface within 2% reflectance was required to perform ELM with a reasonable number of sites and cameras. Using this specification, I explain the methods of system design, and selecting parts based off that design that enable meeting this specification, providing lists of my specifications and selected components. I find in the process of that much of the error inherent in the system comes from the calibration and set-up of the camera system in the field. I have listed ways to calibrate the system, with some focus on finding the azimuth and zenith angles of a camera system crossing multiple coordinate systems.

Experiments with the camera system demonstrate its strengths and limitations. I found that the Teflon block used for the digital number to reflectance conversion had significant specular reflection, which undermined finding the absolute error of the system. Specular reflection contributed a change of 9.2% reflectance for the NIR band, with a mean of change 1.6% for the visible bands. Despite being unable to evaluate the absolute error of the system, there was an opportunity to learn more about the relative limits of the system. In the process, I discovered aspects that may negatively impact performance. In the design phase, the read noise and filter choice were the strongest influences on the quality of the final product. The calibration demonstrated the problems of pixel to angle calibration, and adapting the web camera for scientific work, both physically, and with its software. In the experimental phase, I discovered the importance of the dynamic range of the camera. This was not an element that I had included in the simulations, but processing of the web camera data demonstrated that a narrow dynamic range can impact system error by limiting the range of reflectances that can be measured at the same time. I also learned more of the limits of the PROSAIL and AMBRALS inversions. The PROSAIL inversion needs additional research into the range of parameters to use, while the AMBRALS inversion showed unexpectedly poor performance, with non-physical reflectances in some cases. The experimental results points toward the potential for a full scale system performing within the specifications required for ELM. Before a full scale system can be implemented, more work will have to be done on the absolute calibration.

Performing an ELM correction with the data available and comparing it with a COST correction demonstrated that an ELM correction performed with even limited data provides a correction comparable to an established correction. The project ended by returning to simulations of the effects of ELM correction on the atmosphere, to understand what the limits of the camera system's utility in the field using available sites. The results indicate it would take fewer cameras than expected to do this form of correction than expected, but that a larger diversity of sites would be desirable.

## 5.2 Intellectual Merit

The atmosphere degrades the quality of remotely sensed data gathered by satellite-borne sensors. The atmospheric correction for these data will influence quality of data available to all lines of remote sensing. As such, it is important to understand as much as possible about atmospheric correction. My research seeks to provide a path to learning more about the quality of atmospheric correction.

The full scale camera system will need sites to use as ground targets. Fortunately, many long-term research projects already maintain and monitor sites. Cameras could be set up at these sites and contribute both direct monitoring and corrected remotely sensed data, providing the researchers maintain the land with additional sources of information. Possible existing research sites include the Long Term Environmental Research (LTER) network sites (Knapp et al., 2012), those used by SpecNet (Gamon et al., 2006) or AmeriFlux (Law, 2007), or temporary sites, such as those used by the WiSARD Network (Yang et al., 2005). This work could also be paired with other existing camera networks like AMOS (“AMOS | Project Overview,” 2013) and Camnet (“Camnet,” 2012) or phenological cameras (Richardson et al., 2009 ; Benton et al., 2008). While not originally an intent of this research, the current implementation of the PROSAIL BRF inversion produces measurements of vegetation quality. This would enable the camera system to be of use to and potentially pair up with non-scientific ventures, such as park and golf course management, or farming.

My camera system would complement research on methods of atmospheric correction using both radiative transfer codes and empirical ground reflectance data. These hybrid methods have been suggested (Gao et al., 2009; Clark et al., 1995), but not pursued deeply. This is likely due to the current high costs in time and resources of gathering ground reflectance data. By gathering ground reflectance data over long periods, my camera system could lower these costs, and promote more research into means of improving atmospheric correction.

My camera system will reduce the work needed for atmospheric correction. It could be used with ELM, a straightforward correction requiring only basic math once ground spectral data is available. For researchers interested in using remotely sensed data, but not well versed in atmospheric correction algorithms, my camera system and ELM could provide easy access to well-corrected data. If ELM is not used, and the camera is instead used in a validation capacity, having ground spectral data will still decrease the effort verifying that an atmospheric correction is accurate. In addition, the camera system will not need experts to set up or maintain, enabling it to be shipped to distant places. Low cost ground data could complement the expanding field of low cost satellites (Bouwmeester & Guo, 2010; Salas et al., 2014; Woellert et al., 2011).

## 5.3 Broader Impacts and Future Work

This system is expected to simplify atmospheric correction, improving the quality of remote sensing. It may be of significant use to goniometry, by further demonstrating a method of taking readings from multiple angles at the same time in the field. Similarly, work done characterizing turfgrass will complement BRF research. The camera system may aid in the vicarious calibration of satellite-borne sensors, which needs both high quality atmospheric correction, and spectral monitoring of sites (S. F. Biggar et al., 2003). My simulations of ELM seem to point to a larger trend in atmospheric correction: that a very large number of poor estimates of pixel value can lead to an adequate overall correction. There are a very large number of methods of atmospheric correction, and this may be worth investigating further as a unifying principle.

The system should assist in networking remote sensing with other monitoring networks and the broader community. Remote sensing can currently be done largely with little or no interaction with the non-scientific community. If a camera is located on land not owned by the university or NASA or a similar agency, it necessitates some level of interaction with the non-scientific community. If a camera system were to be placed in a public place such a large school field, it would be an opportunity for engaging citizen scientists and marketing remote sensing, a somewhat hidden field, to the next generation of engineers.

Several areas of this dissertation merit further research. The absolute error for the camera system could be more thoroughly investigated by conducting tests using a more lambertian reference target during a period with fewer cloudy days. Additional BRF recovery testing could be performed using soil as a target, and an appropriate model and method of BRF recovery found. As the final simulations of ELM demonstrated the value of using surfaces beyond soil and vegetation, these surfaces should also be investigated for their BRF recovery potential. Absolute calibration of the camera, while a known process, should also be explored as should the stability of its calibration in the field, as it is a necessary step for outdoor use. Finally, additional BRF recovery methods, such as curve fitting, could be explored.

# Appendix A

## PROSAIL Code Improvements

### PROSAIL Run Speed

PROSAIL's run time determined much of the analysis that I was able to do for this dissertation. It affected both the number of simulations I could do to test the system and the number of LUTs I would be able to generate for the final analysis. As such, it was imperative that I get it to run as fast as possible, if I could.

I ran Matlab's built in runtime tool to better understand the sections of the PROSAIL code that were called the most often and took the longest. Fortunately, I found that the majority of the run time was actually tied up in one subroutine, tav.m. After examining this code, I found that it took in a single input angle, and a large string of preloaded constants that did not change with the input values to PROSAIL. It then ran extensive and time consuming calculations on these before returning a single value.

Since this calculation was so frequently repeated and had a single varying input, it was apparent that I could calculate these values once, and then implement a look-up table solution for the values of tav.m. This limited the resolution of the values produced, but if a sufficiently large number of input

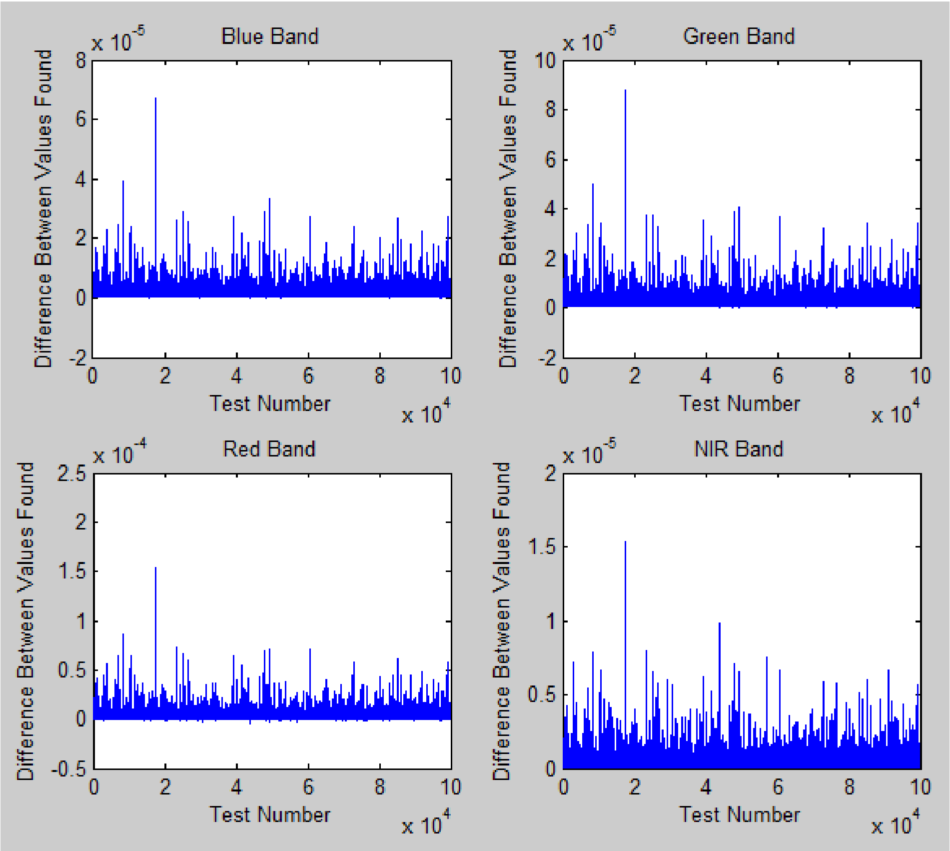

*Figure 55: Absolute difference between the reflectance bands found for 10,000 randomly generated sets of PROSAIL input values, run with the modified and original tav.m code.*

angles were used, this effect could be mitigated. Since this is a program that is run very frequently, running it enough to generate a fine resolution look-up table could be justified.

In my initial experiment with this, I generated 1,000 input values for theta between 0 and 90° to generate the look-up table for tav.m. I then took a copy PROSAIL with the tav.m look-up solution, and the original PROSAIL code, and generated random values for the input to place in them. By running both versions of PROSAIL with these random inputs, I could compare their outputs to see if using the look-up table solution for finding the values of tav.m had a significant effect on the output of the PROSAIL program. After running 10,000 of these simulations, I found that they only changed the values of reflectance bands by 0.01% (Figure 55) in a few cases. Further investigation of these instances demonstrated that these examples only happened when the input and output angles of reflectance were over 89°. Since this is outside the range of inputs that I intended to use, I decided that this was good enough for the program I was running, and should be good enough in most other instances as well. The mean run time difference for the PROSAIL runs with the modified code was 36.9% of that of the PROSAIL code running the original tav.m (Figure 56)

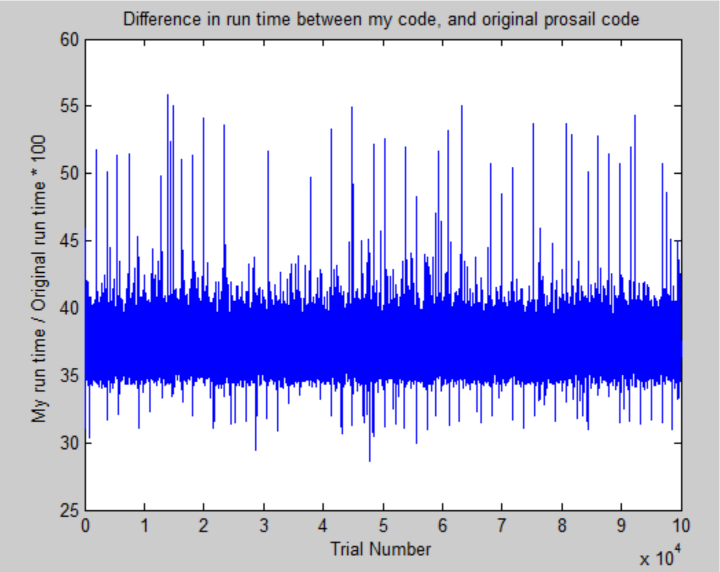

*Figure 56: % Difference in run time for the original tav.m code, and my modified version, for 10,000 runs with randomly generated inputs.*

### PROSAIL LUT Search Algorithm

For the PROSAIL LUT inversion, it is necessary to sort the example BRFs generated to find those that are closest to measured reflectance data. The comparison between the measured reflectance BRF, and the BRF generated by PROSAIL is fixed. Thus, any speed gain to be done here is to be done by improving upon the sorting algorithm. There are a number of sorting algorithms, each with their own merits. For the PROSAIL inversion, I selected the Insertion Sort algorithm.

Insertion sort is one of the simplest sorting algorithms. Insertion sort works by comparing an item $i_n$ with the one immediately before it $i_{n-1}$, according to a metric. If the metric is higher for $i_n$ than it is for $i_{n-1}$, then the items are switched. Insertion sort repeats this swapping until $i_n$ either reaches the top of the list or it encounters an item with a higher metric. By applying this algorithm to each item in the list from top to bottom, the items can be sorted according to the metric. This metric could be an alphabetical order, or as in this case, a measure of how close two BRF functions are to each other.

Insertion sort is not the fastest algorithm if it is used on a random set of data However, the analysis for this project often involved running repeated searches through the same set of examples BRFs with slightly different inputs. Insertion sort is one of the fastest search algorithms when working on nearly sorted data. By keeping a list of the BRFs that had been closest to the reference BRF input to the LUT inversion, it was possible to take advantage of this feature. This meant that the analysis would run slowly the first time, but quickly for any subsequent analysis. For future research, a camera with a pseudo-invariant field of view could make use of this technique to speed the analysis between days of data.

# Bibliography

Ahern, F. J., Goodenough, D. G., Jain, S. C., & Rao, V. R. (1977). Landsat atmospheric corrections at CCRS. In *Proceedings of the 4th Canadian Symposium on Remote Sensing* (pp. 583–595).

Allan, M. G., Hamilton, D. P., Hicks, B. J., & Brabyn, L. (2011). Landsat remote sensing of chlorophyll a concentrations in central North Island lakes of New Zealand. *International Journal of Remote Sensing*, *32*(7), 2037–2055. http://doi.org/10.1080/01431161003645840

AMOS | Project Overview. (2013). Retrieved October 7, 2013, from http://amosweb.cse.wustl.edu/

Anderson, K., Dungan, J. L., & MacArthur, a. (2011). On the reproducibility of field-measured reflectance factors in the context of vegetation studies. *Remote Sensing of Environment*, *115*(8), 1893–1905. http://doi.org/10.1016/j.rse.2011.03.012

Anderson, K., & Milton, E. J. (2006). On the temporal stability of ground calibration targets: implications for the reproducibility of remote sensing methodologies. *International Journal of Remote Sensing*, *27*(16), 3365–3374. http://doi.org/10.1080/01431160500444780

Anderson, N., Czapla-Myers, J., Leisso, N., Biggar, S., Burkhart, C., Kingston, R., & Thome, K. (2013). Design and calibration of field deployable ground-viewing radiometers. *Applied Optics*, *52*(2), 231–40. Retrieved from http://www.ncbi.nlm.nih.gov/pubmed/23314640

Anderson, N., Thome, K., Biggar, S., & Czapla-Myers, J. S. (2008). Design and Validation of a Transfer Radiometer. In J. J. Butler & J. Xiong (Eds.), *Proc. SPIE 7081, Earth Observing Systems XIII* (Vol. 7081, pp. 708104-708104–8). http://doi.org/10.1117/12.795478

Angal, A., Chander, G., Xiong, X., Choi, T., & Wu, A. (2011). Characterization of the Sonoran desert as a radiometric calibration target for Earth observing sensors. *Journal of Applied Remote Sensing*, *5*(1), 59502. http://doi.org/10.1117/1.3613963

ASTRIUM. (2012). *Pléiades Imagery User Guide*. Retrieved from http://blackbridge.com/geomatics/upload/airbus/Pleiades User Guide.pdf

Atkinson, G. a., & Hancock, E. R. (2008). Two-dimensional BRDF estimation from polarisation.

*Computer Vision and Image Understanding*, *111*(2), 126–141. http://doi.org/10.1016/j.cviu.2007.09.005

Bacour, C., Bréon, F.-M., & Maignan, F. (2006). Normalization of the directional effects in NOAA–AVHRR reflectance measurements for an improved monitoring of vegetation cycles. *Remote Sensing of Environment*, *102*(3), 402–413. http://doi.org/10.1016/j.rse.2006.03.006

Bacour, C., Jacquemoud, S., Tourbier, Y., Dechambre, M., & Frangi, J. (2002). Design and analysis of numerical experiments to compare four canopy reflectance models. *Remote Sensing of Environment*, *79*(1), 72–83.

Bannari, A., Morin, D., Bonn, F., & Huete, A. R. (1995). A review of vegetation indices. *Remote Sensing Reviews*, *13*(1–2), 95–120.

Bartlett, B., & Schott, J. R. (2009). Atmospheric compensation in the presence of clouds: an adaptive empirical line method (AELM) approach. *Journal of Applied Remote Sensing*, *3*(1), 1–16. http://doi.org/10.1117/1.3091937

Baugh, W. M., & Groeneveld, D. P. (2008). Empirical proof of the empirical line. *International Journal of Remote Sensing*, *29*(3), 665–672. http://doi.org/10.1080/01431160701352162

Bell, G. E., Howell, B. M., Johnson, G. V, Raun, W. R., Solie, J. B., & Stone, M. L. (2004). Optical Sensing of Turfgrass Chlorophyll Content and Tissue Nitrogen. *HortScience*, *39*(5), 1130–1132.

Bell, G. E., Martin, D. L., Wiese, S. G., Dobson, D. D., Smith, M. W., Stone, M. L., & Solie, J. B. (2002). Vehicle-Mounted Optical Sensing: An Objective Means for Evaluating Turf Quality. *Crop Science*, *42*(1), 197–201. Retrieved from http://www.ncbi.nlm.nih.gov/pubmed/11756274

Benton, L. M., Weltzin, J. F., Richardson, A. D., & Losleben, M. V. (2008). Towards a nation-wide phenology camera monitoring network. Retrieved from https://www.usanpn.org/files/shared/Benton_et_al_ESAposter_PhenoCam_Network.pdf

Berk, A., Anderson, G. P., Acharya, P. K., Bernstein, L. S., Muratov, L., Lee, J., … Shettle, E. P. (2006). MODTRAN 5: 2006 Update. *Proceedings of SPIE*, *6233*(1F), 1–8. http://doi.org/10.1117/12.665077

Berry, J., Heimes, F., & Smith, J. (1978). A portable instrument for simultaneous recording of scene composition and spectral reflectance. *Optical Engineering*, *17*(2), 143–146. Retrieved from http://opticalengineering.spiedigitallibrary.org/article.aspx?articleid=1221504

Bhandari, P., Voss, K. J., & Logan, L. (2011). An instrument to measure the downwelling polarized radiance distribution in the ocean. *Optics Express*, *19*(18), 17609–17620. Retrieved from http://www.ncbi.nlm.nih.gov/pubmed/21935128

Biggar, S. F., Thome, K., Geis, J., & Burkhart, C. (2004). Laser-based system for ground-based measurement of backscatter surface reflectance. In *IGARSS* (Vol. 3, pp. 1955–1957).

Biggar, S. F., Thome, K. J., & Wisniewski, W. (2003). Vicarious Radiometric Calibration of EO-1 Sensors by Reference to High-Reflectance Ground Targets. *IEEE Transactions on Geoscience and Remote Sensing*, *41*(6), 1174–1179.

Boucher, Y., Cosnefroy, H., Petit, D., Serrot, G., & Briottet, X. (1999). Comparison of measured and modeled BRDF of natural targets. In *Proceedings of SPIE Vol. 3699*. Retrieved from http://proceedings.spiedigitallibrary.org/proceeding.aspx?articleid=986972

Bouwmeester, J., & Guo, J. (2010). Survey of worldwide pico- and nanosatellite missions, distributions and subsystem technology. *Acta Astronautica*, *67*(7), 854–862. http://doi.org/10.1016/j.actaastro.2010.06.004

Bucher, T. U. (2004). A simple atmospheric correction for HRSC-AX high resolution image data: examples and conclusions from HRSC flight campaigns. In *Proceedings of SPIE* (Vol. 5574, p. 244). http://doi.org/10.1117/12.565409

Camacho-de Coca, F., Bréon, F. M., Leroy, M., & Garcia-Haro, F. J. (2004). Airborne measurement of hot spot reflectance signatures. *Remote Sensing of Environment*, *90*(1), 63–75. http://doi.org/10.1016/j.rse.2003.11.019

Camnet. (2012). Retrieved from http://www.hazecam.net/

Campbell, J. B. (1993). Evaluation of the dark-object subtraction technique for adjustment of multispectral remote-sensing data. In *Proceedings of SPIE* (Vol. 1819, pp. 176–188).

Chander, G., Angal, A., Xiong, X., Helder, D. L., Mishra, N., Choi, T., & Wu, A. (2010). Preliminary assessment of several parameters to measure and compare usefulness of the CEOS reference pseudo-invariant calibration sites. In R. Meynart, S. P. Neeck, & H. Shimoda (Eds.), *Proceedings of SPIE Vol. 7826* (Vol. 7826, p. 78262L–1–12). http://doi.org/10.1117/12.865166

Chander, G., Helder, D. L., Aaron, D., Mishra, N., & Shrestha, A. K. (2013). Assessment of Spectral , Misregistration , and Spatial Uncertainties Inherent in the Cross-Calibration Study. *IEEE Transactions on Geoscience and Remote Sensing*, *51*(13), 1282–1296.

Chander, G., Mishra, N., Helder, D. L., Member, S., Aaron, D. B., Angal, A., … Doelling, D. R. (2013). Applications of Spectral Band Adjustment Factors ( SBAF ) for Cross-Calibration. *IEEE Transactions on Geoscience and Remote Sensing*, *51*(3), 1267–1281.

Chavez, P. (1996). Image-Based Atmospheric Corrections- Revisited and Improved. *Photogrammetric Engineering and Remote Sensing*, *62*(9), 1025–1036.

Clark, B., Suomalainen, J., & Pellikka, P. (2011). The selection of appropriate spectrally bright pseudo-invariant ground targets for use in empirical line calibration of SPOT satellite imagery. *ISPRS Journal of Photogrammetry and Remote Sensing*, *66*(4), 429–445. http://doi.org/10.1016/j.isprsjprs.2011.02.003

Clark, R. N., Swayze, G. A., & Heidebrecht, K. (1995). Calibration to surface reflectance of terrestrial imaging spectrometry data: Comparison of methods(Abstract Only). In *Summaries of the 5th Annual JPL Airborne Earth Science Workshop* (pp. 41–42). Retrieved from http://scholar.google.com/scholar?hl=en&btnG=Search&q=intitle:Calibration+to+Surface+Reflectance+of+Terrestrial+Imaging+Spectrometry+Data+:+Comparison+of+Methods#0

CLARREO. (n.d.). Retrieved March 7, 2016, from http://clarreo.larc.nasa.gov/

Coburn, C., & Peddle, D. (2006). A low-cost field and laboratory goniometer system for estimating hyperspectral bidirectional reflectance. *Canadian Journal of Remote Sensing*, *32*(3), 244–253. Retrieved from http://pubs.casi.ca/doi/pdf/10.5589/m06-021

Colored Glass Bandpass Filters. (n.d.). Retrieved May 7, 2016, from http://www.edmundoptics.com/optics/optical-filters/bandpass-filters/colored-glass-bandpass-filters/1924/

Commission, E. (2014). RAMI, RAdiation transfer Model Intercomparison.

Congalton, R. (2010). Remote Sensing: An Overview. *GIScience & Remote Sensing*, *47*(4), 443–459. Retrieved from http://bellwether.metapress.com/index/D55921780Q70942P.pdf

Crippen, R. E. (1987). The regression intersection method of adjusting image data for band ratioing. *International Journal of Remote Sensing*, *8*(2), 137–155.

Curran, P. (1980). Multispectral remote sensing of vegetation amount. *Progress in Physical Geography*, *4*(3), 315–341. http://doi.org/10.1177/030913338000400301

Czapla-Myers, J. S. (2006). *Automated Ground-Based Methodology in Support of Vicarious Calibration*. University of Arizona.

Czapla-Myers, J. S., Anderson, N. J., & Biggar, S. F. (2013). Early ground-based vicarious calibration results for Landsat 8 OLI. In J. J. Butler, X. (Jack) Xiong, & X. Gu (Eds.), *Proc. SPIE 8866, Earth Observing Systems XVIII* (Vol. 8866, p. 88660S). http://doi.org/10.1117/12.2022493

Czapla-Myers, J. S., Leisso, N. P., Anderson, N. J., & Biggar, S. F. (2012). On-orbit radiometric calibration of Earth-observing sensors using the Radiometric Calibration Test Site (RadCaTS). In S. S. Shen & P. E. Lewis (Eds.), *Proc. SPIE 8390, Algorithms and Technologies for Multispectral, Hyperspectral, and Ultraspectral Imagery XVIII* (Vol. 8390, p. 83902B). http://doi.org/10.1117/12.918614

Czapla-Myers, J. S., Thome, K. J., & Biggar, S. F. (2009). Calibration and characterization of a digital camera for bidirectional reflectance distribution function retrieval of vicarious calibration sites. *Journal of Applied Remote Sensing*, *3*(1), 33519. http://doi.org/10.1117/1.3116662

Dana, K. J., & Wang, J. (2004). Device for convenient measurement of spatially varying bidirectional reflectance. *Journal of the Optical Society of America. A, Optics, Image Science, and Vision*, *21*(1), 1–12. Retrieved from http://www.ncbi.nlm.nih.gov/pubmed/14725392

Darvishzadeh, R., Skidmore, A., Schlerf, M., & Atzberger, C. (2008). Inversion of a radiative transfer model for estimating vegetation LAI and chlorophyll in a heterogeneous grassland. *Remote Sensing of Environment*, *112*(5), 2592–2604. http://doi.org/10.1016/j.rse.2007.12.003

Darvishzadeh, R., Skidmore, A., Schlerf, M., Atzberger, C., Corsi, F., & Cho, M. (2008). LAI and chlorophyll estimation for a heterogeneous grassland using hyperspectral measurements. *ISPRS Journal of Photogrammetry and Remote Sensing*, *63*(4), 409–426. http://doi.org/10.1016/j.isprsjprs.2008.01.001

Davis, S. M., Landgrebe, D. A., Phillips, T. L., Swain, P. H., Hoffer, R. M., Lindenlaub, J. C., &

Silva, L. F. (1978). *Remote Sensing the Quantitative Approach*. (P. H. Swain, S. M., & Davis, Eds.). London: McGraw-Hill International Book Co.

De Santis, A., & Chuvieco, E. (2007). Burn severity estimation from remotely sensed data: Performance of simulation versus empirical models. *Remote Sensing of Environment*, *108*(4), 422–435. http://doi.org/10.1016/j.rse.2006.11.022

Demircan, A., Schuster, R., Radke, M., Schonermark, M., & Roser, H. P. (2000). Use of a wide angle CCD line camera for BRDF measurements. *Infrared Physics & Technology*, *41*, 11–19.

Dinter, T., Von Hoyningen-Huene, W., Burrows, J. P., Kokhanovsky, A., Bierwirth, E., Wendisch, M., … Diouri, M. (2009). Retrieval of aerosol optical thickness for desert conditions using MERIS observations during the SAMUM campaign. *Tellus B*, *61*(1), 229–238. http://doi.org/10.1111/j.1600-0889.2008.00391.x

Dymond, J. R., & Trotter, C. M. (1997). Directional reflectance of vegetation measured by a calibrated digital camera. *Applied Optics*, *36*(18), 4314–9. Retrieved from http://www.ncbi.nlm.nih.gov/pubmed/18253461

Farrand, W. H., Singer, R. B., & Mer, E. (1994). Retrieval of Apparent Surface Reflectance from AVIRIS Data : A Comparison of Empirical Line , Radiative Transfer , and Spectral Mixture Methods. *Remote Sensing of Environment*, *47*, 311–321.

Feret, J.-B., François, C., Asner, G. P., Gitelson, A. a., Martin, R. E., Bidel, L. P. R., … Jacquemoud, S. (2008). PROSPECT-4 and 5: Advances in the leaf optical properties model separating photosynthetic pigments. *Remote Sensing of Environment*, *112*(6), 3030–3043. http://doi.org/10.1016/j.rse.2008.02.012

Ferrero, A., Campos, J., & Pons, A. (2006). Low-uncertainty absolute radiometric calibration of a CCD. *Metrologia*, *43*(2), S17–S21. http://doi.org/10.1088/0026-1394/43/2/S04

Filip, J., Vavra, R., Haindl, M., Zid, P., Krupicka, M., & Havran, V. (2013). BRDF Slices: Accurate Adaptive Anisotropic Appearance Acquisition. In *IEEE Conference on Computer Vision and Pattern Recognition* (pp. 1468–1473). Ieee. http://doi.org/10.1109/CVPR.2013.193

Foody, G. M., Cutler, M. E., Mcmorrow, J., Pelz, D., Tangki, H., Boyd, D. S., & Douglas, I. a N. (2001). Mapping the biomass of Bornean tropical rain forest from remotely sensed data ESTIMATION AND MAPPING. *Global Ecology and Biogeography*, *10*(4), 379–387.

Gamon, J., Cheng, Y., Claudio, H., Mackinney, L., & Sims, D. (2006). A mobile tram system for systematic sampling of ecosystem optical properties. *Remote Sensing of Environment*, *103*(3), 246–254. http://doi.org/10.1016/j.rse.2006.04.006

Gamon, J., Rahman, A., Dungan, J., Schildhauer, M., & Huemmrich, K. (2006). Spectral Network (SpecNet)—What is it and why do we need it? *Remote Sensing of Environment*, *103*(3), 227–235. http://doi.org/10.1016/j.rse.2006.04.003

Gao, B.-C., Montes, M. J., Davis, C. O., & Goetz, A. F. H. (2009). Atmospheric correction algorithms for hyperspectral remote sensing data of land and ocean. *Remote Sensing of Environment*, *113*(supplement #1), S17–S24. http://doi.org/10.1016/j.rse.2007.12.015

Gates, D. M., Keegan, H. J., Schleter, J. C., & Weidner, V. R. (1965). Spectral Properties of Plants. *Applied Optics*, *4*(1), 11–20. http://doi.org/10.1364/AO.4.000011

Geiger, B., Demircan, A., & Schönermark, M. Von. (2001). Exploiting multi-angular observations for vegetation monitoring. In *Proceedings of SPIE Vol. 4171* (Vol. 4171, pp. 58–68).

Georgiev, G., Butler, J., & Thome, K. (2011). Assessment of multiangular polarization contribution to the bidirectional reflectance of natural samples. In *IGARSS* (pp. 1017–1020). Retrieved from http://cf.gsfc.nasa.gov/docs/Scatterometer/Assessment of multiangular polarization contribution.pdf

Georgiev, G., Butler, J., Thome, K., Ranson, K. J., & King, M. (2010). The effect of incident light polarization on vegetation bidirectional reflectance factor. In *IGARSS* (pp. 1652–1655). Retrieved from http://ieeexplore.ieee.org/xpls/abs_all.jsp?arnumber=5652893

Ghosh, A., Heidrich, W., Achutha, S., & O'Toole, M. (2010). A Basis Illumination Approach to BRDF Measurement. *International Journal of Computer Vision*, *90*(2), 183–197. http://doi.org/10.1007/s11263-008-0151-7

Gianelle, D., & Guastella, F. (2007). Nadir and off- nadir hyperspectral field data: strengths and limitations in estimating grassland biophysical characteristics. *International Journal of Remote Sensing*, *28*(7), 1547–1560. http://doi.org/10.1080/01431160600658180

Giardino, C., & Brivio, P. a. (2003). The application of a dedicated device to acquire bidirectional reflectance factors over natural surfaces. *International Journal of Remote Sensing*, *24*(14), 2989–2995. http://doi.org/10.1080/0143116031000094782

Gleason, A. C. R., Voss, K. J., Gordon, H. R., Twardowski, M., Sullivan, J., Trees, C., … Lee, Z.-P. (2012). Detailed validation of the bidirectional effect in various Case I and Case II waters. *Optics Express*, *20*(7), 7630–45. Retrieved from http://www.ncbi.nlm.nih.gov/pubmed/22453442

Goetz, A. F. H. (2009). Three decades of hyperspectral remote sensing of the Earth: A personal view. *Remote Sensing of Environment*, *113*(supplement 1), S5–S16. http://doi.org/10.1016/j.rse.2007.12.014

Goetz, A. F. H., Heidebrecht, K. B., Kindel, B., & Boardman, J. W. (1998). Using ground spectral irradiance for model correction of AVIRIS data. *Summaries of the Seventh Annual JPL Airborne Earth Science Workshop*, *97–21*(1), 159–168.

Goodin, D. G., Gao, J., & Henebry, G. M. (2004). The Effect of Solar Illumination Angle and Sensor View Angle on Observed Patterns of Spatial Structure in Tallgrass Prairie. *IEEE Transactions on Geoscience and Remote Sensing*, *42*(1), 154–165. http://doi.org/10.1109/TGRS.2003.815674

Greivenkamp, J. E. (2004). *Field Guide to Geometrical Optics*. Bellingham, Washington: SPIE.

Gueymard, C. (1995). *SMARTS, A Simple Model of the Atmospheric Radiative Transfer of Sunshine: Algorithms and Performance Assessment* (No. FSEC-PF-270-95). Florida.

Gueymard, C. (2001). Parameterized Transmittance Model for Direct Beam and Circumsolar Spectral Irradiance. *Solar Energy*, *71*(5), 325–346.

Hadjimitsis, D., & Clayton, C. R. I. (2004). An assessment of the effectiveness of atmospheric correction algorithms through the remote sensing of some reservoirs. *International Journal of Remote Sensing*, *25*(18), 3651–3674. Retrieved from http://www.tandfonline.com/doi/abs/10.1080/01431160310001647993

Hagolle, O., Nicolas, J., Fougnie, B., Cabot, F., & Henry, P. (2004). Absolute Calibration of VEGETATION Derived From an Interband Method Based on the Sun Glint Over Ocean. *IEEE Transactions on Geoscience and Remote Sensing*, *42*(7), 1472–1481.

Hapke, B., DiMucci, D., Nelson, R., & Smythe, W. (1996). The cause of the hot spot in vegetation canopies and soils: Shadow-hiding versus coherent backscatter. *Remote Sensing of Environment*, *58*(1), 63–68. http://doi.org/10.1016/0034-4257(95)00257-X

Helder, D. L., Basnet, B., & Morstad, D. L. (2010). Optimized identification of worldwide radiometric pseudo-invariant calibration sites. *Canadian Journal of Remote Sensing*, *36*(5), 527–539.

Helder, D. L., Malla, R., Mettler, C. J., Markham, B. L., & Micijevic, E. (2012). Landsat 4 Thematic Mapper Calibration Update. *IEEE Transactions on Geoscience and Remote Sensing*, *50*(6), 2400–2408.

Helder, D. L., & Ruggles, T. A. (2004). Landsat Thematic Mapper Reflective-Band Radiometric Artifacts. *IEEE Transactions on Geoscience and Remote Sensing*, *42*(12), 2704–2716.

Helder, D. L., Ruggles, T. A., Dewald, J. D., & Madhaven, S. (2004). Landsat-5 Thematic Mapper Reflective-Band Radiometric Stability. *IEEE Transactions on Geoscience and Remote Sensing*, *42*(12), 2730–2746.

Helder, D. L., Thome, K., Aaron, D., Leigh, L., Czapla-Myers, J., Leisso, N., … Anderson, N. (2012). Recent surface reflectance measurement campaigns with emphasis on best practices, SI traceability and uncertainty estimation. *Metrologia*, *49*(2), S21–S28. http://doi.org/10.1088/0026-1394/49/2/S21

Helder, D. L., Thome, K. J., Mishra, N., Chander, G., Xiong, X., Angal, A., & Choi, T. (2013). Absolute Radiometric Calibration of Landsat Using a Pseudo Invariant Calibration Site. *IEEE Transactions on Geoscience and Remote Sensing*, *51*(3), 1360–1369.

Hilker, T., Gitelson, A., Coops, N. C., Hall, F. G., & Black, T. A. (2011). Tracking plant physiological properties from multi-angular tower-based remote sensing. *Oecologia*, *165*(4), 865–76. http://doi.org/10.1007/s00442-010-1901-0

Holmes, J., & Thome, K. (2001). Comparison of modeled and measured downwelling, diffuse irradiance at a ground-reference calibration test site. *INTERNATIONAL GEOSCIENCE AND REMOTE SENSING SYMPOSIUM*, *1*(I), 78–80. Retrieved from http://ieeexplore.ieee.org/xpls/abs_all.jsp?arnumber=976062

Hook, S. J., Chander, G., Barsi, J. A., Alley, R. E., Abtahi, A., Palluconi, F. D., … Helder, D. L. (2004). In-Flight Validation and Recovery of Water Surface Temperature With Landsat-5 Thermal Infrared Data Using an Automated High-Altitude Lake Validation Site at Lake Tahoe. *IEEE Transactions on Geoscience and Remote Sensing*, *42*(12), 2767–2776.

Hu, B., Lucht, W., Li, X., & Strahler, A. (1997). Validation of kernel-driven semiempirical models for the surface bidirectional reflectance distribution function of land surfaces. *Remote Sensing of Environment*, *62*, 201–214. Retrieved from http://www.sciencedirect.com/science/article/pii/S0034425797000825

Islam, M. R., Yamaguchi, Y., & Ogawa, K. (2001). Suspended sediment in the Ganges and Brahmaputra Rivers in Bangladesh: Observation from TM and AVHRR data. *Hydrological Processes*, *15*(3), 493–509. http://doi.org/10.1002/hyp.165

ITC's database of Satellites and Sensors. (n.d.). Retrieved from http://www.itc.nl/research/products/sensordb/allsensors.aspx

Jacobs, N., Burgin, W., Fridrich, N., Abrams, A., Miskell, K., Braswell, B. H., … Pless, R. (2009). The Global Network of Outdoor Webcams : Properties and Applications. *Proceedings ACM GIS '09*, 111–120. Retrieved from http://dl.acm.org/citation.cfm?id=1653789

Jacquemoud, S., & Baret, F. (1990). PROSPECT: A model of leaf optical properties spectra. *Remote Sensing of Environment*, *34*(2), 75–91. http://doi.org/10.1016/0034-4257(90)90100-Z

Jacquemoud, S., Verhoef, W., Baret, F., Bacour, C., Zarco-Tejada, P. J., Asner, G. P., … Ustin, S. L. (2009). PROSPECT+SAIL models: A review of use for vegetation characterization. *Remote Sensing of Environment*, *113*, S56–S66. http://doi.org/10.1016/j.rse.2008.01.026

Jacquemoud, S., Verhoef, W., Baret, F., Zarco-Tejada, P. J., Asner, G. P., François, C., & Ustin, S. L. (2006). PROSPECT + SAIL : 15 Years of Use for Land Surface Characterization. In *In Geoscience and Remote Sensing Symposium, 2006. IEEE International Conference* (Vol. 0, pp. 1992–1995).

Jensen, J. R. (2007). *Remote Sensing of the Environment: An Earth Resources Perspective*. (J. Howard, D. Kaveney, K. Sciaparelli, E. Thomas, & B. Booth, Eds.) (2nd ed.). Upper Saddle River, NJ: Pearson Prentic Hall.

Jensen, J. R., & Schill, S. R. (2000). Bidirectional Reflectance Distribution Function ( BRDF ) Characteristics of Smooth Cordgrass ( Spartina alterniflora ) Obtained Using a Sandmeier Field Goniometer Bidirectional Reflectance Distribution Function ( BRDF ) Characteristics of Smooth Cordgrass. *Geocarto International*, *15*(2), 23–30.

Jin, Y., Gao, F., Schaaf, C. B., Li, X., Strahler, A. H., Bruegge, C. J., … Member, A. (2002). Improving MODIS Surface BRDF / Albedo Retrieval. *IEEE Transactions on Geoscience and Remote Sensing*, *40*(7), 1593–1604.

Karpouzli, E., & Malthus, T. (2003). The empirical line method for the atmospheric correction of

IKONOS imagery. *International Journal of Remote Sensing*, *24*(5), 1143–1150. http://doi.org/10.1080/0143116021000026779

Kennedy, R. E., Cohen, W. B., & Takao, G. (1997). Empirical Methods To Compensate for a View-Angle-Dependent Brightness Gradient in AVIRIS Imagery. *Remote Sensing of Environment*, *62*, 277–291.

Kim, D. B., Park, K. S., Kim, K. Y., Seo, M. K., & Lee, K. H. (2009). High-dynamic-range camera-based bidirectional reflectance distribution function measurement system for isotropic materials. *Optical Engineering*, *48*(9), 93601-1–11. http://doi.org/10.1117/1.3223247

Knapp, A. K., Smith, M. D., Hobbie, S. E., Collins, S. L., Fahey, T. J., Hansen, G. J. A., … Webster, J. R. (2012). Past, Present, and Future Roles of Long-Term Experiments in the LTER Network. *BioScience*, *62*(4), 377–389. http://doi.org/10.1525/bio.2012.62.4.9

Knighton, N., & Bugbee, B. (2005). *A Mixture of Barium Sulfate and White Paint is a Low-Cost Substitute Reflectance Standard for Spectralon ® %. Utah State University*. Retrieved from http://cpl.usu.edu/files/publications/factsheet/pub__5942708.pdf

Kriebel, K. T. (1978). Measured spectral bidirectional reflection properties of four vegetated surfaces. *Applied Optics*, *17*(2), 253–9. Retrieved from http://www.ncbi.nlm.nih.gov/pubmed/20174392

Kumar, R., & Silva, L. (1974). Statistical separability of spectral classes of blighted corn. *Remote Sensing of Environment*, *3*(2), 109–115. http://doi.org/10.1016/0034-4257(74)90053-4

Lach, S. R., & Kerekes, J. P. (2008). Atmospheric compensation using a geometrically-compensated empirical line method. In *Geoscience and Remote Sensing Symposium, 2008. IGARSS 2008* (pp. 664–667). IEEE. http://doi.org/10.1109/IGARSS.2008.4779435

Law, B. E. (2007). AmeriFlux Network Aids Global Synthesis. *Eos, Transactions American Geophysical Union*, *88*(28), 286.

Leuning, R., Hughes, D., Daniel, P., Coops, N., & Newnham, G. (2006). A multi-angle spectrometer for automatic measurement of plant canopy reflectance spectra. *Remote Sensing of Environment*, *103*(3), 236–245. http://doi.org/10.1016/j.rse.2005.06.016

Lewis, P. (1995). The utility of kernel-driven BRDF models in global BRDF and albedo studies. *1995 International Geoscience and Remote Sensing Symposium, IGARSS '95. Quantitative Remote Sensing for Science and Applications*, *2*, 1186–1188.

http://doi.org/10.1109/IGARSS.1995.521179

Liang, S., Member, S., Fang, H., & Chen, M. (2001). Atmospheric Correction of Landsat ETM+ Land Surface Imagery — Part I : Methods. *IEEE Transactions on Geoscience and Remote Sensing*, *39*(11), 2490–2498.

Liangrocapart, S., & Petrou, M. (2002). A two-layer model of the bidirectional reflectance of homogeneous vegetation canopies. *Remote Sensing of Environment*, *80*(1), 17–35. http://doi.org/10.1016/S0034-4257(01)00264-4

Lukashin, C., Wielicki, B. A., Young, D. F., Thome, K., Jin, Z., & Sun, W. (2013). Uncertainty Estimates for Imager Reference Inter-Calibration With CLARREO Reflected Solar Spectrometer. *IEEE Transactions on Geoscience and Remote Sensing*, *51*(3), 1425–1436.

Mahiny, A. S., & Turner, B. J. (2007). A Comparison of Four Common Atmospheric Correction Methods. *Photogrammetric Engineering and Remote Sensing*, *73*(4), 361–368.

Maignan, F., Bréon, F.-M., Fédèle, E., & Bouvier, M. (2009). Polarized reflectances of natural surfaces: Spaceborne measurements and analytical modeling. *Remote Sensing of Environment*, *113*(12), 2642–2650. http://doi.org/10.1016/j.rse.2009.07.022

Maignan, F., Bréon, F.-M., & Lacaze, R. (2004). Bidirectional reflectance of Earth targets: evaluation of analytical models using a large set of spaceborne measurements with emphasis on the Hot Spot. *Remote Sensing of Environment*, *90*(2), 210–220. http://doi.org/10.1016/j.rse.2003.12.006

Marschner, S. R., Westin, S. H., Lafortune, E. P., & Torrance, K. E. (2000). Image-based bidirectional reflectance distribution function measurement. *Applied Optics*, *39*(16), 2592–2600. Retrieved from http://www.ncbi.nlm.nih.gov/pubmed/18345176

Martonchik, J. V, Pinty, B., & Verstraete, M. M. (2002). Note on "An Improved Model of Surface BRDF-Atmospheric Coupled Radiation." *IEEE Transactions on Geoscience and Remote Sensing*, *40*(7), 1637–1639.

Miller, C. J. (2002). Performance Assessment of ACORN Atmospheric Correction Algorithm. In *PROCEEDINGS of SPIE THE INTERNATIONAL SOCIETY FOR OPTICAL ENGINEERING* (Vol. 4725, pp. 438–449).

Moran, M. S., Bryant, R., Thome, K., Ni, W., Nouvellon, Y., & Gonzalez-dugo, M. P. (2001). A refined empirical line approach for reflectance factor retrieval from Landsat-5 TM and

Landsat-7 ETM +. *Remote Sensing of Environment*, *78*, 71–82.

Moran, M. S., Clarke, T., Qi, J., & Barnes, E. (1997). Practical techniques for conversion of airborne imagery to reflectances. *16th Biannual Workshop on Color Photography and Videography in Research Assessment*, 82–95. Retrieved from http://scholar.google.com/scholar?hl=en&btnG=Search&q=intitle:Practical+Techniques+for+Conversion+of+Airborne+Imagry+to+Reflectances#0

Moran, M. S., Jackson, R. D., Slater, P. N., & Teiuet, P. M. (1992). Evaluation of Simplified Procedures for Retrieval of Land Surface Reflectance Factors from Satellite Sensor Output. *Remote Sensing of Environment*, *41*(23), 169–184.

Nandy, P. (2000). *Evaluation of a CCD Camera System for BRDF Retrieval for Remote Sensing Applications for Vicarious Calibration*.

Nandy, P., Thome, K., & Biggar, S. (2001). Characterization and field use of a CCD camera system for retrieval of bidirectional reflectance distribution function. *Journal of Geophysical Research: Atmospheres*, *106*(D11), 11,957-11,966.

Nguyen, U., Glenn, E. P., Nagler, P. L., & Scott, R. L. (2015). Long-term decrease in satellite vegetation indices in response to environmental variables in an iconic desert riparian ecosystem: The Upper San Pedro, Arizona, United States. *Ecohydrology*, *8*(4), 610–625. http://doi.org/10.1002/eco.1529

Ni, W., & Li, X. (2000). A Coupled Vegetation–Soil Bidirectional Reflectance Model for a Semiarid Landscape. *Remote Sensing of Environment*, *74*(1), 113–124. http://doi.org/10.1016/S0034-4257(00)00127-9

Nilson, T., & Kuusk, A. (1989). A reflectance model for the homogeneous plant canopy and its inversion. *Remote Sensing of Environment*, *27*(2), 157–167. http://doi.org/10.1016/0034-4257(89)90015-1

Otterman, J., & Robinove, C. (1981). Effects of the atmosphere on the detection of surface changes from Landsat multispectral scanner data. *Remote Sensing*, *2*(4), 351–360. Retrieved from http://www.tandfonline.com/doi/full/10.1080/01431168108948369

Pagnutti, M., Blonski, S., Cramer, M., Helder, D., Holekamp, K., Honkavaara, E., & Ryan, R. (2010). Targets , methods , and sites for assessing the in-flight spatial resolution of electro-optical data products. *Canadian Journal of Remote Sensing*, *36*(5), 583–601.

Parada, R. J., Thome, K. J., & Santer, R. P. (1997). Results of dark target vicarious calibration using Lake Tahoe. In *Proceedings of SPIE Vol. 2957* (Vol. 2957, pp. 332–341).

Qaid, A., Basavarajappa, H., Rajendran, S., Ashfaq, S., & Xu, J. (2009). Calibration of ASTER and ETM + imagery using empirical line method—A case study of north-east of Hajjah, Yemen. *Geo-Spatial Information Science*, *12*(3), 197–201. http://doi.org/10.1007/s11806-009-0052-0

Qu, Z., Kindel, B., & Goetz, A. (2003). The High Accuracy Atmospheric Correction for Hyperspectral Data (HATCH) Model. *IEEE Transactions on Geoscience and Remote Sensing*, *41*(6), 1223–1231. Retrieved from http://ieeexplore.ieee.org/xpls/abs_all.jsp?arnumber=1220230

Rahman, M. M., Csaplovics, E., & Koch, B. (2005). An efficient regression strategy for extracting forest biomass information from satellite sensor data. *International Journal of Remote Sensing*, *26*(7), 1511–1519. http://doi.org/10.1080/01431160500044705

Richardson, A. D., Braswell, B. H., Hollinger, D. Y., Jenkins, J. P., & Ollinger, S. V. (2009). Near-surface remote sensing of spatial and temporal variation in canopy phenology. *Ecological Applications : A Publication of the Ecological Society of America*, *19*(6), 1417–28. Retrieved from http://www.ncbi.nlm.nih.gov/pubmed/19769091

Robinson, B. F., & Biehl, L. L. (1982). Calibration Procedures for Measurement of Reflectance Factor in Remote Sensing Field Research. In *Proceedings of the Society of Photo-Optical Instrumentation Engineering* (pp. 16–26).

Roujean, J.-L., Leroy, M., & Deschamps, P.-Y. (1992). A Bidirectional Reflectance Model of the Earth's surface for the Correction of Remote Sensing Data. *Journal of Geophysical Research*, *97*(D18), 20455–20468.

Rowan, L., Wetlaufer, P., Goetz, A., Billingsley, F., & Stewart, J. (1974). Discrimination of rock types and altered areas in Nevada by the use of ERTS images. *Geological Survey Prossional Paper 883*. Retrieved from http://scholar.google.com/scholar?hl=en&btnG=Search&q=intitle:DISCRIMINATION+OF+ROCK+TYPES+AND+ALTERED+AREAS+IN+NEVADA+BY+THE+use+of+ERTS+images#9

Salas, A. G., Attai, W., Oyadomari, K. Y., Priscal, C., Shimmin, R. S., Gazulla, O. T., & Wolfe, J. L. (2014). Phonesat In-Flight Exerience Results. In *The 4S Symposium* (pp. 1–19).

Sandmeier, S. R. (1999). Acquisition of Bidirectional Reflectance Factor Data with Field Goniometers. *Remote Sensing of Environment*, *73*(3), 257–269.

Sandmeier, S. R., & Itten, K. I. (1999). A field goniometer system (FIGOS) for acquisition of hyperspectral BRDF data. *IEEE Transactions on Geoscience and Remote Sensing*, *37*(2), 978–986. http://doi.org/10.1109/36.752216

Sandmeier, S. R., Müller, C., Hosgood, B., & Andreoli, G. (1998a). Physical Mechanisms in Hyperspectral BRDF Data of Grass and Watercress. *Remote Sensing of Environment*, *66*(2), 222–233. http://doi.org/10.1016/S0034-4257(98)00060-1

Sandmeier, S. R., Müller, C., Hosgood, B., & Andreoli, G. (1998b). Sensitivity Analysis and Quality Assessment of Laboratory BRDF Data. *Remote Sensing of Environment*, *64*(2), 176–191. http://doi.org/10.1016/S0034-4257(97)00178-8

Sato, H., Robinson, M. S., Mahanti, P., & Boyd, A. K. (2013). Temperature Dependent Spectral Responsivity of the LROC WAC. In *44th Lunar and Planetary Science Conference* (Vol. 3603).

Schaepman-Strub, G., Schaepman, M. E., Painter, T. H., Dangel, S., & Martonchik, J. V. (2006). Reflectance quantities in optical remote sensing—definitions and case studies. *Remote Sensing of Environment*, *103*(1), 27–42. http://doi.org/10.1016/j.rse.2006.03.002

Schiller, S., & Luvall, J. (1994). A portable ground-based atmospheric monitoring system (PGAMS) for the calibration and validation of atmospheric correction algoithms to satellite images. *SPIE*, *2231*, 191–198.

Schott, J. R., Salvaggio, C., & Volchok, W. J. (1988). Radiometric scene normalization using pseudoinvariant features. *Remote Sensing of Environment*, *26*(1), 1–16. http://doi.org/10.1016/0034-4257(88)90116-2

Schut, A. G. T., Ketelaars, J. J. M. H., Meuleman, J., Kornet, J. G., & Lokhorst, C. (2002). Novel Imaging Spectroscopy for Grass Sward Characterization. *Biosystems Engineering*, *82*(2), 131–141. http://doi.org/10.1006/bioe.2002.0060

Sellers, P. J., Hall, F. G., Asrar, G., Strebel, D. E., & Murphy, R. E. (1988). The First ISLSCP Field Experiment (FIFE). *Bulletin of the American Meteorlogical Society*, *69*(1), 22–27.

Shell II, J. R. (2005). *Polarimetric Remote Sensing in the Visible to Near Infrared*. Rochester Institue of Technology. Retrieved from http://dirsig.org/docs/shell.pdf

Si, Y., Schlerf, M., Zurita-milla, R., Skidmore, A., & Wang, T. (2012). Remote Sensing of Environment Mapping spatio-temporal variation of grassland quantity and quality using MERIS data and the PROSAIL model. *Remote Sensing of Environment*, *121*, 415–425. http://doi.org/10.1016/j.rse.2012.02.011

Smith, G. M., & Milton, E. J. (1999). The use of the empirical line method to calibrate remotely sensed data to reflectance. *International Journal of Remote Sensing*, *20*(13), 2653–2662. http://doi.org/10.1080/014311699211994

Snyder, W. C. (1998). BRDF models to predict spectral reflectance and emissivity in the thermal infrared. *IEEE Transactions on Geoscience and Remote Sensing*, *36*(1), 214–225. http://doi.org/10.1109/36.655331

Sonmez, N., Emekli, Y., Sari, M., & Bastug, R. (2008). Relationship between spectral reflectance and water stress conditions of Bermuda grass ( Cynodon dactylon L .). *New Zealand Journal of Agricultural Research*, *51*(3), 223–233.

Staben, G. W., Pfitzner, K., Bartolo, R., & Lucieer, A. (2012). Empirical line calibration of WorldView-2 satellite imagery to reflectance data: using quadratic prediction equations. *Remote Sensing Letters*, *3*(6), 521–530. http://doi.org/10.1080/01431161.2011.609187

Strahler, A. H., & Muller, J. P. (1996). *MODIS BRDF/Albedo product: algorithm theoretical basis document version 4.0. MODIS ....* Retrieved from http://modis-sr.ltdri.org/publications/MODIS_BRDF.pdf

Strahler, A. H., & Muller, J. P. (1999). *MODIS BRDF Albedo Product : Algorithm Theoretical Basis Document Version 5.0. MODIS ....*

Sun, B., Sunkavalli, K., Ramamoorthi, R., Belhumeur, P. N., & Nayar, S. K. (2007). Time-varying BRDFs. In *IEEE transactions on visualization and computer graphics* (Vol. 13, pp. 595–609). http://doi.org/10.1109/TVCG.2007.1013

Teillet, P. M., Barsi, J. a., Chander, G., & Thome, K. J. (2007). Prime Candidate Earth Targets for the Post-Launch Radiometric Calibration of Space-Based Optical Imaging Instruments. In J. J. Butler & J. Xiong (Eds.), *Proceedings of SPIE Vol. 6677* (Vol. 6677, p. 66770S–1–12). http://doi.org/10.1117/12.733156

Teillet, P. M., & Fedosejevs, C. (1995). On the dark target approach to atmospheric correction of remotely sensed data. *Canadian Journal of Remote Sensing*, *21*(4), 374–387. http://doi.org/10.1080/07038992.1995.10855161

Teillet, P. M., Fedosejevs, G., Thome, K. ., & Barker, J. L. (2007). Impacts of spectral band difference effects on radiometric cross-calibration between satellite sensors in the solar-reflective spectral domain. *Remote Sensing of Environment*, *110*(3), 393–409. http://doi.org/10.1016/j.rse.2007.03.003

Teillet, P., Thome, K., Fox, N., & Morisette, J. (2001). Earth Observation Sensor Calibration Using a Global Instremented and Automated Network of Test Sites (GIANTS). *Proceedings of SPIE*, *4540*, 246–254.

Thome, K. J., Barnes, R., Baize, R., O'Connell, J., & Hair, J. (2010). Calibration of the reflected solar instrument for the climate absolute radiance and refractivity observatory. In *IGARSS* (pp. 2275–2278). Retrieved from http://ieeexplore.ieee.org/xpls/abs_all.jsp?arnumber=5651486

Thome, K. J., Biggar, S. F., & Choi, H. J. (2004). Vicarious Calibration of TERRA ASTER, MISR and MODIS. In W. L. Barnes & J. J. Butler (Eds.), *Proceedings of SPIE Vol. 5542* (Vol. 5542, pp. 290–299). http://doi.org/10.1117/12.559942

Thome, K. J., Czapla-Myers, J., Kuester, M., & Anderson, N. (2008). Accuracy Assessment for the Radiometric Calibration of Imaging Sensors Using Preflight Techniques Relying on the Sun as a Source. In J. J. Butler & J. Xiong (Eds.), *Proceedings of SPIE Vol. 7081* (Vol. 7081, pp. 708118-1–12). http://doi.org/10.1117/12.795681

Thome, K. J., Czapla-Myers, J., Leisso, N., McCorkel, J., & Buchanan, J. (2008). Intercomparison of imaging sensors using automated ground measurements. In *IGARSS* (pp. 1332–1335). Retrieved from https://www.securecms.com/IGARSS2008/Abstracts/pdfs/1794.pdf

Thome, K. J., D'Amico, J., & Hugon, C. (2006). Intercomparison of Terra ASTER , MISR , and MODIS , and Landsat-7 ETM+. In *IEEE International Symposium on Geoscience and Remote Sensing* (pp. 1772–1775).

Thome, K. J., Geis, J., & Cattrall, C. (2005). Comparison of Ground-Reference Calibration Results for Landsat-7 ETM+ for Large and Small Test Sites. In J. J. Butler (Ed.), *Proceedings of SPIE Vol. 5882* (Vol. 5882, p. 58820A–1–9). http://doi.org/10.1117/12.617856

Thome, K. J., Mccorkel, J., & Czapla-myers, J. (2013). In-Situ Transfer Standard and Coincident-View Intercomparisons for Sensor Cross-Calibration. *IEEE Transactions on*

*Geoscience and Remote Sensing*, *51*(3), 1088–1097.

Thome, K. J., Parada, R., Schiller, S., Conel, J., & LaMarr, J. (2000). Evaluation of the use of dark and bright targets for the in-flight calibration of AVIRIS. *STAR*, *38*. Retrieved from http://trs-new.jpl.nasa.gov/dspace/handle/2014/18960

Vaudour, E., Moeys, J., Gilliot, J. M., & Coquet, Y. (2008). Spatial retrieval of soil reflectance from SPOT multispectral data using the empirical line method. *International Journal of Remote Sensing*, *29*(19), 5571–5584. http://doi.org/10.1080/01431160802060920

Verhoef, W. (1984). Light scattering by leaf layers with application to canopy reflectance modeling: The SAIL model. *Remote Sensing of Environment*, *16*(2), 125–141. http://doi.org/10.1016/0034-4257(84)90057-9

Vermote, E., & Tanré, D. (1997). Second simulation of the satellite signal in the solar spectrum, 6S: An overview. *IEEE Transactions on Geoscience and Remote Sensing and Remote Sensing*, *35*(3), 675–686. Retrieved from http://ieeexplore.ieee.org/xpls/abs_all.jsp?arnumber=581987

Vincent, R. K. (1972). An ERTS multispectral scanner experiment for mapping iron compounds. In *Proceedings of the 8th Int. Symp. on Remote Sens. of Environ.* (pp. 1239–1247). Retrieved from http://adsabs.harvard.edu/abs/1972rse..conf.1239V

Vohland, M., & Jarmer, T. (2008). Estimating structural and biochemical parameters for grassland from spectroradiometer data by radiative transfer modelling (PROSPECT+SAIL). *International Journal of Remote Sensing*, *29*(1), 191–209. http://doi.org/10.1080/01431160701268947

Voss, K. J., & Chapin, A. (2005). Upwelling radiance distribution camera system, NURADS. *Optics Express*, *13*(11), 4250–4262. Retrieved from http://www.ncbi.nlm.nih.gov/pubmed/19495340

Voss, K. J., Chapin, A., Monti, M., & Zhang, H. (2000). Instrument to measure the bidirectional reflectance distribution function of surfaces. *Applied Optics*, *39*(33), 6197–6206. Retrieved from http://www.ncbi.nlm.nih.gov/pubmed/18354628

Voss, K. J., & Souaidia, N. (2010). POLRADS: polarization radiance distribution measurement system. *Optics Express*, *18*(19), 19672–19680. Retrieved from http://www.ncbi.nlm.nih.gov/pubmed/20940862

Walthall, C. L., Norman, J. M., Welles, J. M., Campbell, G., & Blad, B. L. (1985). Simple equation to approximate the bidirectional reflectance from vegetative canopies and bare soil surfaces. *Applied Optics*, *24*(3), 383–387. Retrieved from http://www.ncbi.nlm.nih.gov/pubmed/18216958

Wang, L., Dong, T., Zhang, G., & Niu, Z. (2013). LAI Retrieval Using PROSAIL Model and Optimal Angle Combination of Multi-Angular Data in Wheat. *IEEE Journal of Selected Topics in Applied Earth Observations and Remote Sensing*, *6*(3), 1730–1736. http://doi.org/10.1109/JSTARS.2013.2261474

Wang, Y., Czapla-Myers, J., Lyapustin, a., Thome, K., & Dutton, E. G. (2011). AERONET-based surface reflectance validation network (ASRVN) data evaluation: Case study for railroad valley calibration site. *Remote Sensing of Environment*, *115*(10), 2710–2717. http://doi.org/10.1016/j.rse.2011.06.011

Wanner, W., Li, X., & Strahler, A. H. (1995). On the derivation of kernel-driven models for kernel-driven models of bidirectional reflectance. *Journal of Geophysical Research: Atmospheres*, *100*(D10), 21077–21089.

Wanner, W., Strahler, A. H., Hu, B., Lewis, P., Li, X., & Barker, C. L. (1997). Global retrieval of bidirectional reflectance and albedo over land from EOS MODIS and MISR data: Theory and algorithm. *Journal of Geophysical Research: Atmospheres*, *102*(D14), 17143–17161.

Wei, J., Van Dommelen, R., Lewis, M. R., McLean, S., & Voss, K. J. (2012). A new instrument for measuring the high dynamic range radiance distribution in near-surface sea water. *Optics Express*, *20*(24), 27024–27038. http://doi.org/10.1029/2011JC007275.19.

Weiss, M., Baret, F., Myneni, R. B., Pragrere, A., & Knyazikhin, Y. (2000). Investigation of a model inversion technique to estimate canopy biophysical variables from spectral and directional reflectance data. *Agronomie*, *20*(2), 3–22.

Woellert, K., Ehrenfreund, P., Ricco, A. J., & Hertzfeld, H. (2011). Cubesats: Cost-effective science and technology platforms for emerging and developing nations. *Advances in Space Research*, *47*(4), 663–684. http://doi.org/10.1016/j.asr.2010.10.009

Wu, J., Wang, D., & Bauer, M. (2005). Image-based atmospheric correction of QuickBird imagery of Minnesota cropland. *Remote Sensing of Environment*, *99*(3), 315–325. http://doi.org/10.1016/j.rse.2005.09.006

Yang, Z., Ruggeri, B., Flikkema, P., & Johnson, D. (2005). WiSARDNet: A system solution for high performance in situ environmental monitoring. *2nd International Workshop on Networked Sensor Systems (INSS 2005)*. Retrieved from http://wisardnet.nau.edu/publications.html

Zhang, H., & Voss, K. J. (2009). Bidirectional reflectance and polarization measurements on packed surfaces of benthic sediments and spherical particles. *Optics Express*, *17*(7), 5217–5231. Retrieved from http://www.ncbi.nlm.nih.gov/pubmed/19333285